

# MARKOV STATE MODEL-BASED OPTIMAL CONTROL FOR COLLOIDAL SELF-ASSEMBLY

A Thesis  
Presented to  
The Academic Faculty

by

Xun Tang

In Partial Fulfillment  
of the Requirements for the Degree  
Doctor of Philosophy in the  
School of Chemical & Biomolecular Engineering

Georgia Institute of Technology  
December 2016

Copyright © 2016 by Xun Tang

# MARKOV STATE MODEL-BASED OPTIMAL CONTROL FOR COLLOIDAL SELF-ASSEMBLY

Approved by:

Professor Martha A. Grover, Advisor  
School of Chemical & Biomolecular  
Engineering  
*Georgia Institute of Technology*

Professor Sven Holger Behrens  
School of Chemical & Biomolecular  
Engineering  
*Georgia Institute of Technology*

Professor Yoshiaki Kawajiri  
School of Chemical & Biomolecular  
Engineering  
*Georgia Institute of Technology*

Professor Matthew J. Realff  
School of Chemical & Biomolecular  
Engineering  
*Georgia Institute of Technology*

Professor Fumin Zhang  
School of Electrical and Computer  
Engineering  
*Georgia Institute of Technology*

Date Approved: September 15, 2016

## ACKNOWLEDGEMENTS

My special thanks goes to Dr. Martha Grover, my Ph.D. advisor, who introduced me this wonderful project and brought me into the world of process control. Without her guidance, mentoring, and expertise, this work would not be finished.

I would like to thank my collaborators Dr. Michael Bevan at Johns Hopkins University, Dr. David Ford at University of Massachusetts at Amherst, and their students who contributed to this project. I would also like to extend my appreciations to my thesis committee members, Dr. Sven Holger Behrens, Dr. Yoshiaki Kawajiri, Dr. Matthew J. Realf, and Dr. Fumin Zhang, for the insightful discussion and valuable comments provided pertaining this work.

I am also grateful to the current and former members in Dr. Grover's research group and all the friends I met at Georgia Tech, for all the help, accompany and happiness they brought to my life.

Last but not least, I would like to express my deepest thanks to my parents, my uncle and his entire family for their unconditional love and support.

# TABLE OF CONTENTS

<b>ACKNOWLEDGEMENTS</b> . . . . .	<b>iii</b>
<b>LIST OF TABLES</b> . . . . .	<b>vii</b>
<b>LIST OF FIGURES</b> . . . . .	<b>viii</b>
<b>SUMMARY</b> . . . . .	<b>xiii</b>
<b>I INTRODUCTION</b> . . . . .	<b>1</b>
<b>II BACKGROUND</b> . . . . .	<b>7</b>
2.1 Simulation of Colloidal Self-Assembly . . . . .	7
2.1.1 Brownian Dynamics Simulation . . . . .	8
2.1.2 Dimensionality Reduction and Order Parameters . . . . .	10
2.1.3 Fokker-Planck and Smoluchowski Equation . . . . .	11
2.2 Control of Colloidal Self-Assembly . . . . .	13
2.2.1 Control by Particle Surface Property Modification . . . . .	14
2.2.2 Control by Global Driving Forces . . . . .	17
2.3 Summary . . . . .	24
<b>III METHODS</b> . . . . .	<b>26</b>
3.1 Colloidal System . . . . .	26
3.2 Brownian Dynamics Simulation . . . . .	29
3.3 Markov State Model . . . . .	31
3.4 Dynamic Programming . . . . .	32
3.4.1 Markov Decision based Optimization Framework . . . . .	32
3.4.2 Algorithms for Dynamic Programming . . . . .	34
<b>IV PROOF-OF-PRINCIPLE</b> . . . . .	<b>36</b>
4.1 Introduction . . . . .	36
4.2 Methods . . . . .	39
4.2.1 Experimental Control . . . . .	39

4.2.2	Markov State Model Construction . . . . .	39
4.3	Stochastic Polycrystal Assembly . . . . .	40
4.4	Results . . . . .	41
4.4.1	Uncontrolled Simulations with Ramp . . . . .	41
4.4.2	Feedback Control Policy . . . . .	43
4.4.3	Controlled versus Uncontrolled Assembly . . . . .	47
4.4.4	Conclusion . . . . .	49
<b>V</b>	<b>EXPANSION OF THE FRAMEWORK . . . . .</b>	<b>50</b>
5.1	Introduction . . . . .	50
5.2	Methods . . . . .	51
5.2.1	Experimental Control . . . . .	51
5.2.2	Markov State Model Construction . . . . .	52
5.3	Order Parameters and Control Policies . . . . .	52
5.4	Results . . . . .	55
5.4.1	Calculation of Control . . . . .	55
5.4.2	Performance in Brownian Dynamic Simulation . . . . .	55
5.4.3	Performance in Experiments . . . . .	58
5.4.4	Discussion and Conclusion . . . . .	62
<b>VI</b>	<b>REVISITING THE MARKOV STATE MODEL . . . . .</b>	<b>67</b>
6.1	Introduction . . . . .	67
6.2	Markov State Model . . . . .	69
6.2.1	Transition Time $\Delta t$ . . . . .	69
6.2.2	Sampling . . . . .	70
6.2.3	State Discretization . . . . .	72
6.3	Results . . . . .	73
6.3.1	Effect of $\Delta t$ . . . . .	73
6.3.2	Effect of Discretization . . . . .	78
6.3.3	Effect of Numbers of States . . . . .	80

6.3.4	Effect of Sample Sources . . . . .	82
6.4	Discussion . . . . .	85
6.5	Conclusion . . . . .	86
<b>VII</b>	<b>CONCLUSION AND OUTLOOK . . . . .</b>	<b>88</b>
7.1	Conclusion . . . . .	88
7.2	Outlook . . . . .	90
7.2.1	Control Input Selection . . . . .	91
7.2.2	System State Measurement and Representation . . . . .	92
7.2.3	Combination with Other Systems . . . . .	93
7.2.4	Optimal Policy Design . . . . .	94
7.2.5	Extension to Continuous Systems . . . . .	95
<b>APPENDIX A</b>	<b>— COLLOIDAL SELF-ASSEMBLY WITH MODEL</b>	
	<b>PREDICTIVE CONTROL . . . . .</b>	<b>97</b>
<b>REFERENCES</b>	<b>. . . . .</b>	<b>111</b>

## LIST OF TABLES

1	Parameters for BD simulations. . . . .	31
2	Parameters for Experiments. . . . .	41
3	BD yield and assembly time of 100 realizations . . . . .	58
4	Experimental yield and assembly time of 40 cycles . . . . .	62
5	BD yield and assembly time of 200 realizations for policies with different $\Delta t$ and different numbers of samples . . . . .	75
6	BD yield and assembly time of 200 realizations for policies computed with gridding-based models using different policy modifications . . . . .	79
7	BD yield of 200 realizations with policies adaptive to different numbers of states . . . . .	81
8	BD yield and assembly time of 200 realizations for policies with samples generated under different input trajectories . . . . .	84

# LIST OF FIGURES

1	Natural colorful materials with periodic constituents elements: (A) 1-D grating in natural flowers; (B) 1-D periodicity in the form of multilayers; (C) some discrete 1-D periodicity in butterflies and iridescent plant leaves; (D) natural surfaces with 2-D gratings used for anti-reflection and self-cleaning;(E) natural 2-D periodicity in the form of cylindrical voids embedded in high-refractive-index solid mediums, such as in the iridescent hairs of Aphrodite; (F) close-packed spheres of solid materials in gem opals and in beetles; (G) inverse opal analogous nanostructures in exotic butterflies, such as the <i>Parides sesostris</i> [124]. Reproduced by permission of The Royal Society of Chemistry. . . . .	2
2	Defects formed in colloidal self-assembly processes: (A) and (B) SiO <sub>2</sub> assembly with polycrystalline and grain boundary formed in an electric field [104]; (C) disalignment and vacancies formed in spin coating assembly [46]; (D) lattice of point defects introduced in a PMMA thin film opal by selectively removing PS spheres [38]. Reprinted image (c) with permission from [46]. Copyright(2010) by the American Physical Society. Image (d) is reprinted with permission from [38]. . . . .	3
3	Proposed framework for optimal control: 1. Reducing system dimensionality with initial sampling; 2. Clustering state space for Markov state model construction; 3. Resampling the original system to cover a common state space under each input levels; 4. Construction Markov state models with collected samples; 5. Calculating the optimal control policy via dynamic programming; 6. Evaluating the policy performance on the original system. . . . .	4
4	(A) XZ cross sectional contour plot of analytic solution for electric field between coplanar thin films electrodes; (B) XZ cross sectional contour plot of ID-IF potential; (C) XY cross sectional contour plot of ID-ID potential [53]. Reprinted from [53], with the permission of AIP Publishing . . . . .	9
5	Colloidal kagome lattice after equilibration. (a) Triblock Janus spheres, hydrophobic on the poles and charged in the middle section, are allowed to sediment in deionized water. Then NaCl is added to screen electrostatic repulsion for short-range hydrophobic attraction. (b) Fluorescence image of a colloidal kagome lattice and its fast Fourier transform image (bottom right). The top panel in (c) shows an enlarged view of the dashed white rectangle in (b). Dotted red lines in c highlight two staggered triangles. The bottom panel in c shows a schematic illustration of particle orientations [25]. Reprinted by permission from Macmillan Publishers Ltd: [Nature] [25], copyright (2011). . . . .	14

6	Schematic of experimental design to show the assembly process under different thermal and structural conditions. (a) The assembly system of DNA-capped nanoparticles, the aggregates show structural changes under various thermal conditions. (b) DNA linkages between nanoparticles with recognition sequences for the A (blue) and B (red) sets of DNA capping. bp stands for base pairs. b stands for bases and s stands for thiol termination of DNA [71]. Reprinted by permission from Macmillan Publishers Ltd: [Nature] [71], copyright (2008). . . .	16
7	The suspension evolution after the pulsed magnetic field is applied as a function of the pulse frequency. Particle-rich regions of the suspension appear dark on the bright background of transmitted light. The field strength is 1500 Am. After 2000 s in the pulsed field all suspensions appear to have reached their terminal or at least slowly evolving state. While suspension condenses into large magnetic domains near 0.66 Hz, high pulse frequencies ( $\geq 5$ Hz) make the suspension remains percolated and the lowest pulse frequency makes the kinetics of depercolation appear to slow significantly [101]. Reproduced from [101] with permission form The Royal Society of Chemistry. . . . .	19
8	Experimental setup and top view of particle configurations under a microscope. System demonstrates opposite free energy landscape under different electric field frequencies, and the order parameter trajectories possess different characteristics under different voltage levels [54]. Reprinted from [54] with permission from John Wiley and Sons. . . .	21
9	Dynamic feedback controlled assembly and disassemble of a colloidal crystal in terms of order parameter $C_6$ . Experimental optical video microscopy images and particle trajectories for the assembly process with values of (A) 2, (B) 3, (C) 4, (D) 5, and (E) 6. The top image pane shows individual particle $C_6$ with color scaling white for $C_6 = 1$ and blue for $C_6 = 6$ . Particle trajectories by linear spectrum scaled with red for $t = 0$ and violet for $t = 40$ s. Dynamic assembly and disassembly trajectories showing (top) $C_{6SP}$ in solid blue line, $C_{6PV}$ in shaded blue points vs. time and (bottom) electric field voltage, V, (green) and frequency, $\omega$ (orange) vs. time [54]. Reprinted from [54] with permission from John Wiley and Sons. . . . .	23
10	Experimental setup at JHU. (a) batch container with four electrodes attached to generate the electric field; (b) top view of 300 SiO <sub>2</sub> colloidal particles suspended in 1.0 mM NaOH solution under a microscope; (c) Single particle-field potential (blue-red scale: 0-100 kT [104]. Reprinted with permission from [104]. Copyright (2016) American Chemical Society. . . . .	27
11	A backwards conduction algorithm in dynamic programming for finite-horizon Markov decision process based optimization. . . . .	34

12	Quasi-2D colloidal crystal assembly in electric fields. (a) Microfabricated quadrupole electrode. (b) Optical microscopy image of particles within quadrupole. (c) Single particle-field potential (blue-red scale: 0-100 kT). Images of 300 particles with centers colored to visualize reaction coordinates for local hexagonal order, $C_6$ in blue, and global hexagonal order, $\psi_6$ in red, at electric field amplitudes of $\lambda =$ (d) 0.2, (e) 0.9, (f) 2.0, and (g, h, i) 19.7. Representative micro-structures include bicrystals with, (g) large grain boundary (similar sized domains near max misorientation angle), (h) small grain boundary (dissimilar sized domains with smaller misorientation angle), (i) no grain boundary i.e., perfect crystal [104]. Reprinted with permission from [104]. Copyright (2016) American Chemical Society. . . . .	38
13	Ramping electric field at different rates without feedback control. Electric field amplitude, $\lambda$ (long-dash gray), ramped from 0.2 to 19.7 over (a) 0 s (blue), (b) 1000 s (cyan), (c) 2000 s (red), (d) 5000 s (green), and (e) 10000 s (black). Local order, $C_6$ (dotted lines), emerges before global order, $\psi_6$ (solid lines). Equilibrium $\psi_6$ values (open circles) vs. $\lambda$ approach $\psi_6$ ramp trajectories only for the 10000 s ramp case. Reprinted with permission from [104]. Copyright (2016) American Chemical Society. . . . .	42
14	Assembly trajectory on energy landscapes under control. (a) Free energy landscapes of 300 particles at the four $\lambda$ s in policy. Example trajectory (black) with coordinates on policy (b) and corresponding images (c-h). (b) Optimal policy calculated using Markov decision process. Images showing representative configurations with the same coloring scheme as in Figure 12(d)-(i) at: (c) $\lambda = 0.2$ before compression, (d) first compression to $\lambda = 19.7$ with grain boundary, (e) relaxation at $\lambda = 0.9$ , (f) re-compression at $\lambda = 19.7$ with new grain boundary, (g) relaxation at $\lambda = 2.0$ , (h) perfect crystal at $\lambda = 19.7$ [104]. Reprinted with permission from [104]. Copyright (2016) American Chemical Society. . . . .	46
15	Controlled vs. uncontrolled crystal assembly processes. 100 uncontrolled and 100 controlled trajectories shown as: (a) first 10 cycles with $C_6$ (blue), $\psi_6$ (red), $\lambda$ (black) vs. time, (b) $\psi_6$ vs. time for 1000 s for all experiments colored to indicate ensemble average (bold red), no grain boundary (red: $\psi_6 > 0.7$ , $C_6 > 0.95$ ), small grain boundary (orange: $0.7 > \psi_6 > 0.4$ , $C_6 > 0.95$ ), large grain boundary (peach: $0.4 > \psi_6$ , $C_6 > 0.95$ ), (c) perfect crystals vs. time as cumulative number (dark red) and instantaneous number (bars) with same color scheme as (b) [104]. Reprinted with permission from [104]. Copyright (2016) American Chemical Society. . . . .	48

16	Typical assembly configurations with order parameter values from simulation under different input levels: (a) fluid-like state, which only exists under low input $\lambda = 0.2$ ; (b) and (c) polycrystalline and grain boundary states, formed under high input $\lambda = 19.7$ ; (d) the desired defect-free structure only achievable under high input $\lambda = 19.7$ . . . .	54
17	(a) infinite horizon control policy shown as a lookup table in order parameter space; (b) three open loop schemes with optimal open-loop control policy developed from MSM colored in blue, Periodic strategy in red, and Constant in green. . . . .	56
18	900 s finite horizon optimal control policy. Each lookup table presents the control policy for its corresponding 100 s interval, with the last (9th) 100 s interval using $\lambda = 19.7$ to maintain the crystal structure. .	57
19	100 realization averaged BD simulations with results from open-loop strategies plotted in the insect figures. (a) $\psi_6$ evolution over time; (b) $C_6$ evolution over time; (c) cumulative yield of grain boundary free structures over time; (d) averaged input profiles from closed-loop control strategies. . . . .	59
20	Individual BD simulation runs from Periodic, Optimal OL, and InfCL control strategies, showing the corresponding control mechanism. (a) $\psi_6$ trajectories over time; (b) control input profiles. All three simulations were initiated in the same configuration and were simulated with the same seed. . . . .	60
21	10 cycles averaged experimental results of the five strategies, with closed-loop controlled results plotted in the main figure and the open-loop controlled results in the insect figures. (a) $\psi_6$ evolution over time; (b) $C_6$ evolution over time; (c) cumulative yield of grain boundary free structures over time; (d) averaged input profiles used in the experiments.	63
22	Individual experimental runs from Periodic, Optimal OL, and InfCL strategies showing the corresponding control mechanism. (a) $\psi_6$ trajectory over time; (b) control input profile. . . . .	64
23	Control policies and controlled results with different transition times using 10000 samples. Control policy with (a) $\Delta t = 10$ s; (b) $\Delta t = 50$ s; (c) $\Delta t = 100$ s. (d) Yield and averaged input trajectories of 200 BD realizations. . . . .	73
24	Averaged order parameter relaxation trajectories under $\lambda = 0.2$ , starting from assembled states in BD simulation (black), Markov chain Monte Carlo simulation with model built with $\Delta t = 10$ s (red), $\Delta t = 50$ s (blue), and $\Delta t = 100$ s (magenta). . . . .	75

25	100-state clustering-based control policies with different transition time and different number of samples. Policy for (a) $\Delta t = 50$ s with 100 samples; (b) $\Delta t = 100$ s with 100 samples; (c) $\Delta t = 50$ s with 1000 samples; (d) $\Delta t = 100$ s with 1000 samples. . . . .	76
26	Control policies computed with gridding-based Markov state models, with policy modified to have: (a) default action as $\lambda = 0.2$ , i.e. GL; (b) default action as $\lambda = 19.7$ , i.e. GH;(c) modified with extrapolation and interpolation, i.e. GE. (d) Averaged yield of 200 controlled BD simulations, using control policies in Figure 4(d) and the three gridding-based policies. . . . .	80
27	Control policies for 100-state models with 1000 samples from BD simulations under (a) constant input; (b) toggling input; (c) optimal control policy; (d) randomly switched input. . . . .	83
28	Continuous flow system for colloidal self-assembly in the format of a plug flow reactor. $V$ is the velocity with unit <i>length/time</i> and $\Delta t$ is the time needed for state measurement and control action calculation. . . . .	96
29	(a) FELs calculated via BI method based on BD simulation, (b) DLs calculated via BI method based on BD simulation, (c) FELs from simplified analytical model, (d) DLs from simplified analytical model. . . . .	100
30	Averaged $C_6$ trajectories over 100 realizations for different constant input $u$ from system without a feedback control policy. . . . .	104
31	Comparison of best controlled $C_6$ trajectories for each number of control interval $s$ versus uncontrolled $C_6$ trajectory with input $u = 4$ . . . . .	106
32	Average cost $J(x, u)$ over 100 realizations for different combination of $s - h$ . . . . .	107
33	Controlled input $u$ trajectories for combinations of $s3-h4, s5-h5, s8-h2$ over 100 realizations. . . . .	108
34	Computational time for controlled system with control steps of $s = 2, s = 3, s = 5$ and 10 realizations. . . . .	109

## SUMMARY

Colloidal self-assembly is widely studied as a promising route to manufacture highly ordered structures for applications as metamaterials. While near-equilibrium self-assembly could produce defect-free crystal, the time required is usually unmanageable in practical applications. On the contrary, rapid assembly via out-of-equilibrium approaches could reduce the amount of process time, but the assembled structure is usually terminated in defective states. Therefore, a gap exists between the speed and the quality of the structure in a colloidal self-assembly system. To overcome this challenge, this thesis proposes a model-based optimization framework for optimal feedback control over a colloidal self-assembly process for rapid assembly of defect-free two-dimensional crystals.

The proposed framework features: first, the use of an externally applied electric field as a global actuator to influence the particle movement; second, the use of two order parameters to represent the high-dimensional system in a reduced dimension state space; third, the use of the Markov state model to capture the stochasticity in the system; fourth, the use of dynamic programming to design the optimal control policy; and fifth, the use of an optical microscope for *in situ* measurements as feedback.

The feasibility of the framework is first demonstrated with a static optimal control policy, and its performance is evaluated against fast quench and near-equilibrium approaches. The framework is then expanded to construct a time-dependent optimal control policy, and the performance is compared with widely used time-varying control strategies in both simulation and experiments. The refinement of the framework, more specifically, the construction of the Markov state model is also revisited for better efficiency.

The major contributions of this thesis include: (1) it proposes a novel approach to rapidly control colloidal self-assembly processes for perfect crystal with optimal control theories; (2) it demonstrates for the first time in lab, the realization of optimal feedback control of a colloidal self-assembly process; (3) it reveals the benefits of feedback in a stochastic process control, not only to compensate for model inaccuracy, but also to shorten the process time; (4) it also investigates the Markov state model accuracy and provides a more efficient construction of accurate Markov state models.

The framework in this study is built on first-principle concepts, and it can be generalized to any molecular, nano-, or micro-scale assembly process where there exists a global actuator to affect the dynamics, a model to represent the relation between the actuator and the system, and a measurement of system state for feedback. Since micron-sized colloidal particles also serve as model systems to study the phase transition behavior and crystallization kinetics for atomic and molecular crystals, the framework can also be extended to these systems for optimal control.

# CHAPTER I

## INTRODUCTION

Natural colorful materials, from flowers to butterfly wings to beetle and gem opals (Figure 1), demonstrate their iridescent color not by absorption or pigmentation alone, but via interactions with light due to the periodic design of their constituent elements [124]. The ability to manipulate and control the interactions of materials with photons, via material design, could potentially open doors for new materials with novel properties. Therefore manufacturing materials with highly ordered structures has received intensive research interest.

Metamaterials are artificial electromagnetic materials with sub-wavelength structures that can be designed to exhibit strong coupling with the magnetic and/or electric component of an incident electromagnetic wave [112]. With a negative refractive index, metamaterials allow us to surmount obstacles of nature to present new materials with novel properties for applications in photonics, biomaterials, energy harvesting, and communications [14, 21, 22, 30, 67].

Contrary to materials whose physical properties depend on the intrinsic properties of the elemental constituents, the properties of metamaterials depend on their internal, specific structures instead, or in addition. However, control of the structure is challenging. Currently available manufacturing methods can generally be defined into two categories: *top-down* and *bottom-up* approaches [15]. Top-down fabrication such as lithography, is achieved largely by patterning features. It starts from larger dimensions and reduces to the required structures [39]. The top-down approach has shown success as reported in [15] and its references, and is the basis for microelectronics manufacturing. However, it is usually costly to use top-down approaches for

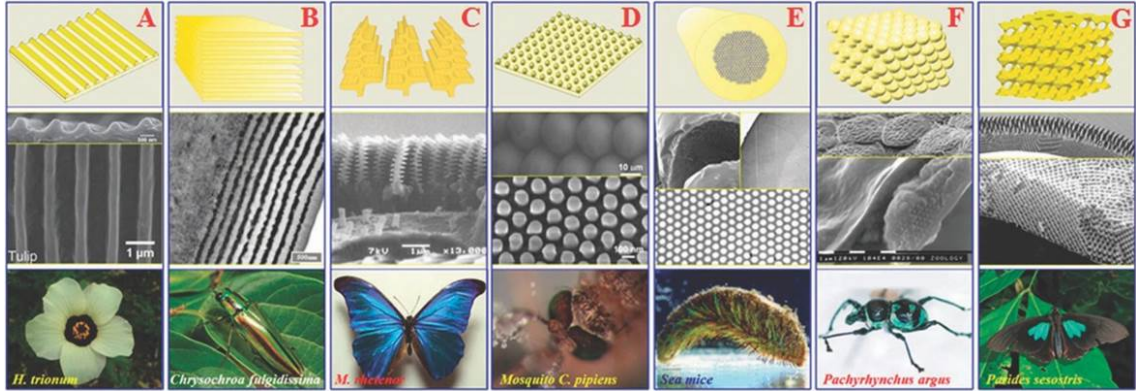


**Figure 1:** Natural colorful materials with periodic constituents elements: (A) 1-D grating in natural flowers; (B) 1-D periodicity in the form of multilayers; (C) some discrete 1-D periodicity in butterflies and iridescent plant leaves; (D) natural surfaces with 2-D gratings used for anti-reflection and self-cleaning; (E) natural 2-D periodicity in the form of cylindrical voids embedded in high-refractive-index solid mediums, such as in the iridescent hairs of Aphrodite; (F) close-packed spheres of solid materials in gem opals and in beetles; (G) inverse opal analogous nanostructures in exotic butterflies, such as the *Parides sesostris* [124]. Reproduced by permission of The Royal Society of Chemistry.

mass production, and it usually has no control of the defects formed along the process. On the other hand, bottom-up fabrication builds up assemblies from smaller components. This could potentially provide a more promising fabrication method for large quantities with less waste and better quality control [7, 15]. One example is the colloidal self-assembly.

Colloidal particles are microscopic solid particles suspended in a fluid [64]. Self-assembly refers to the formation of organized structures from many discrete components due to direct or indirect interactions with each other and their environment [44, 45]. Self-assembly of nano-meter and/or micro-meter objects, including particles, colloids, and folded proteins, into ordered structures could enable metamaterials with exotic properties that are otherwise unattainable. Thus, self-assembly has been deemed as the most practical strategy for making regular periodic crystals at nano- and micro-scales. In particular, colloidal self-assembly has received tremendous attention since colloidal nano- and micro-spheres are in the length scale from several

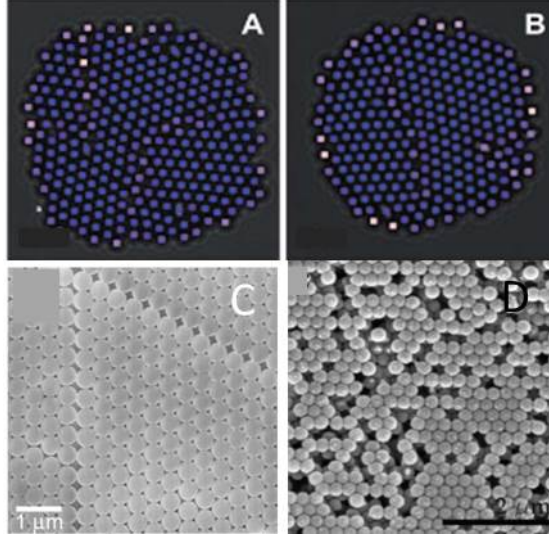


**Figure 2:** Defects formed in colloidal self-assembly processes: (A) and (B) SiO<sub>2</sub> assembly with polycrystalline and grain boundary formed in an electric field [104]; (C) disalignment and vacancies formed in spin coating assembly [46]; (D) lattice of point defects introduced in a PMMA thin film opal by selectively removing PS spheres [38]. Reprinted image (c) with permission from [46]. Copyright(2010) by the American Physical Society. Image (d) is reprinted with permission from [38].

micrometers to tens of nanometers, which is close to the resolution limit of conventional patterning techniques [123].

Colloidal particles at the micron scale, by virtue of their size, can be monitored in real time and real space without requiring advanced measuring techniques as in atomic systems. The fundamental dynamics of colloidal particles at a wide range of length scales does not differ dramatically, such that knowledge on one system could potentially be applied to other length scale systems. Additionally, understanding the behavior and the control of micro-sized colloidal self-assembly processes could also shed light on systems with molecular and nano-scaled components, since micro-sized colloidal particles also serve as model systems to study the phase transition behavior and crystallization kinetics for atomic and molecular crystals [5, 90].

One long standing problem associated with colloidal self-assembly process is the

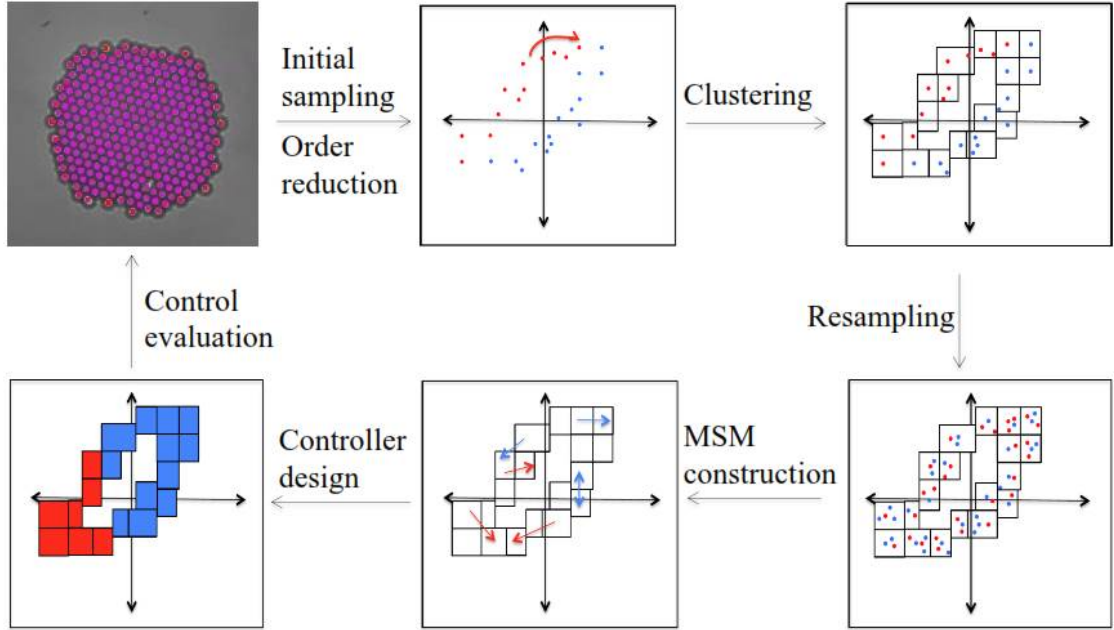


**Figure 3:** Proposed framework for optimal control: 1. Reducing system dimensionality with initial sampling; 2. Clustering state space for Markov state model construction; 3. Resampling the original system to cover a common state space under each input levels; 4. Construction Markov state models with collected samples; 5. Calculating the optimal control policy via dynamic programming; 6. Evaluating the policy performance on the original system.

difficulty in rapid production of perfect crystals. A perfect colloidal crystal is the thermodynamic ground state, which theoretically can be reached after an infinitely long process without external inference. Assembly in finite time accelerates the process. Operation in an out-of-equilibrium mode leads to meta-stable defective structures, which have higher energy but may be persistent (Figure 2). In rapid colloidal self-assembly process, defect formation and migration are stochastic, thus making it hard to predict and control the structure of assemblies. Therefore to bridge the gap between rapid production and low defect density, a robust control over the formation of defects is desired.

This thesis focuses on a micron-sized colloidal self-assembly process in an externally applied electric field to understand and control the defects for rapid production

of perfect two-dimensional crystals. Specifically, an optimization framework is proposed with a reduced-order Markov decision process, to design an optimal feedback control policy to eliminate the grain boundary formed along the assembly process.

The key steps of the proposed framework are presented in Figure 3, and are summarized as follows:

1. Conducting dimensionality reduction analysis to identify lower system dimensions (e.g. with order parameters) with initial sampling from the original high dimensional system;
2. Clustering the continuous lower dimensional state space into discrete states for the construction of Markov state models;
3. Generating additional samples from the original high dimensional system to cover a common state space under each of the control input levels;
4. Building Markov state models with the collected samples to approximate the transition probabilities between different discrete states;
5. Solving for the optimal control policy in the format of lookup tables based on the Markov state models, via dynamic programming;
6. Evaluating the performance of the control policy on the original system.

The whole process or part of the procedure could be repeated until satisfying results are achieved.

This thesis is organized as follows: Chapter 2 provides the background of current advances and progress in modeling and controlling colloidal self-assembly processes; Chapter 3 summarizes the experimental setup and preparation, the basics of dynamic programming, and the fundamentals of Markov state models; Chapter 4 provides the proof-of-principle for the proposed framework on a colloidal self-assembly process

with a time-invariant optimal control policy; Chapter 5 extends the study for a more comprehensive comparison with both open-loop and closed-loop control strategies; Chapter 6 investigates the improvement of the framework for more efficient construction of the MSMs; Chapter 7 concludes the findings and provides an outlook on the topic of colloidal self-assembly.

## CHAPTER II

### BACKGROUND

Colloidal self-assembly of nano- and micro-meter particles is a stochastic process, in which particle movements, defect formation and migration are random. A solid understanding of the system dynamics is required to design experiments to control and eliminate the defects, in order to achieve highly ordered structures. Studying system dynamics directly from experiments can provide the most accurate information, but is usually costly and challenging to generate a sufficient amount of samples to account for statistical effects in a stochastic process. In particular, if meta-stable states exist, the time required to observe meaningful dynamics can be beyond an experimentally achievable timescale. Alternatively, computer simulations provide a more efficient approach to understand the underlying dynamics of colloidal self-assembly processes. This chapter summarizes the most widely used simulation techniques for colloidal self-assembly processes, and provides a background on the current studies on control.

#### *2.1 Simulation of Colloidal Self-Assembly*

The development of mathematical models to simulate colloidal self-assembly systems is a subject of intense interest and research. Understanding the equilibrium and steady-state structures is important. However, meta-stable states and kinetics bottlenecks could prevent the system from reaching equilibrium states within accessible time scales. In this chapter, the two main approaches used to simulate the dynamic behaviors are presented. Specifically, the simulation based on detailed force balance analysis, and the simulation with reduced-order models using order parameters are studied.

### 2.1.1 Brownian Dynamics Simulation

Micron-sized colloidal particles are subjected to Brownian motion. The random movement of each particle is the result of the collision between the particles and the surrounding molecules. In other words, the motion of the particle is subjected to stochastic forces on the system. Therefore, using Newton's second law to analyze the forces each particle experiences in the system enables the simulation of particle movements. One such an example is the Brownian dynamics simulation.

The Brownian dynamics simulation framework is usually built on a differential equation, such as the Langevin equation, which is integrated forward in time to describe the motion of the Brownian particles.

The general form of a Langevin equation to describe a particle with mass  $M$  that undergoes stochastic forces is given as [31]:

$$M\ddot{\mathbf{r}} = -(\mathbf{r}) - \zeta M\dot{\mathbf{r}} + \zeta M\kappa(\mathbf{r}) + \mathbf{F}^{(b)} \quad (1)$$

where  $\mathbf{r}$  is the particle position, e.g. Cartesian coordinates,  $\zeta$  is the specific friction coefficient,  $U$  is the net particle interaction potential,  $\kappa$  is the homogeneous velocity gradient, and  $\mathbf{F}^{(b)}$  is the Brownian force experienced by the particle. Assuming a Gaussian process behavior,  $\mathbf{F}^{(b)}$  can be further defined as:

$$\mathbf{F}_t^{(b)} = \sqrt{2k_B T \zeta M} \frac{d(\mathbf{W})_t}{dt} \quad (2)$$

with  $k_B$  being the Boltzmann's constant,  $T$  being the absolute temperature, and  $(\mathbf{W})_t$  a Wiener process at time instant  $t$ .

Neglecting the inertia effects on the particle, the Brownian dynamics equation of a Brownian particle is then described as:

$$0 = -(\mathbf{r}) - \zeta M\dot{\mathbf{r}} + \zeta M\kappa(\mathbf{r}) + \sqrt{2k_B T \zeta M} \frac{d(\mathbf{W})_t}{dt} \quad (3)$$

Further introducing the definition of friction coefficient  $\varsigma = M\zeta$  and the diffusion coefficient of the particle  $D = k_B T / \zeta$ , the Brownian dynamics simulation equation

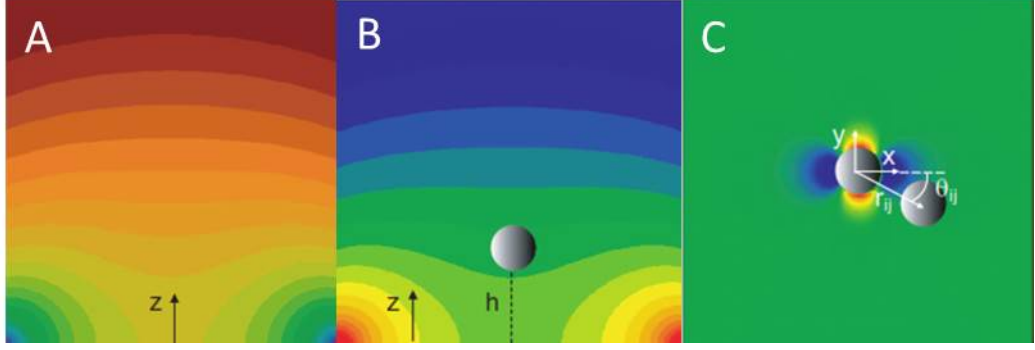


**Figure 4:** (A) XZ cross sectional contour plot of analytic solution for electric field between coplanar thin films electrodes; (B) XZ cross sectional contour plot of ID-IF potential; (C) XY cross sectional contour plot of ID-ID potential [53]. Reprinted from [53], with the permission of AIP Publishing

for the instantaneous particle velocity can then be presented as:

$$\dot{\mathbf{r}} = \frac{-\langle \mathbf{r} \rangle}{\zeta} + \kappa(\mathbf{r}) + \sqrt{2D} \frac{d(\mathbf{W})_t}{dt} \quad (4)$$

With specified potential  $U(\mathbf{r})$ , friction coefficient  $\zeta$ , and diffusion coefficient  $D$  for a particular system, the Brownian dynamic simulation can be tailored to simulate specific colloidal self-assembly systems.

For example, in Ref. [53], the authors reported the use of a Brownian dynamics simulation to study the quasi-two-dimensional configuration of micron-sized silica colloids in an externally applied electric field between coplanar thin films electrodes. Figure 4 shows the simulated forces in Brownian dynamics [53].

When the electric field is applied, colloidal particles become induced dipoles, which can interact with each other and the field to generate movement. The net interaction potential that drives the assembly of the system in the electric field is presented as the sum of particle-particle, particle-wall, and particle-field interactions. Mathematically, it is given as  $u^{(net)} = u^{(pp)} + u^{(pw)} + u^{(pf)}$ , where  $u^{(pp)}$  is the particle-particle potential which includes an electrostatic interaction and a dipole-dipole interaction,  $u^{(pw)}$  is the particle-wall potential which only includes the electrostatic interactions, and  $u^{(pf)}$  is the particle-field potential which includes the gravitational potential energy and the

interaction of the induced dipole with the induced field [53].

Using inverse statistical mechanical analyses to calculate these interaction potentials, Juárez *et al.* demonstrated the ability of the Brownian dynamics simulation to quantify interactions in the electric field and describe the dynamics of the silica colloidal self-assembly process [53].

Tracking particle coordinates to define the system state as in Ref. [53] is usually computationally demanding. In addition, for systems where overall system level properties, such as ordering, are of more interest than individual particle locations, a set of aggregate variables, i.e. order parameters, is often used to characterize the assembly. Sometimes they are also used to model the dynamics.

### 2.1.2 Dimensionality Reduction and Order Parameters

Dimensionality reduction can be implemented with either numerical methods or physical interpretations, or a combination of both. Numerical approaches include both linear techniques like Principal Component Analysis and its extensions [84, 119], factor analysis [109]; and nonlinear techniques like diffusion maps [28, 29] and other manifold dimensionality reduction methods [37, 109]. Numerical algorithms are generally straightforward to implement using widely distributed software. However, the resulting variables from numerical dimensionality reduction usually bear no physical meaning, and this makes it challenging to uncover a physical phenomenon.

Alternatively, constructing aggregate variables with domain knowledge can potentially provide physically meaningful parameters to better illustrate the complex system dynamics. Taking the colloidal system as an example, if the feature of interest is the compactness of the particles, then radius of gyration,  $R_g$ , which quantifies the root-mean square distance between particles within an ensemble, can be used; if the local order of a structure is of interest, then the averaged number of nearest neighbors can be used, such as  $C_6$  for a 2-D hexagonal structure; if the global order is needed,

then global orientation parameters which describe the particle-particle bond orientation, like  $\psi_6$ , can be used. Other examples include pair-correlation or distribution functions [89], volume fraction [92], and dihedral angles [86].

The use of physically meaningful parameters tremendously mitigates the difficulty of relating the numerical values to a physical phenomenon, however this approach not only requires domain knowledge, it also requires extensive validation. Sometimes, a combination of the numerical approach and physical interpretation could be used. For example, in Ref. [13], diffusion map is used to verify the use of  $R_g$  and  $C_6$  to quantify defect formation in a depletion force mediated colloidal self-assembly process. A combination of physical interpretation and numerical techniques could not only provide physically meaningful order parameters, it could also provide mathematical justification to the selection.

### 2.1.3 Fokker-Planck and Smoluchowski Equation

Instead of tracking particle locations, if a stochastic process can be characterized with order parameters, then simulation can be achieved by modeling the evolution of the probability density  $P(x, t)$  of the order parameters, where  $x$  is the order parameter(s), and  $t$  is the time instant. Further if the system dynamics can be classified into fast and slow modes [61], and can be approximated as a Markovian process, the probability density can then be described by low-dimensional stochastic differential equations like the Fokker-Planck and the Smoluchowski equation [61, 82].

Derived from the Kramers-Moyal expansion for the density distribution function  $P(x, t)$ , the Fokker-Planck equation is one of the most widely used mathematical frameworks for stochastic dynamical self-assembly systems. For example, in Ref. [61], the authors presented the derivation of the general Fokker-Planck equation for a one-dimensional stochastic process, and its application on the study of micelle

formation

$$\frac{\partial P(x, t)}{\partial t} = \left[ -\frac{\partial}{\partial x} v(x) + \frac{\partial^2}{\partial x^2} D(x) \right] P(x, t) \quad (5)$$

where  $v(x)$  is the drift coefficient,  $D(x)$  is the diffusion coefficient, and  $x$  is the micelle size for this particular application. The coefficients were reconstructed from short-time kinetic Monte Carlo simulations, and were calculated with linear fitting techniques. The authors concluded that the use of Fokker-Planck equation can successfully represent the Monte Carlo dynamics of micelle formation for a Larson model [61].

As a special form of the Fokker-Planck equation, the Smoluchowski equation is another popularly used description of a stochastic process [61, 82]. The Smoluchowski equation in terms of order parameter  $x$  is [82],

$$\frac{\partial P(x, t)}{\partial t} = \frac{\partial}{\partial x} \left\{ D(x) e^{-W(x)/kT} \frac{\partial}{\partial x} [e^{W(x)/kT} p(x, t)] \right\} \quad (6)$$

where  $P(x, t)$  is the probability,  $D(x)$  is the diffusivity landscape which captures the mobility of trajectories in terms of order parameter  $x$ , same as in Eqn. 5, and  $W(x)$  is the free energy landscape which describes the free energy difference between different states defined by  $x$ . Similar to the Fokker-Planck equation, the coefficients in the Smoluchowski equations can also be estimated with short-scale trajectories instead of long-scale dynamics. This is favorable in systems where meta-stable states exist and it is challenging to obtain long-scale dynamics.

One application of the Smoluchowski equation in the study of colloidal self-assembly can be found in Ref. [118], where Yang and co-authors reported the construction of a low-dimensional Smoluchowski equation and the simulation of an electric field mediated colloidal self-assembly process. With order parameters  $R_g$  and  $C_6$  to quantify the global system condensation and the local ordering of the particles, they demonstrated in simulation that with such a reduced-order Smoluchowski equation, the formation and migration of the grain boundary formed in the assembly

process can be accurately captured. Other applications of the Smoluchowski equation in colloidal self-assembly systems include Refs. [10, 35].

## ***2.2 Control of Colloidal Self-Assembly***

A highly regular arrangement of colloidal particles is needed to realize many novel properties of metamaterials. However, manufacturing highly periodic colloidal crystals is challenging due to the existence of kinetic bottlenecks and meta-stable states. Colloidal self-assembly systems trapped in meta-stable states, i.e. defective states, could take a practically inaccessible amount of time before evolving into a fully ordered structure, assuming no human interference. Therefore, one control objective is to avoid or reduce the amount of time spent in these defective states.

One approach to defect mitigation is called template-assisted self-assembly, where physical templates are introduced to design the positions that particles can occupy, therefore guiding the assembly to a specific structure. Template-assisted assembly relies on the physical constraint on particle location to exclude irregular arrangement, with reported success [51, 88, 114]. However, assembly with templates often lacks the capability of eliminating defects formed along the process.

On the other hand, template-free assembly via particle-particle and particle-environment interaction manipulation can potentially provide control over the defect formation. Without the use of a physical template, assembly can be enabled with attractive interactions between each particle. For systems with repulsive particle-particle interactions, self-assembly can be achieved with a global driving force, created with externally applied fields, to drive particles together. Template-free assembly holds promise for scale-up, the manipulation of particle-particle and particle-field interactions also provides the opportunity for a reversible assembly process.

The following sections discuss in general, the type of control that manipulates these particle-particle and particle-field interactions by either modifying the intrinsic

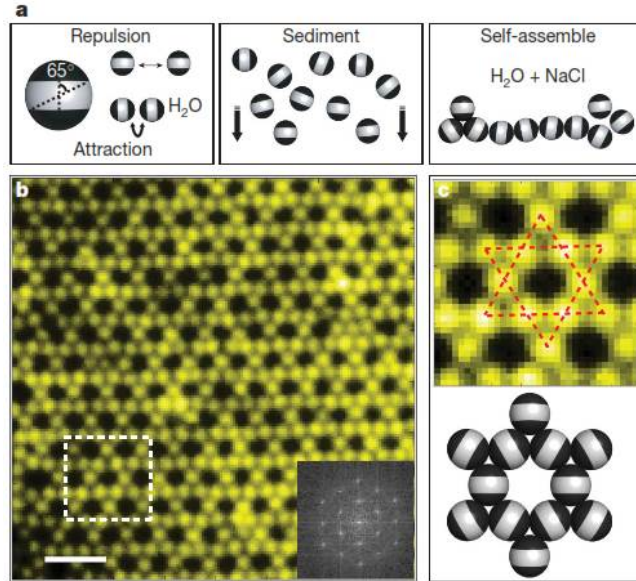


**Figure 5:** Colloidal kagome lattice after equilibration. (a) Triblock Janus spheres, hydrophobic on the poles and charged in the middle section, are allowed to sediment in deionized water. Then NaCl is added to screen electrostatic repulsion for short-range hydrophobic attraction. (b) Fluorescence image of a colloidal kagome lattice and its fast Fourier transform image (bottom right). The top panel in (c) shows an enlarged view of the dashed white rectangle in (b). Dotted red lines in c highlight two staggered triangles. The bottom panel in c shows a schematic illustration of particle orientations [25]. Reprinted by permission from Macmillan Publishers Ltd: [Nature] [25], copyright (2011).

properties of each particle, or using external fields for global driving forces. Review articles on colloidal self-assembly approaches include Refs. [44, 57, 59, 75].

### 2.2.1 Control by Particle Surface Property Modification

Colloidal particle surface properties significantly affect the inter-particle, and particle-field interactions, thereby the structure of the assembly. Thus, one control strategy is to modify the particle surface with engineered properties for specific interactions and configuration. Coined by Casagrande in 1988, Janus particles are particles whose surfaces have two or more distinct physical properties [47]. Research over the past few decades has demonstrated the potential of manufacturing high quality crystals

with Janus particles. In Ref. [47], Hong *et al.* reported the use of amphiphilic colloidal spheres, whose two hemispheres are hydrophobic and charged respectively, to form wormlike strings in both simulation and experiments. The interaction potential between particles switches from the extreme of attraction when the hydrophobic sides face one another to an extreme of repulsion when the charged sides face one another, and exhibits intermediate properties depending on the angle between particle orientation. The range of the angle between particles becomes greater with an increasing slat concentration. The authors demonstrated that, with increased salt concentration to reduce the electrostatic screening length, they were able to observe compact clusters and to produce ordered worm-like objects. They further concluded the clustering is a free energy minimization process and indicated that, potential extensions could be achieved with more complicated design of the sphere’s surface chemistry [47].

In another example [25], Chen *et al.* reported the feasibility of directing “triblock Janus” particles into a colloidal kagome lattice. Different from Ref. [47], “Triblock Janus” latex particles were fabricated through a sequential deposition of titanium and gold to have two hydrophobic poles and a middle electrically charged band. Such a surface decoration enables neighboring particles to attract each other at their hydrophobic poles while avoiding contacts between the charged middle bands. When salt is added in the deionized water to screen electrostatic repulsion, ordering of the assembly is then achieved due to the attractions between particle hydrophobic poles. Using fluorescence imaging, the authors illustrated a two-step assembly mechanism where, particles first cluster with their neighbors into kinetically favored triangles, strings or a combined structure; and then coordinate with additional particles on a slower timescale to rearrange into better ordered structures (Figure 5). Other applications of Janus particles in self-assembly can be found in a recent review paper [33].

Precise design of the coating area on a Janus particle is critical to achieving a

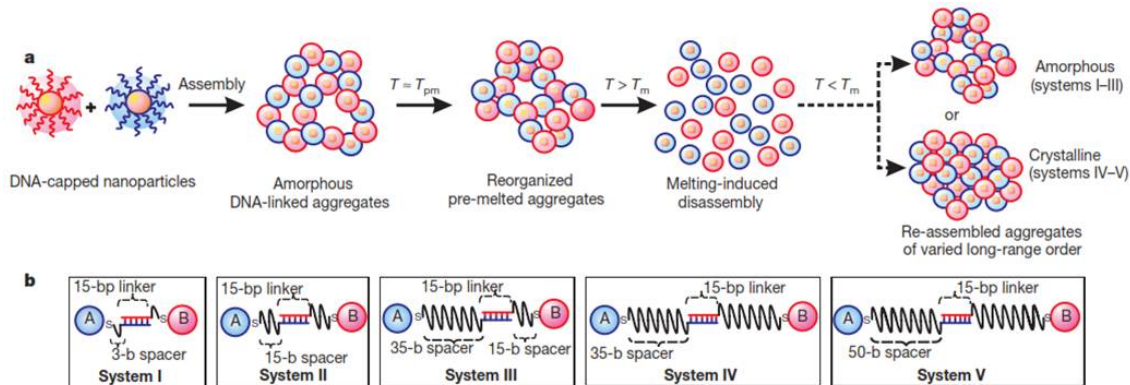


**Figure 6:** Schematic of experimental design to show the assembly process under different thermal and structural conditions. (a) The assembly system of DNA-capped nanoparticles, the aggregates show structural changes under various thermal conditions. (b) DNA linkages between nanoparticles with recognition sequences for the A (blue) and B (red) sets of DNA capping. bp stands for base pairs. b stands for bases and s stands for thiol termination of DNA [71]. Reprinted by permission from Macmillan Publishers Ltd: [Nature] [71], copyright (2008).

specific structure. Assembly in Janus particle systems is always enabled by slowing increasing salt concentration to screen electrostatic repulsion, and this makes the process generally irreversible.

On the other hand, DNA strands disassemble when heated up, and assemble specifically via Watson-Crick base pairing information. The structure of assembly and particle interactions are subjected to the length and the specific sequence of the DNA strand. Therefore modifying particles with DNA could introduce both flexibility and reversibility in self-assembly for ordered structures.

In Ref. [71], Nykypanchuk *et al.* demonstrated the formation of three-dimensional crystalline assemblies of DNA modified gold nanoparticles. The authors reported that heating up the system to its melting temperature reduces the DNA interaction, therefore providing the opportunity for particle rearrangement into the equilibrium structure; while cooling down the system enhances the DNA interactions to enable particle assembly. The study indicates that with a simple heating-cooling cycle, a reversible formation of nanoparticle crystals is observed. The results in Ref. [71]

indicate that the structure of the assembly can be manipulated via the length of the DNA sequence, since a longer DNA sequence allows larger local rearrangements in the structure with a lower energy penalty for the deformation of DNA [71].

DNA coated particles interact with each other due more to the complementary DNA base pair sequence than the particle material or shape. Varying the combinations of the base pair and the lengths of the DNA sequence on the particle surface makes it seem possible to produce limitless colloidal structures [113]. Given these advantages, programming DNA-guided self-assembly has been extensively studied for ordered structures. Refs. [85, 106] provide excellent review summaries of recent development and progress on this topic.

### **2.2.2 Control by Global Driving Forces**

Instead of manipulating particle interactions via modifying intrinsic particle properties, self-assembly process can also be controlled with global driving forces created by external fields including magnetic and electric fields.

In an external field mediated self-assembly system, assembly dynamics is primarily influenced by particle-field interactions which can be adjusted by changing the system settings, i.e. global actuator(s). Self-assembly systems possess different free energy properties corresponding to different morphology, under different global actuator settings. The idea of changing global actuator is to create an out-of-equilibrium approach that breaks kinetically trapped structures for rapid assembly of perfect crystals. Based on system dynamics under different settings, controlling self-assembly is equivalent to designing the global actuator(s) trajectory (i.e. control input profile) to avoid kinetic bottlenecks and meta-stable states. Such control strategies can be obtained from either heuristic experience, or model-based simulations as open-loop or closed-loop control policies.

### *2.2.2.1 Open-loop control*

Open-loop control policies are recipes designed beforehand, and the control action is updated according to the process time, independent of system state. The design of open-loop control policies usually does not require complicated calculations, and can be achieved with experimental observations or model-based simulations.

One such open-loop control policy is to control the self-assembly of nano-scaled superparamagnetic particles, in a magnetic field in Ref. [101], developed heuristically. When the magnetic field is turned on, particles interact with the field to first form chains parallel to the magnetic field lines and then start aggregating laterally. In a constant magnetic field, the lateral aggregation arrests the particle motion and forms defective structure that could not evolve into ordered state, due to the strong attractive force between the particles. In contrast, when the field is turned off, the attractive force is suppressed such that particles can diffuse to rearrange into a crystalline structure. Given this observation, the open-loop policy is designed with a toggling scheme, where the magnetic field is periodically turned on and off at specific frequencies.

The authors pointed out that the toggling frequency is the key parameter in the performance, since the field should be turned off long enough to eliminate defects, but not too long that particles diffuse too far where a complete disassembly occurs. They further demonstrated that with a toggling frequency of around 0.66 Hz, well-ordered crystal can be formed after about 2000 s (Figure 7) [101].

Open-loop control is welcome given its simplicity. Strategies like the toggling scheme have also shown success in a variety of self-assembly processes in both experiments and simulations [52, 92]. In addition, open-loop control is the only option when system state measurement is challenging or unobtainable. However, in a stochastic process, such as the colloidal self-assembly, system dynamics are unique every time

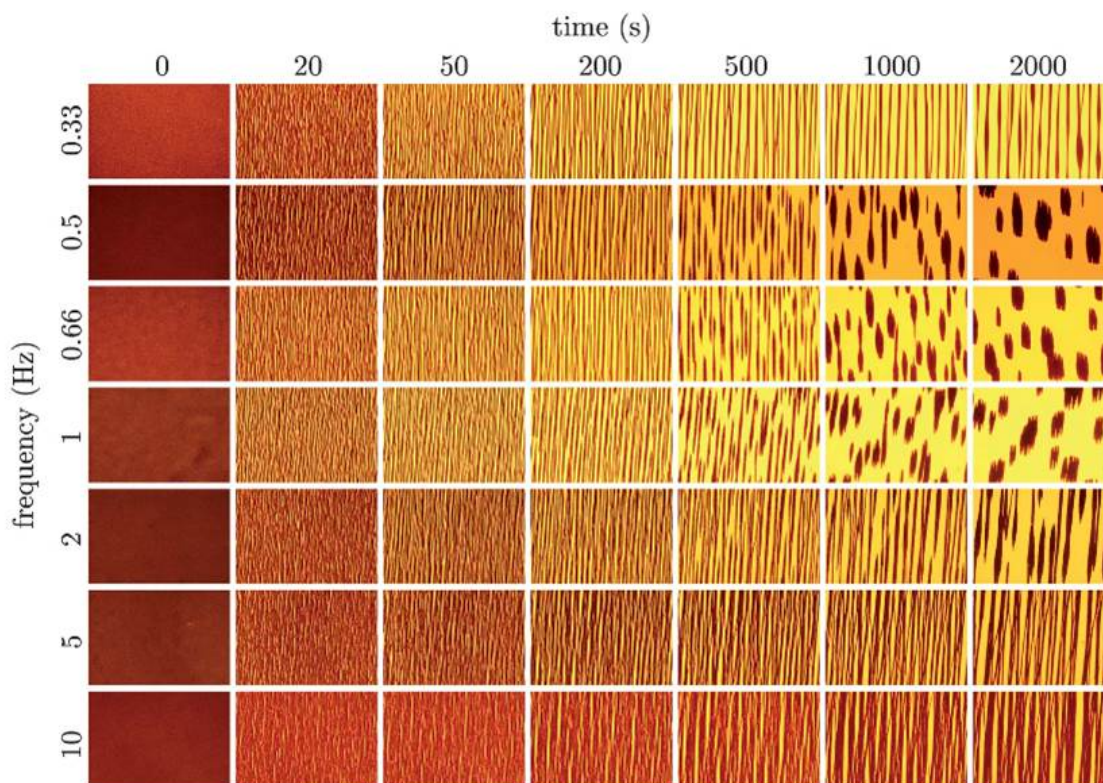


**Figure 7:** The suspension evolution after the pulsed magnetic field is applied as a function of the pulse frequency. Particle-rich regions of the suspension appear dark on the bright background of transmitted light. The field strength is 1500 Am. After 2000 s in the pulsed field all suspensions appear to have reached their terminal or at least slowly evolving state. While suspension condenses into large magnetic domains near 0.66 Hz, high pulse frequencies ( $\geq 5$  Hz) make the suspension remains percolated and the lowest pulse frequency makes the kinetics of depercolation appear to slow significantly [101]. Reproduced from [101] with permission from The Royal Society of Chemistry.

a new process is conducted. The loss of system state information makes an open-loop control strategy less robust compared to a closed-loop (i.e. feedback) control. Therefore, when system state measurement is available, closed-loop control could potentially improve the control performance.

#### 2.2.2.2 Closed-loop control

In closed-loop control policies, instant system information is measured and integrated into the control rules to identify the next step control input. Feedback control policies can be designed either with heuristic experiences, or model-based simulations.

In Ref. [54], a simple proportional controller is designed to experimentally control an electric field mediated colloidal self-assembly process for a defect free two-dimensional crystal (Figure 8). Each silica particle position is monitored with an optical microscope to calculate the order parameter  $C_6$  which quantifies the local crystallinity of the system, and serves as feedback to the controller. Low  $C_6$  indicates a disordered fluid configuration, and a high  $C_6$  value indicates an ordered hexagonal close packed structure, which this is the objective of the control.

The  $C_6$  evolution is manipulated by tuning the electric potential in the system via changing the input voltage level,  $V$  and the AC field frequency,  $\omega$ . When switched to low frequencies, the structure disassembles at a faster than diffusion speed, while a high frequency enables particle assembly at the center of the field, which is the free energy minimum of the system. The magnitude of the voltage determines to the strength of the compressing force, which drives the assembly of the particles. Thus the idea of the proportional control is to design the voltage and frequency in time, based on the instant  $C_6$  value, to navigate the system along a pre-specified  $C_{6SP}$  set point trajectory. The detailed proportional controller is given as,

$$[V, \omega] = \begin{cases} [-K\Delta C_6, 0.1 \text{ MHz}], & \Delta C_6 < \Delta C_{6T} \\ [K\Delta C_6, 1 \text{ MHz}], & \Delta C_6 \geq \Delta C_{6T} \end{cases} \quad (7)$$

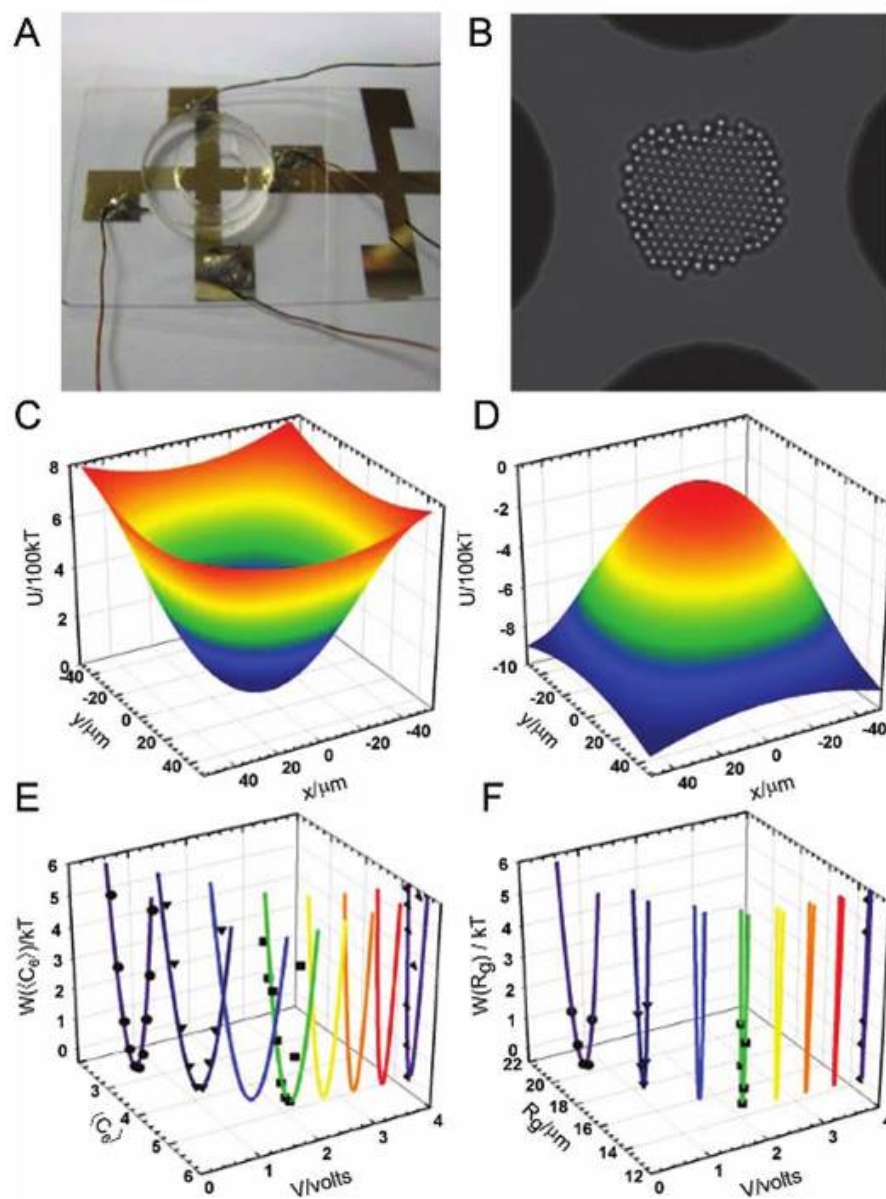


**Figure 8:** Experimental setup and top view of particle configurations under a microscope. System demonstrates opposite free energy landscape under different electric field frequencies, and the order parameter trajectories possess different characteristics under different voltage levels [54]. Reprinted from [54] with permission from John Wiley and Sons.

where  $K = 4V$  is the proportional gain determined with experimental observations, and  $\Delta C_6$  is the difference between the objective set point and the current system value, defined as  $\Delta C_6 = C_{6SP} - C_{6PV}$ . The authors reported that with the feedback proportional control policy, they were able to guide the assembly and disassembly of a 130 particle system along the predefined order parameter trajectories as in Figure 9 [54].

The study in Ref. [54] demonstrated the application of a classic control approach in an electric-mediated colloidal self-assembly process, with order parameters used to describe the system state. The success of the proportional controller also indicates that the control policy might be further improved for an optimal control if advanced control theories to be used.

One such advanced optimal control example is the application of model predictive control for rapid assembly of a two-dimensional  $\text{SiO}_2$  crystal in Ref. [105]. Model predictive control falls into the category of optimal control, where the control action is obtained by online computation. The basic concept of MPC is to use a dynamic model to forecast system behavior over a prediction horizon, and optimize the forecast to produce the best control move over the control horizon [81]. In MPC, an optimized input trajectory is designed at each control interval based on the current system state and the prediction from the model, subject to the constraints of the system. However, only the first control input is applied to the system at the next time step. This strategy ensures that the latest update of the actual measured output is considered in the optimization and accounts for the disturbance introduced by any uncertainties in the system [80, 81].

The system studied in Ref. [105] is similar to that of Ref. [54], with 210 particles. The dynamics of the system are modeled with a one-dimensional Langevin equation

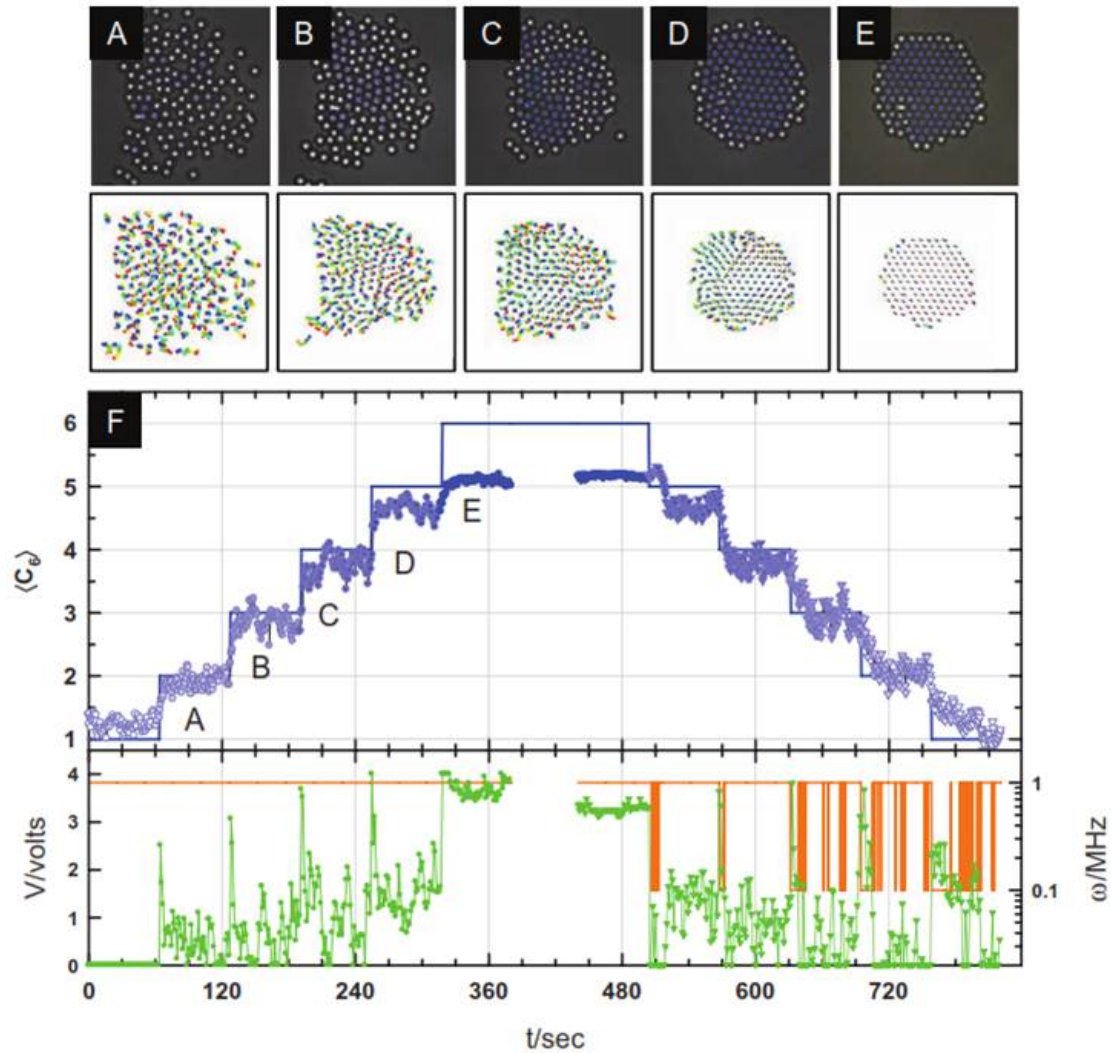


**Figure 9:** Dynamic feedback controlled assembly and disassembly of a colloidal crystal in terms of order parameter  $C_6$ . Experimental optical video microscopy images and particle trajectories for the assembly process with values of (A) 2, (B) 3, (C) 4, (D) 5, and (E) 6. The top image pane shows individual particle  $C_6$  with color scaling white for  $C_6 = 1$  and blue for  $C_6 = 6$ . Particle trajectories by linear spectrum scaled with red for  $t = 0$  and violet for  $t = 40$  s. Dynamic assembly and disassembly trajectories showing (top)  $C_{6SP}$  in solid blue line,  $C_{6PV}$  in shaded blue points vs. time and (bottom) electric field voltage,  $V$ , (green) and frequency,  $\omega$  (orange) vs. time [54]. Reprinted from [54] with permission from John Wiley and Sons.

using  $C_6$  as the state representation [105]. To achieve the optimal control, a time-discrete objective function  $J$  is defined and minimized,

$$J(x, u) = \sum_{k=1}^N J_k(x(k), u(k)) \quad (8)$$

where  $J_k(x(k), u(k))$  is defined as the cost at each time point  $k$  as following:

$$J_k(x(k), u(k)) = (x(k) - x_{target})^2 \quad (9)$$

where  $x_{target} = C_{6target} = 6$  indicates a perfect hexagonal crystal in a two-dimensional case, which is the objective of the control. The optimization is solved online using simulated annealing when a new measurement is available. The simulation results indicate that, with the online optimal control approach, a rapid assembly of a two-dimensional defect-free colloidal crystal can be achieved.

The optimal control action is calculated online, using the averaged prediction of several individual simulations. The optimization over an expected prediction is reasonable, considering the stochasticity of the system. However, as pointed out by the authors, the computational time of online optimization is prohibitively high to be implemented in experiments, which is a common issue with online computation.

Alternatively, optimal control policies can also be calculated offline. Examples of offline calculated optimal control policies for colloidal self-assembly include Ref. [13, 115]. In Ref. [13] a depletion-force mediated colloidal self-assembly process is studied. The osmotic pressure is manipulated as the global driving force for assembly. Two order parameters  $R_g$  and  $D_{cc}^*$  are used to describe the system states, and the control objective is to drive the system to a state with both a low  $D_{cc}^*$  and a low  $R_g$  value. Instead of MPC, a Markov decision process based optimization problem is formed, and dynamic programming is used to solve for the optimal control policy in the form of a lookup table. The Brownian dynamic simulation results demonstrate the feasibility of rapid assembly of ordered crystalline state with the offline computed optimal control policy [13].

### ***2.3 Summary***

Theoretical and simulation studies on colloidal self-assembly systems provided the foundation of accurately modeling the system with reduced system dimensions, such as order parameters. Representing systems with lower dimensions opens up the possibility of designing model-based control strategies. Imaging techniques enable real-time monitoring of the system dynamics evolution, which can provide not only an *in situ* measurement for control performance evaluation, but also a feedback in the closed-loop control. Current studies on colloidal self-assembly control with simple and advanced control theories also indicate the potential of an optimal control. The challenge addressed in this thesis is how to design an optimal control strategy that is applicable to experiments, and can also be generalized for a wide range of applications.

## CHAPTER III

### METHODS

#### *3.1 Colloidal System*

The experiment is set up at Johns Hopkins University as in Figure 10, where 300 micron-sized SiO<sub>2</sub> particles are suspended in a batch container with four electrodes to generate the electric field inside the system [104].

Coplanar quadrupole Au thin film electrodes were patterned on glass microscope coverslips as shown in Figure 10(a). The coverslips were prepared by 30 minutes sonication in acetone, 30 minutes sonication in isopropanol (IPA), and then were rinsed with deionized (DI) water, followed by 1 hour soak in Nochromix (Godax), then rinsed with DI water, sonicated in 0.1 M KOH for 30 minutes, rinsed again with DI water, and then were dried with N<sub>2</sub>.

The electrodes were fabricated by spin coating photoresist (S1813, Shipley) onto the microscope cover slips, treated with UV exposure through a chrome photomask, and physical vapor deposition of a 15 nm chromium adhesive layer and a 35 nm gold layer. The photoresist liftoff was accomplished with agitation in 1165 Remover (Shipley). The electrode tips are separated by  $\sim 100 \mu\text{m}$ . Before experiments, the coverslips with patterned electrodes were sonicated for 30 minutes in each of IPA, acetone, and IPA. Then were rinsed in DI water, suspended in Nochromix for 20 minutes, and rinsed with DI water again before they were dried with N<sub>2</sub>.

Experiments were performed in batch cells consisting of Viton O-rings. To construct batch cells, O-rings were coated with vacuum grease and sealed between the coverslip with the electrode and a glass coverslip. 22 gauge copper wires were attached to the electrode using conductive carbon tape. The electrode was then connected in

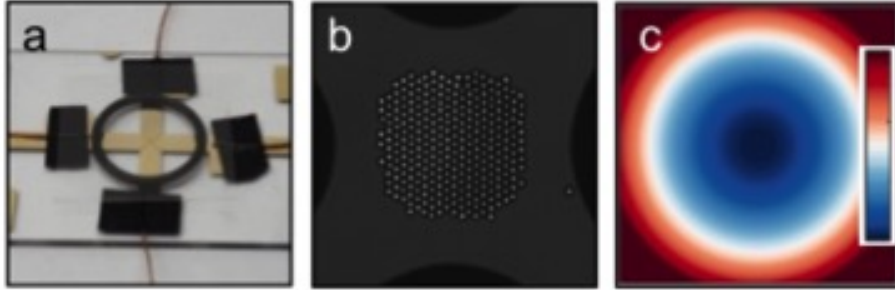


**Figure 10:** Experimental setup at JHU. (a) batch container with four electrodes attached to generate the electric field; (b) top view of 300  $\text{SiO}_2$  colloidal particles suspended in 1.0 mM NaOH solution under a microscope; (c) Single particle-field potential (blue-red scale: 0-100 kT [104]). Reprinted with permission from [104]. Copyright (2016) American Chemical Society.

series with a function generator (Agilent 33220a) with one lead attached to the north-south poles and another to the east-west poles. For experiments in Chapter 4, 100  $\mu\text{L}$  of the colloidal particle dispersion was dispensed into the batch cell and allowed to sediment for 5 minutes prior to sealing with a coverslip to obtain approximately 300 particles in the quadrupole. For experiments in Chapter 5, the dispersion was allowed to sediment for 15 minutes instead.

Microscopy was performed on an inverted optical microscope with a  $63\times$  Zeiss air objective lens (0.6 numerical aperture) at 1.25 magnification. A 12-bit CCD camera captured  $336 \text{ pixel} \times 256 \text{ pixel}$  ( $104 \mu\text{m} \times 79 \mu\text{m}$ ) digital images at rate of 10 frames/s. Image capture and analysis were performed using MATLAB Image Processing and Image Acquisition Toolboxes. Image analysis algorithms coded in MATLAB were used to simultaneously locate and track particle centers, as well as compute the order parameter values in real time. Figure 10(b) shows a top view of the particle configuration under a microscope.

Two order parameters,  $\psi_6$  and  $C_6$  are used to capture the formation of grain

boundary in the system. The global orientation parameter  $\psi_6$  describes the particle-particle bond orientation and is defined as,

$$\psi_6 = \left| \frac{1}{N} \sum_{j=1}^N \psi_{6,j} \right| \quad (10)$$

where  $N$  is the number of particles and  $\psi_{6,j}$  is the local six-fold bond orientation order of particle  $j$  defined as:

$$\psi_{6,j} = \frac{1}{N_{C,j}} \sum_{k=1}^{N_{C,j}} e^{i6\theta_{jk}} \quad (11)$$

where  $N_{C,j}$  is the number of neighbors within the first radius of gyration peak of particle  $j$ , and  $\theta_{jk}$  is the angle between particle  $j$  and each neighboring particle  $k$  with an arbitrary reference direction.

Connectivity between crystalline particles,  $\chi_{6,jk}$  is defined as,

$$\chi_{6,jk} = \frac{|Re[\psi_{6,j}\psi_{6,k}^*]|}{|\psi_{6,j}\psi_{6,k}^*|} \quad (12)$$

where  $\psi_{6,k}^*$  is the complex conjugate of  $\psi_{6,j}$ . The connectivity  $\chi_{6,jk}$  is used to compute the local order parameter for 6-fold connectivity  $C_{6,j}$  as,

$$C_{6,j} = \sum_{k=1}^{N_{C,j}} \left[ \begin{array}{cc} 1 & \chi_{6,jk} \geq 0.32 \\ 0 & \chi_{6,jk} < 0.32 \end{array} \right] \quad (13)$$

The local order parameter  $C_6$  is the averaged number of nearest neighbors over all the particles, and is defined as,

$$C_6 = \frac{1}{N} \sum_{j=1}^N \frac{C_{6,j}}{\langle C_6 \rangle_{HEX}} \quad (14)$$

where  $C_{6,j}$  is the local order six-fold connectivity, and  $\langle C_6 \rangle_{HEX}$  is the  $C_6$  value for 2D hexagonal close packed particles with a hexagonal morphology writes,

$$\langle C_6 \rangle_{HEX} = N^{-1}6(3S^2 + S) \quad (15)$$

$$S = -(1/2) + [(1/3)(N - 1) + (1/4)]^{1/2} \quad (16)$$

Combination of these two order parameters is able to capture the system evolution and quantify the ordering of the assembly. A state with both a low  $\psi_6$  and  $C_6$  value is the dispersed fluid state; state with high  $C_6$  but low  $\psi_6$  value is a defective state, with either vacancies or grain boundaries, or both; state with high  $\psi_6$  values automatically comes with a high  $C_6$  due to the physical meaning of the two order parameters, and this is the desired ordered crystalline state to be achieved.

### 3.2 *Brownian Dynamics Simulation*

System dynamics is simulated with detailed force balance analysis with Brownian dynamics simulation using the Cartesian coordinates of each particle, and Figure 10(c) shows the single particle-field potential at  $kT$ -scale. At the core of this BD simulation is a Langevin equation given for a particle with mass  $m$  as,

$$m \frac{d\mathbf{U}}{dt} = \mathbf{F}^H + \mathbf{F}^P + \mathbf{F}^B \quad (17)$$

where  $\mathbf{U}$  is the velocity vector,  $\mathbf{F}^H$  is the dissipative hydrodynamic forces,  $\mathbf{F}^P$  is the conservative forces due to the potential field, and  $\mathbf{F}^B$  is the Brownian forces, which is characterized with a mean and variance given by,

$$\langle \mathbf{F}^B \rangle = \mathbf{0} \langle \mathbf{F}^B(0) \mathbf{F}^B(t) \rangle = 2(kT)^2 (\mathbf{D}^{-1})(t) \quad (18)$$

where  $\mathbf{D}$  is a diffusivity tensor for finite number of particles above a no-slip plane that can be related to the resistance tensor via Stokes-Einstein relation [102].

Setting  $\mathbf{F}^H = -kY(\mathbf{D}^{-1}) \cdot \mathbf{U}$ , and use a midpoint algorithm to integrate the above equation gives the particle displacement equation as, with superscript “0” indicates quantities at the start of time,

$$\mathbf{r} = \mathbf{r}^0 + (\nabla \cdot \mathbf{D}^0) \Delta t + (kT)^{-1} \mathbf{D}^0 \cdot (\mathbf{F}^{P,0} + \mathbf{F}^{B,0}) \Delta t \quad (19)$$

The net conservative forces  $\mathbf{F}^P$  are calculated using the total conservative force acting on each particle  $i$  as,

$$\mathbf{F}_i^P = -\nabla_{r_i} [u_{de,i}^{pp} + u_{dd,i,j}^{pp}] \quad (20)$$

where  $u_{dd,i,j}^{pp}(\mathbf{r})$  is the electrostatic potential between particle  $i$  and  $j$ , writes,

$$u_{e,i,j}^{pp}(r_{ij}) = 32\pi\epsilon_m a \left(\frac{kT}{e}\right)^2 \tanh^2 \frac{e\psi}{4kT} \exp[-\kappa(r_{ij} - 2a)] \quad (21)$$

with  $r_{ij}$  being the particle center-to-center distance,  $e$  the element charge, and  $\psi$  the colloidal surface potential. The dipole-field,  $u_{de,i}^{pf}$  and dipole-dipole,  $u_{dd,i,j}^{pp}$  interactions are defined as,

$$u_{de,i}^{pf}(r_i) = -2kT\lambda f_{CM}^{-1} \left(\frac{E(\mathbf{r}_i)}{E_0}\right)^2 \quad (22)$$

$$u_{dd,i,j}^{pp}(\mathbf{r}) = -kT\lambda P_2(\cos\theta_{ij}) \left(\frac{2a}{r_{ij}}\right)^3 \left(\frac{E(\mathbf{r}_i)}{E_0}\right)^2 \quad (23)$$

where  $P_2(\cos\theta_{ij})$  is the second Legendre polynomial,  $\theta_{ij}$  is the angle between the line connecting two particle centers and the electric field, and  $\left(\frac{E(\mathbf{r}_i)}{E_0}\right)^2$  characterizes the radially electric varying field approximated with  $L = (x^2 + y^2)^{0.5}$  as,

$$\left|\frac{E(L)}{E_0}\right| = \frac{4L}{d_g} [2.081 \times 10^{-7} L^4 - 1.539 \times 10^{-9} L^3 + 8.341 \times 10^{-5} L^2 + 1.961 \times 10^{-5} L + 1.028] \quad (24)$$

The parameter used in this Brownian dynamics simulation is given in Table 1 to show: (a) colloidal particle size, (b) absolute temperature, (c) Debye screening length, (d) particle and wall Stern potential, (e) input levels, (f) Clausius-Mosotti factor for an AC field frequency at 1 MHz, (g) medium dielectric permittivity, and (h) electrode spacing. The detailed construction and validation of the BD simulation is given in Ref. [35].

The input  $\lambda$  is a dimensionless representation of the voltage, indicating the strength of the compressing force in the system. It is related to the voltage by [34],

$$\lambda(N, \kappa^{-1}) = \pi\epsilon_m a^3 \frac{[f_{CM} E_0(N, \kappa^{-1})]^2}{kT} \quad (25)$$

$$E_0(N, \kappa^{-1}) = 8^{-0.5} \frac{V_{pp}}{d_g} \quad (26)$$

$$V(N, \kappa^{-1}) = a_0(\kappa^{-1})^{-b_0(\kappa^{-1})} \quad (27)$$

$$a_0(\kappa^{-1}) = 7.15 + 4.10 \cdot 10^{-3} \kappa^{-1} \quad (28)$$

$$b_0(\kappa^{-1}) = 0.219 + 4.24 \cdot 10^{-4} \kappa^{-1} \quad (29)$$

where  $\kappa$ ,  $f_{CM}$ ,  $\epsilon_m$ ,  $E_0$ , and  $d_g$  are the same as in Table 1, and  $k$  is Boltzmann's constant. The peak-to-peak voltage,  $V_{pp}$ , is defined as  $V_{pp} = \alpha V(N, \kappa^{-1})$ , where  $\alpha \in [0, 1]$ , and  $V(N, \kappa^{-1})$  is the voltage at which all particles crystallize in a system of  $N$  particles.

### 3.3 Markov State Model

The use of particle coordinates in the BD simulation makes the simulation time consuming, and makes the design of control policies challenging. Therefore, Markov state models using order parameters  $\psi_6$  and  $C_6$ , are constructed with simulated samples from the Brownian dynamics simulation to approximate the system dynamics, and to compute the optimal control policy.

A Markov state model (MSM) is a stochastic model, which describes a memoryless time series, in which the future dynamics only depend upon the current state [19]. The MSM is characterized by a set of system states  $S$ , a set of feasible actions  $A$ , a probability transition time  $\Delta t$ , and a probability transition matrix  $P(a)$  composed of the transition probability  $P(a)_{ij}$  for the system to be in state  $j$  given the current state  $i$  under an input  $a \in \mathbb{A}$ , after a transition time  $\Delta t$ . When the system state and the

**Table 1:** Parameters for BD simulations.

Parameter	Value
$2a$ (nm) <sup>a</sup>	2870
$T$ (K) <sup>b</sup>	298
$\kappa^{-1}$ (nm) <sup>c</sup>	10
$\psi$ (mV) <sup>d</sup>	-50.0
$\lambda$ <sup>e</sup>	0.2, 0.9, 2.0, 19.7
$f_{CM}$ <sup>f</sup>	-0.4667
$\epsilon_m/\epsilon_0$ <sup>g</sup>	78
$d_g$ ( $\mu\text{m}$ ) <sup>h</sup>	96

control action are continuous, the number of feasible control policies are infinite, this will cause computational issues in solving for the optimal control policy, i.e. “curse of dimension” in dynamic programming. Therefore, in this study, we discretize both the system state defined by the two order parameters, and the control action space defined by the voltage, or its dimensionless representation  $\lambda$ . Besides, assuming the dynamics in the system does not differ significantly over time, a time-invariant transition matrix is used, where the transition probability  $P(a)$  does not change over time.

The time-invariant transition matrix is estimated with order parameter trajectories from Brownian dynamics simulation. To calculate the transition probability  $P(a)_{ij}$ , the number of transitions ending in state  $j$  starting from state  $i$  is counted and divided by the total number of transitions from state  $i$ . Let  $d_k = (i_0, i_1, \dots, i_k)$  denotes the history of the process up to time  $k$ , and  $N$  the total number of the discrete state, then the Markov transition probability satisfies the following relationship:

$$P(a)_{i_k j} = P(a)_{d_k j} \quad (30)$$

$$\sum_{j=1}^{j=N} P(a)_{ij} = 1 \quad (31)$$

If there are no transitions observed coming out from a state  $i$ , that state is deemed as an absorbing state, in which once the system gets in there, it will not transit to any other states. Mathematically, the probability of the system in an absorbing state  $i$  satisfies,

$$P(a)_{ij} = \begin{cases} 1, & \text{if } j = i \\ 0, & \text{other wise} \end{cases} \quad (32)$$

### 3.4 *Dynamic Programming*

#### 3.4.1 Markov Decision based Optimization Framework

To compute the optimal control policy, a Markov decision process based optimization process is formulated. A MDP is characterized by  $T, S, A, P(A)$ , where  $S, A, P(A)$  are

defined previously, and  $T$  is the set of the discrete time epoch  $k$  [79]. If  $T$  is infinite, the process is called an infinite-horizon MDP, and the resulting control policy has a static structure. Otherwise, a finite-horizon MDP, and the corresponding control policy has a time-dependent structure. In this thesis, both infinite- and finite-horizon MDP are studied.

In the infinite-horizon MDP, the optimization is achieved over an infinite number of time steps, and the policy is designed to maximize the objective function at each state:

$$J^\pi(x) = E \left\{ \sum_{k=0}^{\infty} \gamma^k R(x_k, a_k) \right\} \quad (33)$$

where  $E$  is the expectation operator, and  $\pi : S \rightarrow \mathbb{A}$ , is a feasible policy composed of control actions  $a_k \in \mathbb{A}$ ,  $x_k \in \mathbb{S}$  is the discrete state,  $k$  is the discrete time instant, and  $\gamma \in (0, 1)$  is the discount factor introduced to ensure the convergence of the optimization [12]. The one-stage reward function  $R(x_k, a_k) : S \times A \rightarrow \mathbb{R}$  is obtained when the system is in state  $x$  and control action  $a$  is taken. The design of the objective function is aimed to obtain the highest possible reward at each time step.

In the finite-horizon MDP, the optimization is achieved over a finite number of time steps, with the objective function defined as:

$$J^\pi(x) = E \{ R(x_{t_f}, a_{t_f}) \} \quad (34)$$

where  $R(x_{t_f}, a_{t_f})$  denotes the reward at the terminal time point  $t_f$ . The design of the policy is aimed to maximize the reward at the end of process.

The one-stage reward function  $R(x, a)$  for both the finite- and the infinite-horizon MDP policy is defined the same as  $R(x_k, a_k) = \psi_6^2$ . Order parameter  $C_6$  was not explicitly included in the objective for several reasons: first, a high  $\psi_6$  state automatically ensures a high  $C_6$  value, due to their physical relationship; second,  $C_6$  contributes more toward state classification and its inclusion in the objective function does not significantly affect the control policy, according to our investigations.

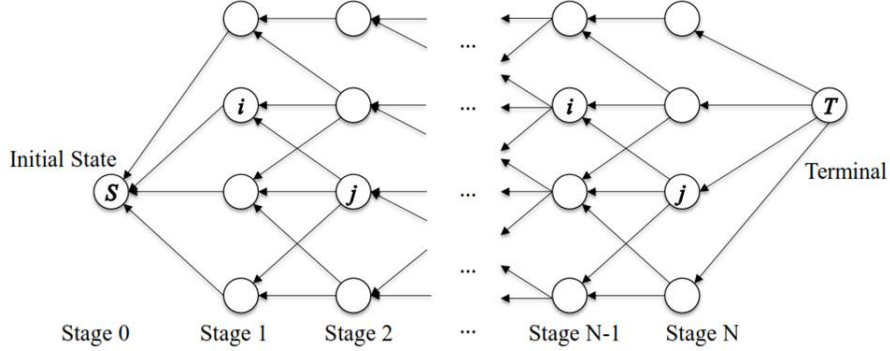


**Figure 11:** A backwards conduction algorithm in dynamic programming for finite-horizon Markov decision process based optimization.

The optimal value function  $J^*$  and the optimal policy  $\pi^*$  for both the finite- and infinite-horizon MDP control policies are defined as,

$$J^*(x) = \sup_{\pi \in \Pi} J^\pi(x) \quad (35)$$

$$\pi^*(x) = \arg\{\sup_{\pi \in \Pi} J^\pi(x)\} = \arg J^*(x) \quad (36)$$

where “sup” indicates the supremum, and  $\Pi$  is the set of all feasible control policies.

### 3.4.2 Algorithms for Dynamic Programming

The finite-horizon MDP option is solved with a backwards conduction algorithm, and the infinite-horizon MDP optimization is solved with a policy iteration algorithm. Both algorithms are provided in the MATLAB MDP Toolbox [23].

The backwards conduction algorithm starts at the last time period  $T$ , computes the value function for each feasible state and then step back another time period until it reaches the initial time (Figure 11). The outline of one such algorithm is given as following, with  $V_t(S_t)$  is the reward or value function obtained in state  $S_t$  which is the set of all feasible states at time  $t$  [77].

1. Initialization:

- Initialize the terminal contribution  $V_T(S_T)$ .

- Set  $t = T - 1$ .
2. Calculate:
 
$$V_t(S_t) = \max_{a_t} \{C_t(S_t, a_t) + \gamma \sum_{s'} P(s'|S_t, a_t) V_{t+1}(s')\}$$
 for all  $S_t \in S$ .
  3. If  $t > 0$ , decrement  $t$  and return to step 1. Else stop.

The policy iteration algorithm starts with an initial feasible policy  $\pi$ , and calculates the associated value function and updates the action in the current policy in each iteration to achieve the maximum reward/value function. Below is one example of the policy iteration [77].

1. Initialization:
  - Select a policy  $\pi^0$ .
  - Set  $n = 1$ .
2. Given a policy  $\pi^{n-1}$ :
  - Compute the one-step transition matrix  $P^{\pi^{n-1}}$ .
  - Compute the contribution vector  $c^{\pi^{n-1}}$  where the element for state  $s$  is given by  $c^{\pi^{n-1}}(s) = C(s, A^{\pi^{n-1}})$ .
3. Let  $v^{\pi, n}$  be the solution to:
 
$$(I - \gamma P^{\pi^{n-1}})v = c^{\pi^{n-1}}$$
4. Find a policy  $\pi^n$  defined by
 
$$a^n(s) = \arg_{a \in A} \max(C(a) + \gamma \sum_{s'} P(s'|s, a) v^{\pi, n})$$
 This requires computing an action for each state  $s$ .
5. If  $a^n(s) = a^{n-1}(s)$  for all states, then set  $a^* = a^n$ ; Else set  $n = n + 1$  and return to step 1.

## CHAPTER IV

### PROOF-OF-PRINCIPLE

Perfectly ordered states are targets in diverse molecular to micro-scale systems involving for example atomic clusters, protein folding, protein crystallization, nanoparticle superlattices, colloidal crystals, etc. However, there is no obvious approach to control the assembly of perfectly ordered global free energy minimum structures; near-equilibrium assembly is impractically slow, and faster out-of-equilibrium processes generally terminate in defective states.

In this chapter, the application of the proposed framework in Figure 3 is demonstrated on a colloidal system elaborated in Section 3.1 for a proof-of-concept purpose. An infinite-horizon MDP based optimal policy is computed with dynamic programming featuring four inputs:  $\lambda = 0.2$ ,  $\lambda = 0.9$ ,  $\lambda = 2.0$ , and  $\lambda = 19.7$ . The results in this chapter demonstrate that by tracking real-time stochastic particle configurations and adjusting the applied fields with feedback, the evolution of the assembly process can be guided through polycrystalline states into single domain crystals an order of magnitude faster than the near-equilibrium approach.

#### *4.1 Introduction*

Perfectly ordered nano- and micro- colloidal structures possessing exotic properties can be used as metamaterials for multidisciplinary applications [8, 36, 73, 99]. However, obtaining perfect structures is non-trivial at any scale (e.g., atomic clusters, nanoparticle superlattices, folded proteins), either due to the unmanageable amount of time needed or the formation of defects in a fast assembly process.

Crystallization kinetics depends on how constituents collectively assemble via diffusion in the solution. When the diffusion rate is fast enough to be experimentally

manageable, perfect crystals can be formed via near-equilibrium assembly. Examples include directional growth from a seed crystal and single small protein crystals for X-ray crystallography via combinatorial screening. These near-equilibrium assemblies are usually achieved with the use of predefined processing recipes, based on slow nucleation, growth, and annealing to allow the constituents gradually assemble and relax into global free energy minimum perfect crystals. When the diffusion rate is too slow to be experimentally accessible, like in the micron-sized colloidal self-assembly systems, such near-equilibrium is usually impractical. However, rapid out-of-equilibrium assembly, like using externally applied electric force to compress particles, usually results in meta-stable states and persistent defective structures.

Here, a static feedback optimal control strategy is developed to control the defects formed in an out-of-equilibrium colloidal self-assembly system (Figure 12) for rapid production of two-dimensional perfect crystals. Specifically, a quadrupolar electric field is used to generate a tunable compressing force between the particles for assembly. The system under different compressing force possesses different free energy landscapes and renders different particle configurations. Therefore the problem to solve here is equivalent to using a global thermodynamic variable (i.e., electric field) to change the relative free energy of all configurations, thus guiding particles to assemble via thermal motion to minimize their free energy.

To enable feedback control in real-time and real-space, the essential capabilities include: (1) system state monitoring via image analysis with microscopy, (2) particle interaction manipulation to navigate energy landscapes via field mediated potentials (i.e changing the field amplitude), and (3) actuator settings assignment based on feedback via an optimal policy as lookup table. This approach provides defects correction in real-time to produce perfect crystals experimentally for the first time.

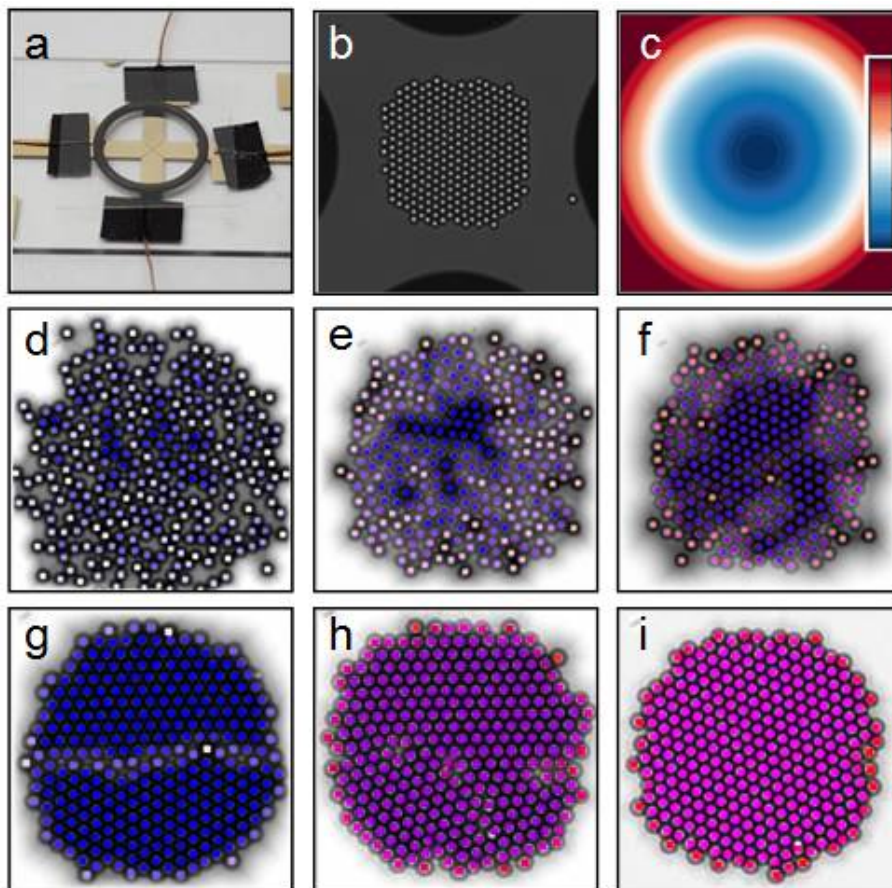


**Figure 12:** Quasi-2D colloidal crystal assembly in electric fields. (a) Microfabricated quadrupole electrode. (b) Optical microscopy image of particles within quadrupole. (c) Single particle-field potential (blue-red scale: 0-100 kT). Images of 300 particles with centers colored to visualize reaction coordinates for local hexagonal order,  $C_6$  in blue, and global hexagonal order,  $\psi_6$  in red, at electric field amplitudes of  $\lambda =$  (d) 0.2, (e) 0.9, (f) 2.0, and (g, h, i) 19.7. Representative micro-structures include bicrystals with, (g) large grain boundary (similar sized domains near max misorientation angle), (h) small grain boundary (dissimilar sized domains with smaller misorientation angle), (i) no grain boundary i.e., perfect crystal [104]. Reprinted with permission from [104]. Copyright (2016) American Chemical Society.

## 4.2 Methods

### 4.2.1 Experimental Control

Radius of gyration,  $R_g$  defined in Eqn. 37, was used to measure the degree of melting between individual cycles. After a perfect crystal was obtained or 1000 s had elapsed, the system was melted at  $\lambda = 0.2$  until  $R_g = 25.5 \mu\text{m}$  before the next cycle was started.

$$R_g = 0.5N^{-1} \left[ \sum |r_i - r_j| \right]^{0.5} / R_{g,HEX} \quad (37)$$

where  $R_{g,HEX}$  is the radius of gyration for 2D hexagonally close packed particles with regular polygon morphologies given by,

$$R_{g,HEX} = 5^{0.5} 3^{-1} a N^{0.5} \quad (38)$$

The particle location is identified as the brightness maxima within an image taken under the optical microscope, and this is deemed as the centroid of the particle. The accuracy of the particle location detection is affected by the variation in the lighting intensity over the image, the variation in the particle size and shape, as well as the resolution of the measurement. To account for the particle tracking errors in the experiments, order parameter  $\psi_6$  is normalized by  $\psi_{6,max} = 0.8$ , and  $C_6$  is normalized by  $C_{6,max} = 0.95$  before use in the lookup table for updating  $\lambda$ . All the experiments in this chapter were conducted by Brad Rupp at Johns Hopkins University.

### 4.2.2 Markov State Model Construction

The set of control actions in the Markov state model in this chapter is composed by the four  $\lambda$ 's. The state space defined by  $(\psi_6, C_6)$  is discretized evenly into 6000 discrete states, with  $\psi_6$  into 50 intervals and  $C_6$  into 120 intervals after trial-and-error inspection.

Four MSMs are constructed and for each model, BD simulations are initialized in different discrete states to cover a commonly visited region of the state space.

The parameters used in the BD simulation are summarized in Table 1 in Section 3.2 of this thesis. The simulations were repeated to ensure the important states have enough samples to account for stochastic effects. Simulations were conducted under both constant and time-varying inputs to enrich sampling, with voltage switching at intervals of  $\Delta t = 100$  s, corresponding to the transition time used in the MSM.

### 4.3 *Stochastic Polycrystal Assembly*

Assembly is performed with 300 SiO<sub>2</sub> colloids (radius,  $a = 1.4 \mu\text{m}$ ) confined by gravity into a quasi-2D layer within a quadrupole electrode, as shown in Figure 12(a) (also refer to Section 3.1 of this thesis). A function generator controls the amplitude of a 1 MHz AC field, which determines the degree of localization of colloids at the field minimum in the quadrupole center, as shown in Figure 12(b), monitored with a microscope. In the electric field, shown in Figure 12(c), particles are induced into dipoles, and the driving force for the assembly is characterized by the dipole-field potential as [55],

$$u(\mathbf{r}) = -\lambda f_{CM}^{-1}[E(\mathbf{r})/E_0] \quad (39)$$

where  $\lambda = \pi_m a^3 (f_{CM} E_0)^2 / (KT)$  characterizes how strongly the radially varying field,  $E(r)/E_0$ , confines particles relative to thermal energy,  $kT$ ,  $\mathbf{r}$  is the particle location. The Clausius-Mosotti factor for an AC field  $f_{CM}$  depends on the particle dielectric property,  $\epsilon_p$ , and the medium dielectric property  $\epsilon_m$  [2]. The detailed information on the experiments are given in Table 2. where (a) colloidal particle size, (b) absolute temperature, (c) Debye screening length, (d) particle and wall Stern potential, (e) peak-to-peak voltage, (f) input levels, (g) Clausius-Mosotti factor for an AC field frequency at 1 MHz, (h) medium dielectric permittivity, and (i) electrode spacing.

A balance of the field confinement against the quasi-2D dispersion osmotic pressure determines, for systems with a given particle number, whether a fluid or solid phase, as shown in Figure 12(d)-(i), will form versus  $\lambda$  [34]. As system size increases,

polycrystallinity, i.e. misoriented crystal domains with grain boundaries shown in Figure 12(g) and (h), becomes increasingly prevalent under rapid assembly with a stronger compression force; this is the defect to be repaired.

Order parameters  $\psi_6$  and  $C_6$  are used to capture different states include: amorphous states with both a low  $C_6$  and  $\psi_6$  value in Figure 12(d), polycrystals in Figure 12(g) with high  $C_6$  but low  $\psi_6$  value, and the perfect crystals in Figure 12(h) with a  $\psi_6$  value close to 1.  $C_6$  captures emergence of crystallinity during condensation and distinguishes the amorphous (low  $C_6$ ) and the polycrystalline (high  $C_6$ ) states, that both have a near to 0  $\psi_6$  value.

## 4.4 Results

### 4.4.1 Uncontrolled Simulations with Ramp

To understand the tradeoff between slow near-equilibrium assembly and rapid out-of-equilibrium processes, simulations are conducted with four open-loop ramp schemes and a quench scheme where  $\lambda = 19.7$  is used along the process. Four ramps are considered where input  $\lambda$  increases from 0.2 to 19.7 in: 1000 s, 2000 s, 5000 s, and 10000 s respectively, to include both slow near-equilibrium ramp and rapid out-of-equilibrium ramp.

Assembly trajectories are reported for  $N = 300$  particles in Brownian Dynamic

**Table 2:** Parameters for Experiments.

Parameter	Value
$2a$ (nm) <sup>a</sup>	2870
$T$ (K) <sup>b</sup>	293
$\kappa^{-1}$ (nm) <sup>c</sup>	10
$\psi$ (mV) <sup>d</sup>	-50.0
$V_{pp}/V^e$	0.2, 0.4, 0.6, 0.95
$\lambda^f$	0.2, 0.9, 2.0, 19.7
$f_{CM}^g$	-0.4667
$\epsilon_m/\epsilon_0^h$	78
$d_g$ ( $\mu\text{m}$ ) <sup>i</sup>	96

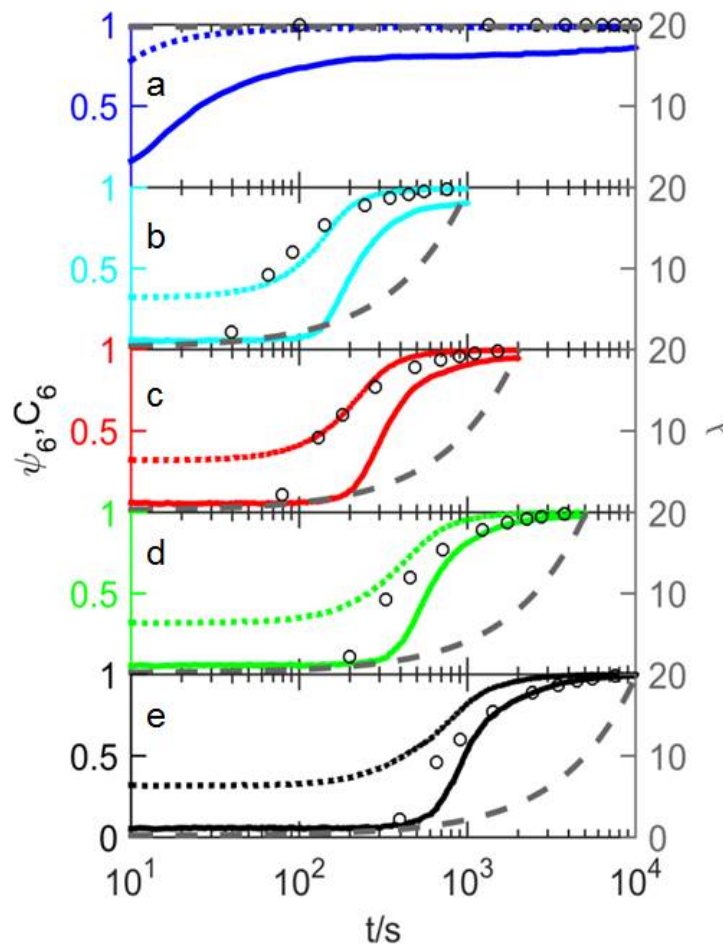


**Figure 13:** Ramping electric field at different rates without feedback control. Electric field amplitude,  $\lambda$  (long-dash gray), ramped from 0.2 to 19.7 over (a) 0 s (blue), (b) 1000 s (cyan), (c) 2000 s (red), (d) 5000 s (green), and (e) 10000 s (black). Local order,  $C_6$  (dotted lines), emerges before global order,  $\psi_6$  (solid lines). Equilibrium  $\psi_6$  values (open circles) vs.  $\lambda$  approach  $\psi_6$  ramp trajectories only for the 10000 s ramp case. Reprinted with permission from [104]. Copyright (2016) American Chemical Society.

(BD) simulations matched to experiments [35]. Non-equilibrium order parameter trajectories averaged over 100 simulations are shown alongside the equilibrium  $\psi_6$  values (i.e., free energy minima values at each  $\lambda$ ) in Figure 13. To obtain the equilibrium  $\psi_6$  values, BD simulations starting from fluid states are conducted under each  $\lambda$  to construct free energy landscapes in the order parameter space via linear fitting a Smoluchowski equation coefficients. The free energy minimum on each landscape is deemed as the equilibrium  $\psi_6$  for that  $\lambda$ . The detailed fitting is provided in supplementary information of Ref. [104].

According to Figure 13, local ordering always precedes global ordering, and in order to achieve a 100% perfect crystals out of the 100 simulations, a near-equilibrium ramp of 10000 s is needed. Note that ramped  $\psi_6$  approaches equilibrium  $\psi_6$  values at long ramp times. On the contrary, as the ramp time reduces, more defective crystals form since faster ramps produce non-equilibrium polycrystals that do not relax to single crystals in the allotted times.

#### 4.4.2 Feedback Control Policy

The  $(\psi_6, C_6)$  coordinates quantitatively capture non-equilibrium stochastic trajectories between states, and provide a dynamic model to close the feedback control loop. A  $(\psi_6, C_6)$  based model quantifies the field mediated crystallization dynamics via a Smoluchowski equation given as [35],

$$\frac{\partial p(\mathbf{x}, \lambda, t)}{\partial t} = \nabla(\mathbf{x}, \lambda) \cdot \frac{1}{kT}(\mathbf{x}, \lambda) + \nabla]p(\mathbf{x}, \lambda, t) \quad (40)$$

where  $p(\mathbf{x}, \lambda, t)$  is probability,  $x = (\psi_6, C_6)$ ,  $D$  is a diffusivity landscape, and  $W$  is a free energy landscape. With this dynamic model, an optimal control scheme based on free energy gradients in  $W$  and hydrodynamic mediated friction in  $D$  can be formulated [35].

Controlling the colloidal self-assembly is thus conceptually the navigation of free

energy landscapes,  $W$ , at each electric field amplitude,  $\lambda$ , as shown in Figure 14(a). The equilibrium ramp in Figure 13(e) can be interpreted as slowly increasing  $\lambda(t)$  to guide the configuration evolve near the free energy minimum on each  $W$ . Faster ramps in Figure 13(a)-(d) cause sampling of non-equilibrium polycrystalline states on each  $W$  instead. In these non-equilibrium states, vanishing gradients in  $W$  provide minimal driving force for relaxation, therefore more defective states are formed.

The more sophisticated approach here is to determine the optimal  $\lambda(t)$  based on current  $(\psi_6, C_6)$  coordinates to maximize the probability of moving from the initial fluid state to the perfect crystal. The particle and grain boundary motion are stochastic such that each process is unique, no one  $\lambda(t)$  is best every time the process is conducted. Therefore closed-loop control is required to obtain the optimal actuation.

A Markov decision process based dynamic programming optimization framework is formulated to compute for the optimal control policy. Markov state model [19], a discretized version of the Smoluchowski equation, characterized by a “probability transition matrix” to quantify the transition probability between all states during a time step,  $\Delta t$ , is constructed for each  $\lambda$ . The optimal control policy,  $\pi^*(\mathbf{x})$  is solved by maximizing an infinite-horizon objective function given in Eqn. 41, and is defined as in Eqn. 42, with the optimal value function  $J^*$  defined in Eqn. 43.

$$J^\pi(\mathbf{x}) = E \left\{ \sum_{t=0}^{\infty} \gamma^t R(\mathbf{x}_i, \lambda_i) \right\} \quad (41)$$

$$\pi^*(\mathbf{x}) = \arg\left\{ \sup_{\pi \in \Pi} J^\pi(x) \right\} = \arg J^*(\mathbf{x}) \quad (42)$$

$$J^*(\mathbf{x}) = \sup_{\pi \in \Pi} J^\pi(\mathbf{x}) \quad (43)$$

where  $E$  is the expectation operator and  $R(\mathbf{x}_i, \lambda_i)$  is the reward function at time  $i$

defined as  $R = \psi_6^2$  to maximize the crystallinity on each stage. The discount factor  $\gamma = 0.99$  is used to ensure the convergence of the policy calculation.

The optimal policy  $\pi^*(\mathbf{x})$  was solved using a MATLAB policy iteration algorithm [23]. It provides a mapping from the current measured state,  $\mathbf{x}$ , to the next step action,  $\lambda$ , i.e.  $\lambda_{i+1} = \pi^*(\mathbf{x}_i)$ , where  $i$  is the discrete time instant, and is given in the form of a look-up table in Figure 14(b), indicating the  $\lambda$  to use when assembly trajectories pass through each  $(\psi_6, C_6)$  coordinate.

A typical single experimental trajectory is plotted in Figure 14(a) and (b) to illustrate the mechanism of the control policy. System state  $(\psi_6, C_6)$  coordinates plotted as trajectories on the  $W$  at each  $\lambda$  in Figure 14(a), are updated every 100 ms using image analysis to locate each particle centers. The current values of the  $(\psi_6, C_6)$  coordinates are used in the look-up table in Figure 14(b) to update  $\lambda$  every 100 s, which is shown by the trajectories jumping between the  $W$  in Figure 14(a). The policy update time of  $\Delta t = 100$  s was determined by considering actuation times comparable to the inherent system response time.

The policy update time and inherent system response time depends on the cooperative short-range motion of particles necessary for grain boundary motion [95, 121], which can be estimated from the long time self-diffusivity as,  $D_S^L = D_S^S[1+2\phi g(2a)]^{-1}$ , where  $D_S^S$  is the short time self-diffusivity,  $\phi$  is the particle area fraction, and  $g(2a)$  is the radial distribution function contact value within the quasi-2D colloidal monolayer [6]. Using  $D_S^S=0.5D_0$  where  $D_0$  is the Stokes-Einstein value, to account for particle-wall hydrodynamics [40], and the hard disk fluid radial distribution function for  $g(2a)$  [120], the time for particles to diffuse over a distance comparable to their own radius,  $\tau = a^2/D_S^L$  is about 100 s at low concentrations. By considering how the soft electrostatic repulsion between particles significantly decrease  $g(2a)$  [6],  $D_S^L$  becomes a weak function of  $\phi$ , therefore  $\tau \approx 100$  s captures the characteristic structure relaxation time scale for all configurations and  $\lambda$ . Estimating  $D_S^L$  based on dense fluid

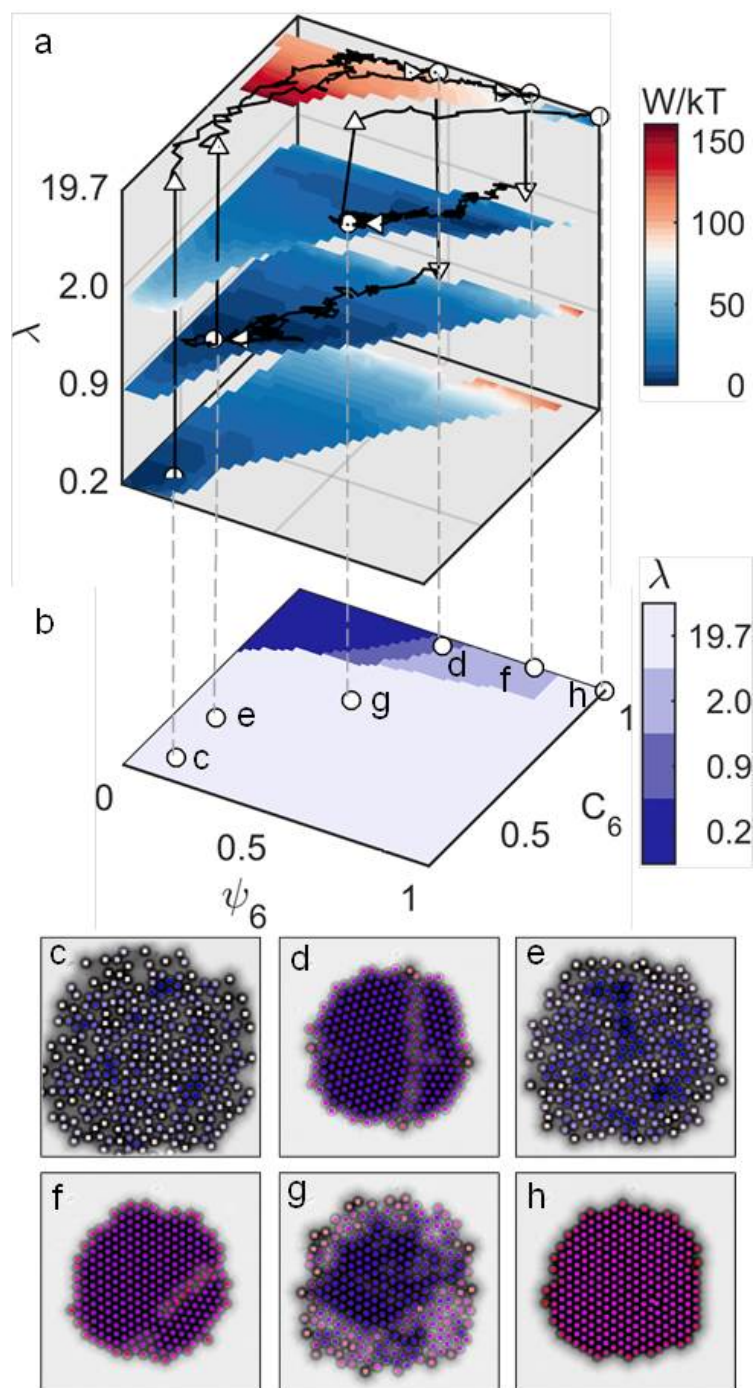


**Figure 14:** Assembly trajectory on energy landscapes under control. (a) Free energy landscapes of 300 particles at the four  $\lambda$ s in policy. Example trajectory (black) with coordinates on policy (b) and corresponding images (c-h). (b) Optimal policy calculated using Markov decision process. Images showing representative configurations with the same coloring scheme as in Figure 12(d)-(i) at: (c)  $\lambda = 0.2$  before compression, (d) first compression to  $\lambda = 19.7$  with grain boundary, (e) relaxation at  $\lambda = 0.9$ , (f) re-compression at  $\lambda = 19.7$  with new grain boundary, (g) relaxation at  $\lambda = 2.0$ , (h) perfect crystal at  $\lambda = 19.7$  [104]. Reprinted with permission from [104]. Copyright (2016) American Chemical Society.

properties can be rationalized since motion within grain boundaries has been compared to concentrated melt dynamics [4, 69, 122]. In addition, the different  $\lambda$  values in conjunction with the inhomogeneous field cause the dynamics to vary significantly from the concentrated interior of the particle ensemble to the vanishing density at its periphery [34]. Moreover, the 100 s update time worked better than faster or slower times, consistent with the above analysis.

The single experimentally controlled trajectory indicates that low  $\lambda$ 's are used for particle rearrangement only when defective states are formed, and  $\lambda = 19.7$  is used for rapid compression. Depending on the severity of the grain boundary, different low levels of  $\lambda$  are used to relax the assembly.

#### 4.4.3 Controlled versus Uncontrolled Assembly

To collect sufficient statistics for a fair comparison of the uncontrolled (i.e. quench) and controlled processes, 200 alternating uncontrolled and controlled cycles were conducted in a fully automated experiment over 31 hr (see Section 3.1 of this thesis). Each cycle used feedback control to: (1) ensure initial disassembly, (2) execute either a step-quench without intervention or 100 s control updates, and (3) terminate the process after either a perfect crystal is obtained or 1000 s elapsed.

The first 10 cycles of the alternating experiments (even cycles for controlled and odd cycles for uncontrolled) illustrate several scenarios (Figure 15a) that: (1) quick relaxation for small grain boundaries to form perfect crystal in the uncontrolled cycle #3, #7, and #9; (2) slow relaxation within 1000 s to form a perfect crystal in uncontrolled cycle #1; (3) formation of meta-stable crystals that never relax in uncontrolled cycle #5; (4) formation of perfect crystals either without (#4, #10) or with (#2, #6, #8) several feedback corrections.

The controllers success at producing perfect crystals is better illustrated via analysis of all the 200  $\psi_6$  versus time trajectories as shown in Figure 15(b), and the number

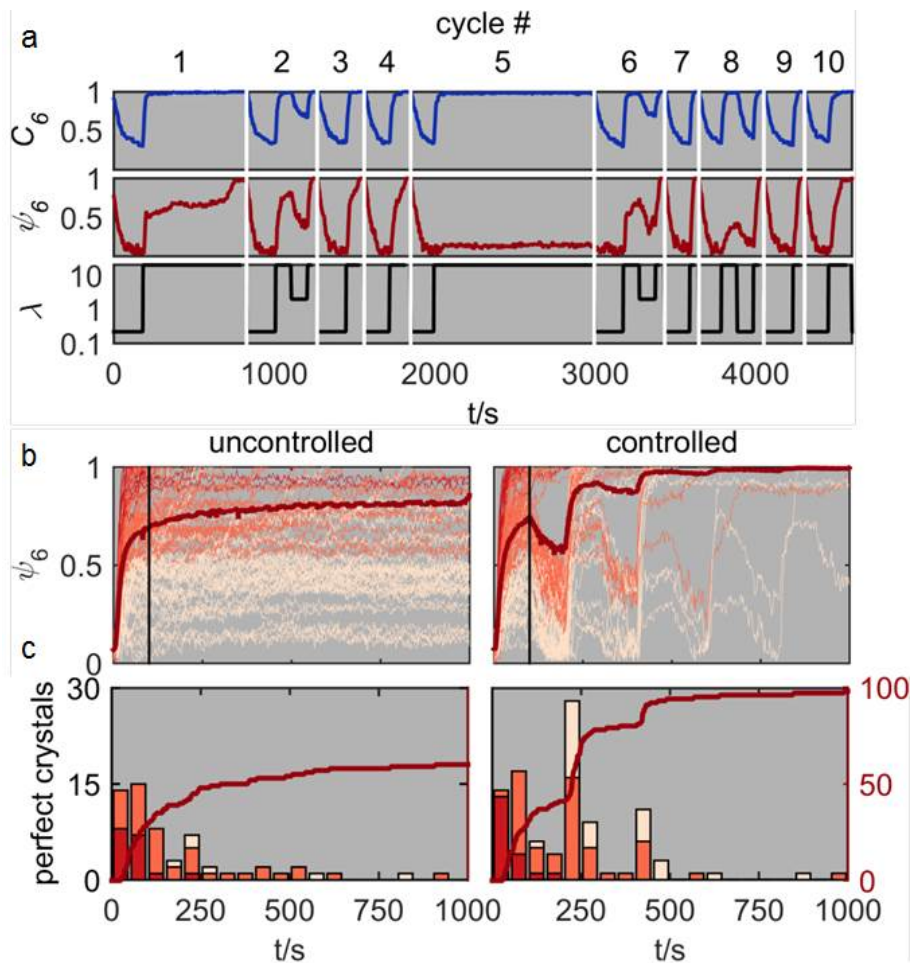


**Figure 15:** Controlled vs. uncontrolled crystal assembly processes. 100 uncontrolled and 100 controlled trajectories shown as: (a) first 10 cycles with  $C_6$  (blue),  $\psi_6$  (red),  $\lambda$  (black) vs. time, (b)  $\psi_6$  vs. time for 1000 s for all experiments colored to indicate ensemble average (bold red), no grain boundary (red:  $\psi_6 > 0.7$ ,  $C_6 > 0.95$ ), small grain boundary (orange:  $0.7 > \psi_6 > 0.4$ ,  $C_6 > 0.95$ ), large grain boundary (peach:  $0.4 > \psi_6$ ,  $C_6 > 0.95$ ), (c) perfect crystals vs. time as cumulative number (dark red) and instantaneous number (bars) with same color scheme as (b) [104]. Reprinted with permission from [104]. Copyright (2016) American Chemical Society.

of perfect crystals versus time as shown in Figure 15(c). Perfect crystals form immediately under the strong compression at  $\lambda = 19.7$  without grain boundaries in a small portion of the 200 cycles (17 uncontrolled vs. 19 controlled), by bypassing slow grain boundary motion on free energy plateaus, i.e.  $W$  at  $\lambda = 19.7$  in Figure 14(a).

The remaining trajectories confirm the interpretation, made with the single trajectory in Figure 14(a), of how control removes grain boundaries by choosing lower  $\lambda$ . In cycles where small grain boundaries form, perfect crystals are obtained in 100% (52/52) of trajectories after 1–2 corrective steps using the optimal control policy, whereas 78% (37/47) of small grain boundary bicrystals are able to relax for perfect crystals in the uncontrolled cycles. In cycles where large grain boundaries form, perfect crystals are obtained in 93% (27/29) of controlled trajectories after 3–4 corrective steps with the control policy; while only 18% (6/34) of uncontrolled processes reached a perfect crystal. In sum, with the control policy, processes produced perfect crystals 98% of the time while uncontrolled processes were 60% successful.

#### 4.4.4 Conclusion

This chapter proves the success of the proposed framework in controlling the colloidal self-assembly to rapidly produce perfect 2-dimensional crystal. Building on understanding of the free energy landscape at different global actuator input levels and the corresponding particle configurations, the optimal control policy is able to navigate the assembly process in order parameter space to achieve a  $\sim 40\%$  improvement in the yield of perfect crystals compared to the simple quench scheme. The out-of-equilibrium assembly approach resulted from the optimal control policy also reduced an order of magnitude amount of process time compared to the near-equilibrium assembly.

## CHAPTER V

### EXPANSION OF THE FRAMEWORK

The previous chapter demonstrated the feasibility of the proposed framework and the benefits of the static model-based optimal feedback policy compared to quench and near-equilibrium assembly approaches. This chapter widens the scope of the previous chapter to compare closed-loop optimal policies with the commonly used open-loop “toggling” approach, where the input is periodically switched between the high and low levels. In addition, the MDP optimization framework is also expanded beyond the infinite-horizon closed-loop policy, to include a finite-time policy, where the policy structure is time-dependent. The time-dependent policy enables a more direct comparison to toggling and more directly incorporates the objective of achieving crystalline assembly at the end of the process.

#### *5.1 Introduction*

Directed self-assembly describes a process in which directing agents, external fields, or templates are intentionally manipulated to influence the assembly process [44]. As described in the previous chapters that, there is a tradeoff between the speed of the assembly and the crystallinity of the assembled structure in a directed colloidal self-assembly process. To address this issue, time-varying assembly has been used including slow voltage ramps to anneal to the perfect crystal [107], and toggling of the magnetic field to periodically relax out defects [101]. However, these open-loop strategies do not address the stochastic nature of defect formation. If the formation of a defect could be detected early and healed locally and quickly before getting locked in, it might be possible to achieve rapid assembly without the inefficiency of unneeded

relaxations that slow down the assembly. There has been limited application of closed-loop feedback control in colloidal assembly, including heuristic switching rules applied in simulation [60], and proportional control applied in experiments [54], as well as the previous simulation [13, 115], and experimental [104] approaches for model-based control underpinning the results presented in the previous chapter.

To understand the similarities and the differences between the open-loop and the closed-loop control strategies, five strategies are compared in this chapter, with three open-loop strategies including a heuristic time-invariant strategy, a heuristic time-varying strategy, and a model-based time-varying strategy; together with two model-based closed-loop strategies including a policy with a time-independent structure, and a policy with a time-dependent structure. All the strategies use the same update time step of 100 s and the same two voltage levels. All strategies run for 900 s, which is long enough to achieve the desired crystalline state. The design of these strategies is aimed to understand the effects of time-varying actions and the use of system state as feedback in controlling this stochastic self-assembly process. To provide a fair comparison, all the MSM-based policies in this study use the same MSM.

## **5.2 *Methods***

### **5.2.1 Experimental Control**

Radius of gyration,  $R_g$  defined as in Eqn.37, was used to measure the degree of melting between individual cycles. A new experimental cycle was initiated when  $R_g = 25.5 \mu\text{m}$  is reached after melting the system at  $\lambda = 0.2$ .

To prepare for the experiments, 100  $\mu\text{L}$  of the colloidal particle dispersion was dispensed into the batch cell and allowed to sediment for 15 minutes prior to sealing with a coverslip, to obtain approximately 300 particles in the system. Same as in Chapter 4, to account for particle tracking errors, experimental values of the system metrics  $\psi_6$  and  $C_6$  in this chapter were calibrated, normalized by constants of  $\psi_{6max}$

= 0.85 and  $C_{6max} = 0.98$ , before use as feedback in the closed-loop strategies.

### 5.2.2 Markov State Model Construction

The set of control actions in the Markov state model in this chapter is composed by the two  $\lambda$ 's. The state space defined by  $(\psi_6, C_6)$  is discretized evenly into 6000 discrete states, with  $\psi_6$  into 50 intervals and  $C_6$  into 120 intervals after trial-and-error inspection.

To estimate the transition probabilities, we used a time-varying input trajectory, where the input is switched (uniformly) randomly between  $\lambda = 0.2$  and  $\lambda = 19.7$  every 100 s, to generate samples from the detailed Brownian dynamic simulation. The parameters used in the BD simulation are summarized in Table 1 in Section 3.2 of this thesis.

The design of a dynamic input is aimed to reach states excited by the switches that are challenging to obtain under either of the constant input values. Simulations were initiated and repeated in about 400 different discrete states to ensure sampling of the commonly visited state space under each of the two input levels. Samples from constant inputs were also included to enrich the sample set. We then estimated the transition matrix  $P(a)$  using a moving window strategy elaborated as Counting Method 1 in Ref. [74], for each of the two input levels. A total of about 1600 BD simulations including both short time (900 s) and long time ( $\sim 5000$  s) runs were used in the transition matrix estimation. It took about 4 hours to finish a 900 s BD simulation realization using.

### 5.3 Order Parameters and Control Policies

To make a direct comparison with a periodic toggling strategy [101], we consider two voltage levels:  $0.1V$  and  $0.95V$ , where  $V$  is the lowest voltage to completely crystallize the system within a 2-dimensional planar space as defined in [34]. The corresponding dimensionless representations of the two input levels are defined as  $\lambda = 0.2$  and  $\lambda$

= 19.7 respectively, to indicate the strength of the electric compression force in the system [53, 104].

Markov state models are constructed for the two input levels using two order parameters  $\psi_6$  and  $C_6$  as the system state representation. With these two order parameters, we are able to distinguish: the fluid state in Figure 16(a), which only exists under  $\lambda = 0.2$ ; defective states in Figure 16(b) and (c), formed due to the strong compression force under  $\lambda = 19.7$ ; and the ordered state in Figure 16(d), which could only be achieved and maintained under high voltage (i.e.  $\lambda = 19.7$ ). The ultimate goal of the control is to achieve a grain boundary free state as in Figure 16(d). Detailed information on the  $\lambda$ -voltage conversion and the order parameters is given in Chapter 3 of this thesis.

#### 5.3.0.1 *Open-loop policies*

The first open-loop strategy is the Constant policy, where  $\lambda = 19.7$  is used from the beginning to the end of the process, since a highly crystalline state can not be achieved when  $\lambda = 19.7$  is used. The second open-loop strategy is the Periodic policy, where the input is switched between the two input levels every 100 s, starting and ending with  $\lambda = 19.7$ . The third open-loop approach is calculated with Markov chain Monte Carlo simulation using the MSMs as follows: first, we enumerated all the possible combinations ( $2^9$ ) of the actions over the nine time steps (900 s/100 s). Then we used the MSMs to predict and identify the policy that gives the highest final crystallinity according to its  $\psi_6$  value. This input series is the optimal open-loop control policy. This policy is referred as “Optimal OL” for short.

#### 5.3.0.2 *Closed-loop control strategies*

The two closed-loop control policies were solved to include a finite-horizon policy (i.e. “FinCL”), and an infinite-horizon policy (i.e. “InfCL”), with the formulation described in Chapter 3 of this thesis. The control policy was solved with dynamic

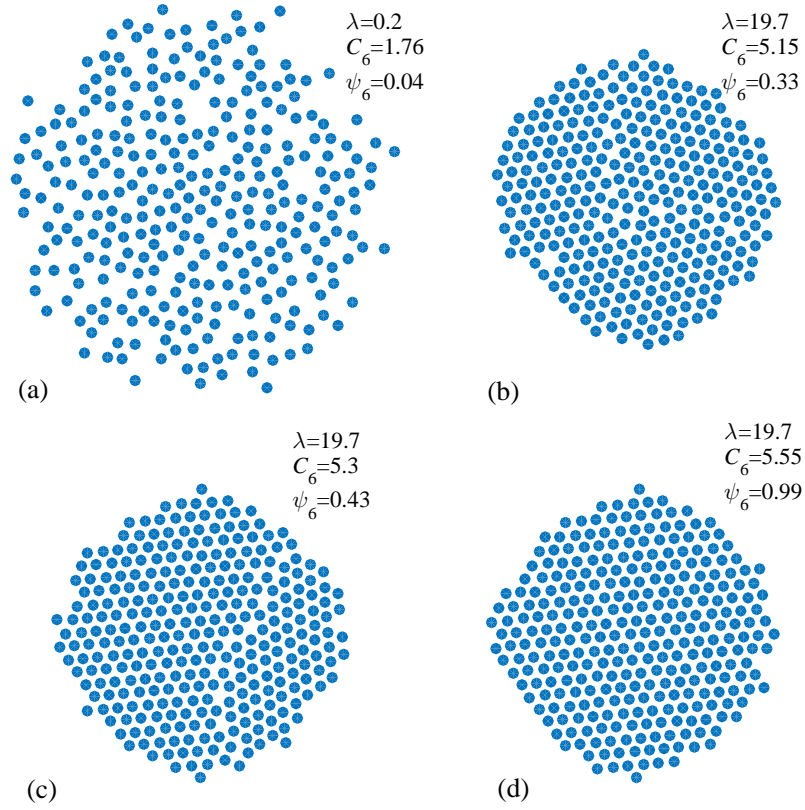


**Figure 16:** Typical assembly configurations with order parameter values from simulation under different input levels: (a) fluid-like state, which only exists under low input  $\lambda = 0.2$ ; (b) and (c) polycrystalline and grain boundary states, formed under high input  $\lambda = 19.7$ ; (d) the desired defect-free structure only achievable under high input  $\lambda = 19.7$ .

programming via a backwards conduction algorithm for the finite-horizon MDP option, and via a policy iteration algorithm for the infinite-horizon MDP optimization. Both policies were calculated using the MATLAB MDP Toolbox [23]. For both cases, solving for the optimal control policy takes only a few seconds on a 3.40 GHz Intel(R) Xeon(R) CPU with 16.0 GB memory.

## 5.4 Results

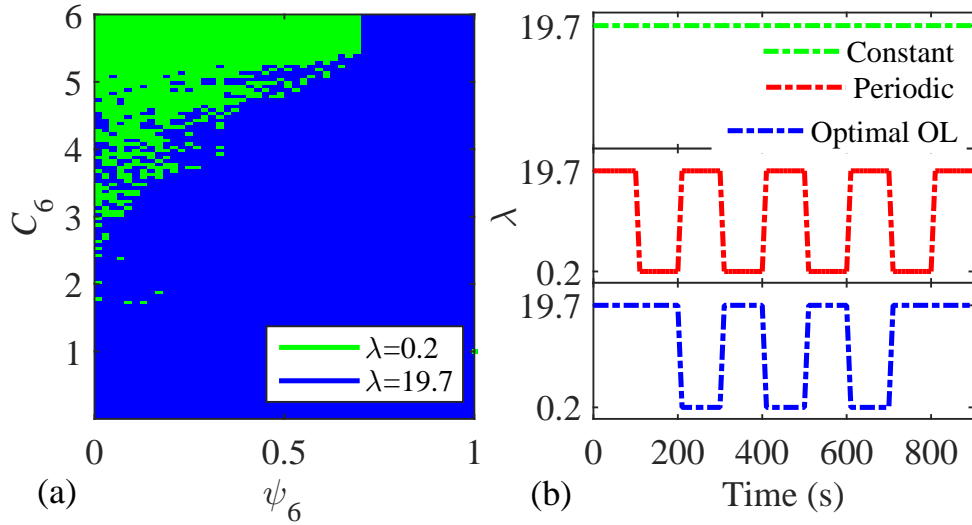
### 5.4.1 Calculation of Control

Figure 17(a) shows the infinite-horizon optimal closed-loop control policy in the reduced state space and Figure 17(b) shows the three open-loop control strategies. Figure 4 shows the 900 s finite-horizon optimal closed-loop control policy, with each panel representing the policy for the corresponding 100 s time interval. Since  $\lambda = 19.7$  is used for the 800 s to 900 s period to maintain the structure, it is not shown for simplicity. In the finite- and infinite-horizon control policies, states with a  $C_6$  value higher than about 5.5 are not reachable in either experiments or simulation [54]. However, to provide a complete presentation, actions in these states were extrapolated given information on nearby states.

The input in the open-loop strategies is updated only according to time, regardless of system state. In contrast, to use the closed-loop control policies, a picture of the colloidal system is taken under the microscope and analyzed to calculate first the intensity centroid of each particle, and then the two order parameter values. From the order parameters, the input  $\lambda$  level for the next 100 s is found directly from the look-up tables in Figure 17(a) or Figure 18. Control actions for each of the five strategies are updated every 100 s.

### 5.4.2 Performance in Brownian Dynamic Simulation

The open-loop and closed-loop policies were evaluated by performing 100 realizations of the BD simulations for each of the five control strategies. Specifically, ten different



**Figure 17:** (a) infinite horizon control policy shown as a lookup table in order parameter space; (b) three open loop schemes with optimal open-loop control policy developed from MSM colored in blue, Periodic strategy in red, and Constant in green.

initial configurations were used, with each taken from the lower-left “fluid” region of the state space. Ten different realizations (i.e. different initial seeds in the random number generator) were conducted, beginning in each of the ten initial configurations, for each control strategy. The results are illustrated in Figure 19, for 900 s long BD simulations. The system is deemed to be a perfect assembly when the value of  $\psi_6$  is greater than 0.95, and the yield is the fraction of the perfect assemblies at the current time.

The use of a constant voltage led to significant defects, as quantified in Table 3 by a final yield of 54%. However, the other four strategies, both open- and closed-loop, all led to assembly yields greater than 90%. While the assembly under constant voltage is highly stochastic, forming graining boundaries about half of the time, the other two open-loop strategies employ time-varying inputs that create robust operating policies without the need for feedback.

The values in Table 3 suggest that a closed-loop strategy might be somewhat

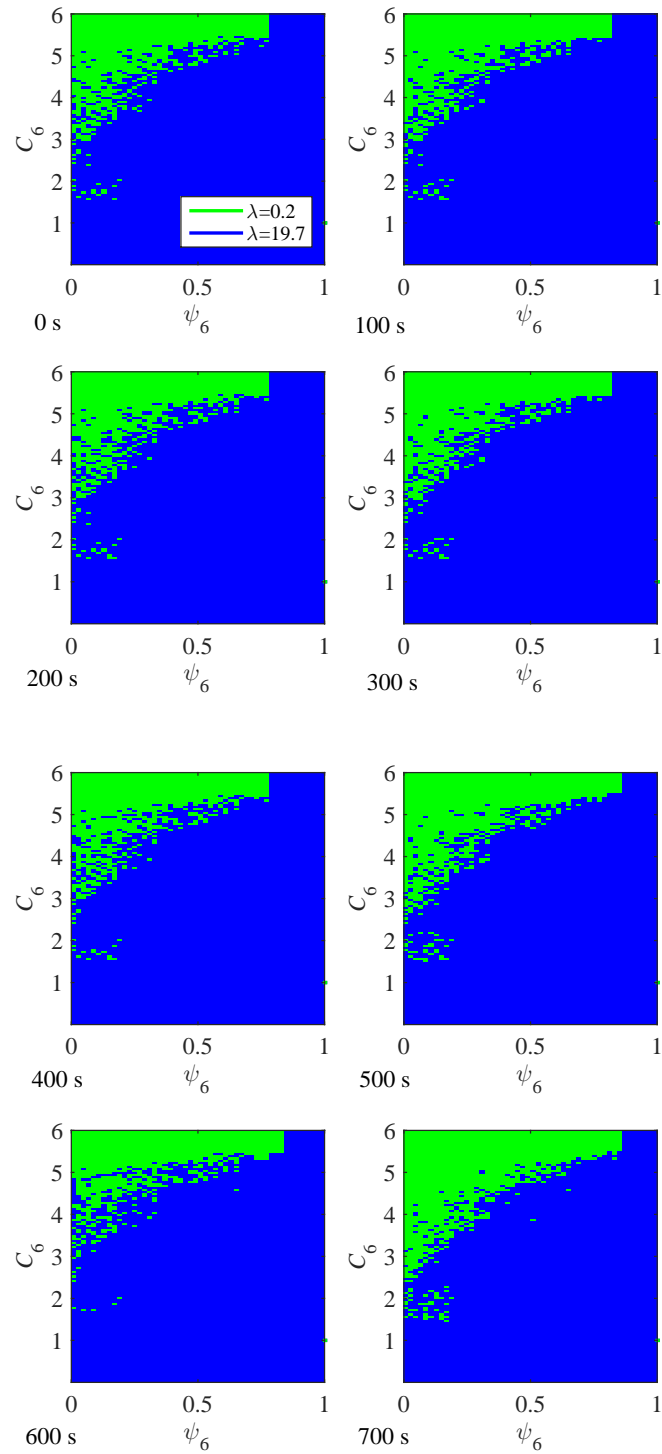


**Figure 18:** 900 s finite horizon optimal control policy. Each lookup table presents the control policy for its corresponding 100 s interval, with the last (9th) 100 s interval using  $\lambda = 19.7$  to maintain the crystal structure.

faster and more effective than an open-loop strategy. However, using a two-sided t-test with a 95% confidence level, it is not possible to resolve any significant differences in performance between the strategies, other than the constant input. Figure 20 provides additional qualitative insight on the potential differences between the open- and closed-loop performance, by comparing individual realizations that use the same initial configuration and the same seed for the random number generator. The system successfully assembles without defects under all three strategies, as shown in Figure 20. Note that the input profile used for the periodic and closed-loop realizations is identical up until 500 s, and therefore so are the corresponding trajectories. In the closed-loop policy shown at the bottom, two relaxation periods are needed, but the system is on a good path at 500 s, not requiring any additional relaxation. In contrast, in the upper panel under periodic input, the system undergoes another relaxation between 500 and 600 s that was not needed, unnecessarily delaying the assembly process. Additional relaxation is applied from 700 to 800 s, taking the system from the defect-free state to a relaxed state and then back to the crystalline state by the end of the 900 s process.

**Table 3:** BD yield and assembly time of 100 realizations

	>50% Time (s)	>80% Time (s)	Yield
Constant	500	N/A	54.0%
Periodic	260	640	92.0%
Optimal OL	330	590	92.0%
InfCL	260	560	91.0%
FinCL	260	560	95.0%

### 5.4.3 Performance in Experiments

The same five control policies were then applied to the experiments, and all the experiments in this chapter were conducted by Jianli Zhang at Johns Hopkins University.

Due to time constraints, it was not practical to perform 100 repetitions of each of the five strategies (it took over 30 hr to perform 200 experimental cycles [104]).

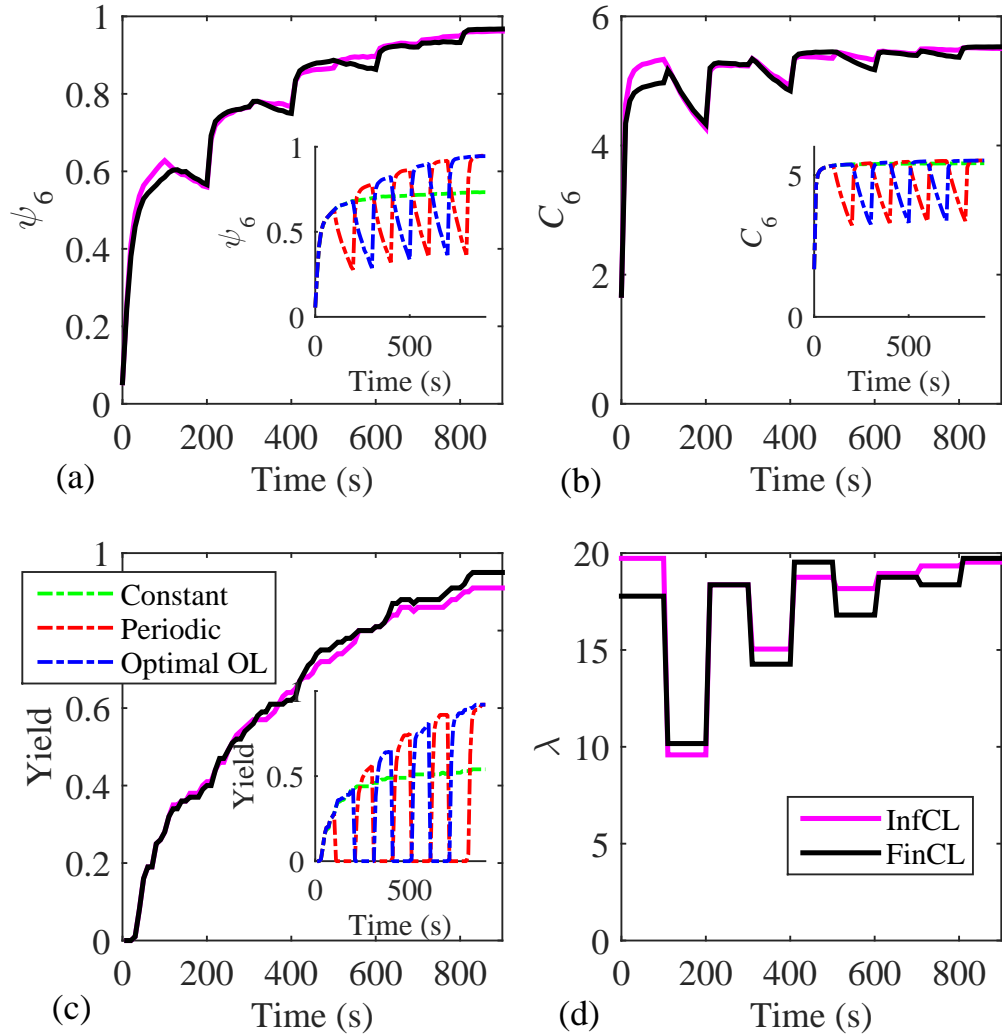


**Figure 19:** 100 realization averaged BD simulations with results from open-loop strategies plotted in the inset figures. (a)  $\psi_6$  evolution over time; (b)  $C_6$  evolution over time; (c) cumulative yield of grain boundary free structures over time; (d) averaged input profiles from closed-loop control strategies.

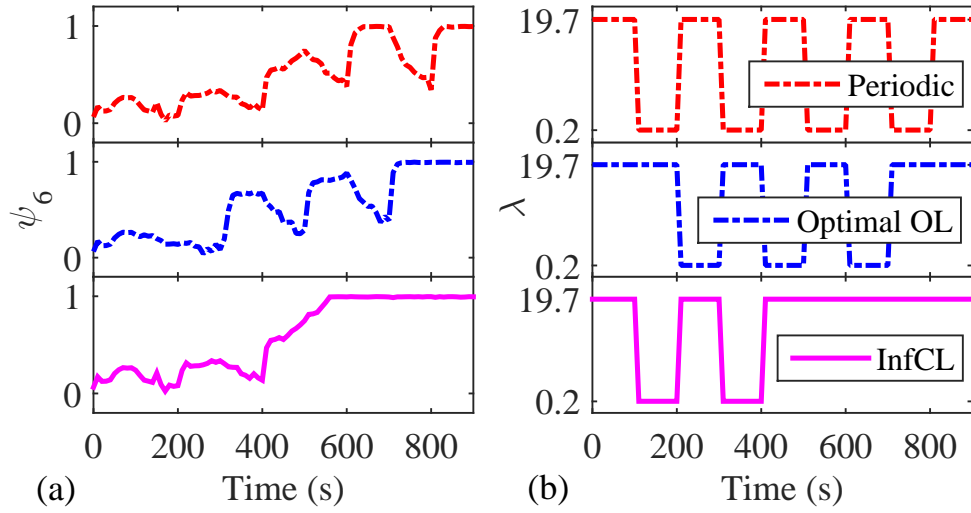


**Figure 20:** Individual BD simulation runs from Periodic, Optimal OL, and InfCL control strategies, showing the corresponding control mechanism. (a)  $\psi_6$  trajectories over time; (b) control input profiles. All three simulations were initiated in the same configuration and were simulated with the same seed.

Instead, ten repetitions were performed for each of the five strategies over the full assembly time of 900 s. Moreover, 30 additional repetitions were performed for each strategy, but each of these runs was stopped once the system had reached a perfect crystal (i.e.  $\psi_6 > 0.95$ ), to save time. If a perfect crystal had not been obtained by 900 s, then that run was stopped.

Figure 21 shows the results averaged over the ten repetitions of the full 900 s process. The closed-loop policies result in high yield, consistent with the BD simulation results. At some point in the process, both of the closed-loop strategies can be seen to achieve a yield of 10 out of 10, indicating that all of the runs did assemble and could have been stopped at that point. However, under the high input level, particles are still subject to Brownian motion, which leads to changes in particle positions that contribute to a  $\pm 0.02$  deviation from 0.95 in  $\psi_6$  value, even if a defect-free assembly is present. Since we have used 0.95 as the criterion for a yield, this phenomenon eventually resulted in the fluctuations in the yield of the two closed-loop control results

as in Figure 21(c). In contrast, the maximum yield observed for the constant input is 0.7, suggesting that three of the ten runs had a persistent grain boundary.

The most striking difference between the BD simulations and the experiments is seen in the other two open-loop policies. Although the yield for the open-loop optimal policy reaches 0.8 early in the process, it subsequently degrades. The periodic policy never reaches a yield above 0.6. This is a qualitatively different behavior than that seen in the BD simulations, where a relaxation followed by a high voltage always leads to a ratcheting up of  $\psi_6$  and thus the corresponding yield (see Figure 20 as an example).

A closer inspection of individual runs in Figure 22 confirms this interpretation. Under the periodic trajectory, the system reaches its highest value of  $\psi_6$  at 500 s. The subsequent relaxations and assembly cycles result in reduced crystallinity. Similar behavior is seen in the optimal open-loop run (middle plot). The level of crystallinity at 600 s is lower than at 400 s. The system does recover somewhat at 800 s, but it still fails to assemble by the end of the 900 s process. These typical results suggest that the relaxation and re-assembly dynamics in the BD simulation are not fully capturing what is actually occurring in the experiments—thus highlighting the need for feedback to confer robustness to the assembly process to compensate for unmodeled dynamics.

However, the nature of the feedback that is required may potentially be simpler than the closed-loop optimal policies that are presented here. A simpler alternative for feedback is simply to stop the process once  $\psi_6$  exceeds a value of 0.95. By applying a high voltage at the time when assembly is first detected, the crystalline structure may be locked in. This simple feedback approach is referred to here as “endpoint detection”.

This endpoint detection feedback strategy was applied in the experiments over 30 repetitions, as described previously. In addition, the ten repetitions that ran until the full 900 s were also analyzed from this point of view, with the point of first assembly

used as the endpoint of the process. The results based on all 40 repetitions of the five strategies are summarized in Table 4. The endpoint detection did not really help with the constant strategy. In this case, the grain boundaries are locked in by the high voltage, and without relaxation of the voltage they are unlikely to heal. However, a high final yield was achieved for the other four strategies. The open-loop optimal policy achieves a fast time to 50% yield, due to its 200 s of high voltage at the beginning of the process. However, this does not necessarily incur long-term advantage, as the time to achieve 80% yield is not statistically distinguishable from the other three policies. Overall, it appears that all four strategies use a similar alternating pattern of high and low voltage to relax out grain boundaries. Feedback is needed to determine when the system has achieved a highly crystalline assembly, so that it is not destroyed by subsequent relaxations.

**Table 4:** Experimental yield and assembly time of 40 cycles

	>50% Time (s)	>80% Time (s)	Yield
Constant	230	N/A	65.0%
Periodic	250	470	95.0%
Optimal OL	110	400	97.5%
InfCL	240	450	92.5%
FinCL	270	450	95.0%

#### 5.4.4 Discussion and Conclusion

The periodic open-loop strategy that was considered here worked well, especially when combined with endpoint detection. This is consistent with previous theoretical and experimental studies, which showed “toggling” to be beneficial compared to constant conditions [101]. The periodic strategy can be further optimized, by choosing the two voltage levels, the frequency, and the duty cycle. Moreover, a periodic strategy with more than two levels could be considered. As the number of parameters grows, this “simple” strategy becomes more difficult to design and optimize. Fundamentally, it is a special case of the open-loop optimal strategy presented here, in which periodicity

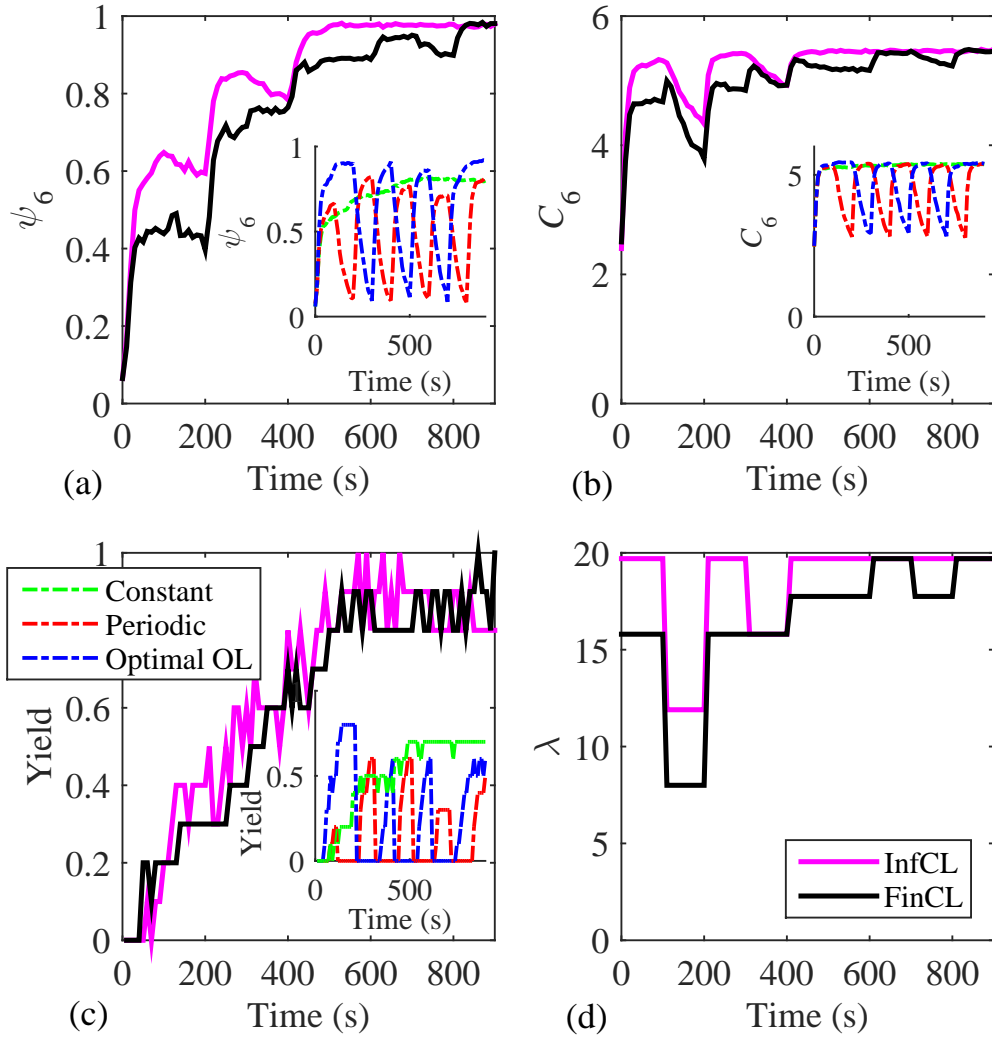


**Figure 21:** 10 cycles averaged experimental results of the five strategies, with closed-loop controlled results plotted in the main figure and the open-loop controlled results in the inset figures. (a)  $\psi_6$  evolution over time; (b)  $C_6$  evolution over time; (c) cumulative yield of grain boundary free structures over time; (d) averaged input profiles used in the experiments.

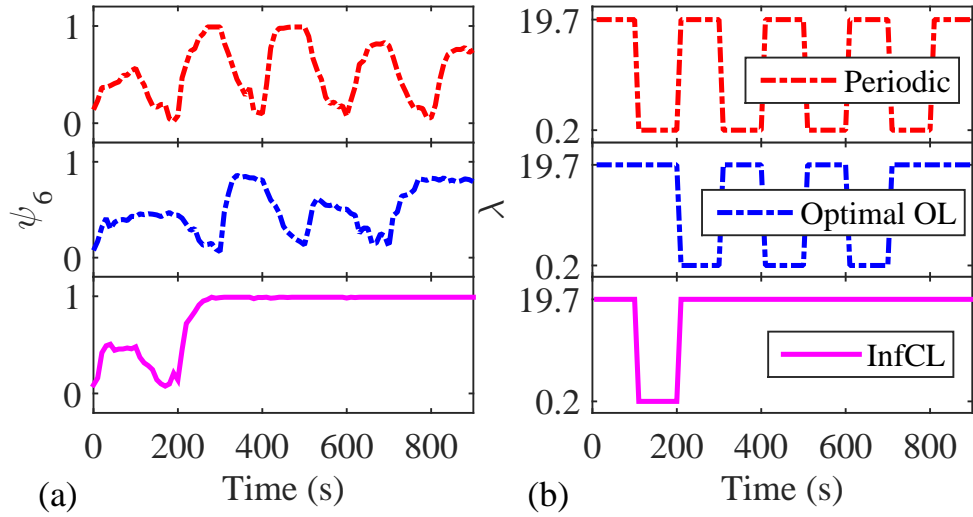


**Figure 22:** Individual experimental runs from Periodic, Optimal OL, and InfCL strategies showing the corresponding control mechanism. (a)  $\psi_6$  trajectory over time; (b) control input profile.

was not enforced. The calculation of the closed-loop strategies adds insight into the toggling concept, which can be viewed as a switching in time. However, the closed-loop policy reveals that the switching is really in space, not in time. This is seen in the static policy in Figure 17(a), but is demonstrated most convincingly in Figure 18, in which the policies do not change much in time, but maintain the same green and blue regions, with only a slight shifting of the policy seen toward the final few panels. In contrast, a truly time-varying toggling should appear in Figure 17 as an alternation of the fully blue panels for the odd time intervals and the fully green panes for the even intervals. The switching that is seen in the closed-loop optimal policies emerges from the tendency of the system to form grain boundaries under strong compression, and the efficacy of healing those grain boundaries under weak compression.

In the results presented here, feedback was an effective means to correct for unmodeled effects. However, in any model-based control strategy, the policy is only optimal for that particular model, and thus unmodeled dynamics result in sub-optimality

of the policy. Although the policies applied here were effective in achieving defect-free assembly with high yield, it would also be possible to apply robust control methods to account for uncertain parameter values [11, 16], and this might be important in other systems or operating regions. Alternatively, reinforcement learning could be applied directly to the BD simulations, initialized with the model-based policies presented here, to further refine the policy toward optimality [17]. In principle, reinforcement learning could even be applied directly to the experiments, circumventing the need to construct any model at all. However, the tradeoff would be a larger number of experiments needed, and this might not be practical due to experimental budgets.

Feedback control requires *in situ* sensing, and this has been a major limitation in applying control to self-assembly at small length scales. Optical video microscopy was implemented here to enable full state feedback of the two-dimensional assembly. Confocal microscopy could be used instead to image three-dimensional structures [32, 68]. To extend down to nanometer length scales, *in situ* transmission electron microscopy could be used, although this technology is not yet as mature [125]. However, in manufacturing practice, it may not be practical or desirable to use any of these imaging-based approaches. What this study shows is that it is really only necessary to measure the key state variables, which here are  $\psi_6$  and  $C_6$ . These sorts of overall averaged quantities could alternatively be measured by simpler non-invasive sensors such as optical spectroscopy or Bragg diffraction, which are more amenable to industrial implementation.

A time-varying voltage input is beneficial for assembling grain-boundary-free colloidal crystals, especially when combined with system state as feedback. The optimal feedback control policy was calculated using a Brownian dynamics simulation and a reduced-order Markov state model. These optimal policies were shown to be effective in assembling crystals at high yield, both in the stochastic simulations and in the experiments. The periodic and optimal open-loop policies were effective in achieving

robust assembly performance when applied to the stochastic simulations, but they did not perform as well in the experiments due to unmodeled effects. The open-loop and closed-loop policies ultimately provided similar strategies, alternating between high voltage to drive assembly and low voltage to relax out defects. Thus, a simple feedback control strategy based on endpoint detection may be an effective middle-ground for practitioners, which does not require a model-based computation of the optimal policy, but still uses feedback to confer robustness.

## CHAPTER VI

### REVISITING THE MARKOV STATE MODEL

Markov state models have been widely used to simulate time-sequential stochastic processes in many fields, given their versatility of capturing the system stochasticity. However, building a Markov state model is nontrivial. To improve the efficiency in building an accurate Markov state model, this chapter investigates the effect of state discretization, transition time  $\Delta t$ , sampling approach, and the number of samples on the accuracy of a Markov state model. The model accuracy is evaluated based on the performance of the control policy, calculated with the framework in Figure 3, in controlling a Brownian dynamics simulation to produce perfect crystals.

#### *6.1 Introduction*

Understanding the dynamics of complex time-sequential processes is important in a wide range of disciplines including physics, biology, material science, engineering, and economics. However, a comprehensive understanding of these dynamics can be elusive due to the need for a large amount of information about the system dynamics, which is challenging and sometimes even unobtainable via experiments. Therefore, having a reliable mathematical model is highly valuable.

Colloidal self-assembly processes can be simulated with Monte Carlo simulation [111], Molecular Dynamics [41, 110], and Brownian Dynamics [24, 35]. In this work, the focus is on a Brownian dynamics simulator. Based on first principle theories, Brownian dynamics quantifies the interaction forces in the system and uses particle coordinates for simulation. The resulting model has a high system dimension as demonstrated in Ref. [35]. Although these detailed force balance models can provide accurate approximations of the system dynamics, it can be time-consuming to conduct

simulations with a high-dimensional system space [104], especially for systems where the kinetics timescale spans from milliseconds to hours. Moreover, to account for the statistical effects in a stochastic process, it is even more challenging to conduct enough simulations to capture distributions. Alternatively, time-series models like the Markov state model can be built using order parameters and can shorten the amount of simulation time.

Markov state models have been widely used to simulate time-sequential stochastic processes in many fields including biology [65, 93], economics [20], as well as colloidal self-assembly processes [76, 115, 104]. A Markov state model can be formulated as either a continuous or a discrete time model. A discrete-time Markov state model is characterized by a set of discrete time points  $T$ , a set of system states  $S$ , and a probability transition matrix  $P(a)$ , which stores the transition probabilities between different states under an input  $a$  [19]. Considering the computational challenge with a continuous state Markov model, the system state is typically discretized.

The accuracy of a Markov state model requires an accurate transition matrix  $P(a)$ , which is mainly affected by the following three factors [18, 19, 74, 91]: (1) training samples, based on which the transition probabilities are calculated; (2) transition time  $\Delta t$ , after which the transitions are counted; (3) state discretization, where a continuous state space is discretized into discrete states. Although numerous studies have been reported on the construction of Markov state models, efficiently building an accurate Markov state model for a high-dimensional system is still challenging.

In this chapter, the focus remains on the  $\text{SiO}_2$  colloidal self-assembly process specified in Chapter 3, and the effects of the aforementioned three factors on the Markov state model accuracy are investigated. Optimal control policies are calculated with an infinite-horizon Markov decision process based dynamic programming optimization, as specified in the Chapter 3 of this thesis. The model accuracy is evaluated based on the performance of the Markov state model based optimal control policies, since

the ultimate application of the model is to develop control for rapid assembly of a perfect crystal. A perfect crystal is obtained when  $\psi_6$  reaches 0.95 (either during the process or at the end of the process), and the yield is the percentage of simulations that produce a perfect crystal. This definition of yield is also referred as “ednpoint detection” in Chapter 5 of this thesis. For simplicity, and to facilitate comparison to the previous chapters, two values of input  $a$  are considered in this chapter:  $\lambda = 0.2$  and  $\lambda = 19.7$ . The order parameters  $C_6$  and  $\psi_6$  are again used to represent the system dynamics in the Markov state model.

## ***6.2 Markov State Model***

### **6.2.1 Transition Time $\Delta t$**

The transition time is one important factor that affects the accuracy of a Markov state model. The validity of Markov state models builds on the Markovian assumption of a memory-free state. If the transition time is too short, it is possible that previous history also has an effect on the future dynamics [48]. This phenomenon violates the Markovian assumption that future dynamics only depends on current state instead of previous history. The memory effects can be lessened with a longer  $\Delta t$  [48, 78]. In addition, a transition time that is too short could also result in the system being artificially trapped in meta-stable states or kinetic bottlenecks, that the system would not be able to evolve to other states. This would cause absorbing states in the transition matrix. On the other hand, if the transition time is too long, it will result in a loss of intermediate information. In addition to limiting the time resolution of the model, the performance of the model-based control policy will also suffer since fewer switches in the input will be possible.

One way to identify the appropriate transition time is through trial-and-error. In this approach, modeling errors from models built with different transition times are compared, the one that gives the lowest model error is identified and the associated

transition time is selected. Model error evaluation can be achieved with system kinetics analysis-based approaches, such as mean first passage time analysis [65], or spectral theory-based lag time test, such as implied timescale test and Chapman-Kolmogorov test [19, 78].

Alternatively, if the characteristic time of a physical system is obtainable with either domain knowledge, or experimental observations, then it can be used as the transition time. In practice, the trial-and-error approach can be combined with physical interpretation to identify an appropriate transition time  $\Delta t$ . Previous findings suggest that the system in this study has a characteristic time of approximately 100 s [104]. Given the fact that assembly takes only 1000 s, longer transition times are not considered here, as they would not resolve the dynamics or enable much control action. Consequently, models with  $\Delta t = 10$  s, 50 s and 100 s are studied in this chapter.

### 6.2.2 Sampling

The Markov state model is data driven, and the accuracy of any data-driven model depends on the training samples. For a deterministic process, the challenge in building a globally accurate model comes from generating samples to cover all feasible system states, particularly for states that are rarely visited. The situation is more challenging in a stochastic process like the colloidal self-assembly system. Due to system uncertainties, multiple samples are required for each state to ensure a reliable estimation of the transition probabilities.

To generate samples, constant input trajectories or time-varying input trajectories can be used. Sampling with constant input is straightforward to implement. However it is often challenging to sample all the important states associated with all input levels, using a single input level, confined by its specific thermodynamic landscape. In addition, states that can only be reached by a dynamic input trajectory will not

be sampled with a constant input. These states can be important from the perspective of control, where switches between different inputs are specified. One challenge associated with a dynamic sampling is the design of the switching frequency. The switching time should be longer than the transition time in order to obtain a sample that can be used for the construction of the transition matrix. For this reason, a realization of simulated data with a fixed switching frequency can only be used for transition times shorter than the switching time. When the transition time is not yet determined, the switching frequency in a dynamic sampling scheme constrains the maximum transition time that can be used.

Samples can be collected from either long time simulations or short time simulations. Long time simulation trajectories include the long term behavior of the system, thus it can provide information on the characteristic time of the system. However, for systems with meta-stable states, long time simulation trajectories can be inefficient if the simulation becomes trapped [74, 86]. As a result, long time molecular or detailed dynamics simulations may require a large amount of storage space. To save storage space, intermediate information is often discarded. With short simulations, one can use constant inputs to run simulations from a predefined set of states. However, simulation with constant inputs may not capture all the important dynamically accessible states.

The main sampling pool in this study is constructed with BD simulations using time-varying input trajectories that randomly switch between the two inputs every 100 s. Specifically, a total of 500 realizations with initial states from fluid, defective and highly crystalline regions are conducted, with each realization simulated for 2000 s. The rationale behind this sampling approach is to increase the number of states visited, by exciting the system using random switches.

### 6.2.3 State Discretization

State discretization is important and nontrivial. A discretization that is too coarse could group together configurations that have different dynamics, and discretization that is too fine could result in a prohibitively large number of states to sample in transition matrix estimation [18, 19, 26, 78]. Moreover, if the system state is too big, it could also cause difficulties in control policy calculation [79], which is known as “curse of dimensionality” in dynamic programming. Therefore a tradeoff between the coarse and fine discretization is needed.

States can be discretized according to their kinetic similarities, where states with similar transition speeds are grouped together [26, 76, 91]. They can also be discretized geometrically using a distance metric. While kinetic based discretization requires a solid understanding of the system kinetics, discretization with geometrical distance metric could be easier [58].

One simple geometric discretization is to discretize the state space into evenly spaced intervals. Here we call this approach as “gridding”. Gridding is particularly useful if a region of state space is clearly defined, and the resolution of the distance metric (i.e order parameters) needed to distinguish dynamically different states is known. Another popular distance metric based discretization is clustering, which groups together states that meet a predefined criterion such as the k-means clustering. Other methods include hierarchical clustering, fuzzy clustering, and nearest neighbor clustering [19, 50, 70, 103].

Gridding requires no initial samples, and it could help the design of experiments by providing an exhaustive enumeration of the state space. If one can obtain samples for each individual cell, gridding also holds the promise for a globally accurate model. However, discretization with gridding can introduce infeasible states, and this will lead to difficulties in sampling. On the other hand, discretization with clustering algorithms is achieved using whatever samples are available, this guarantees that

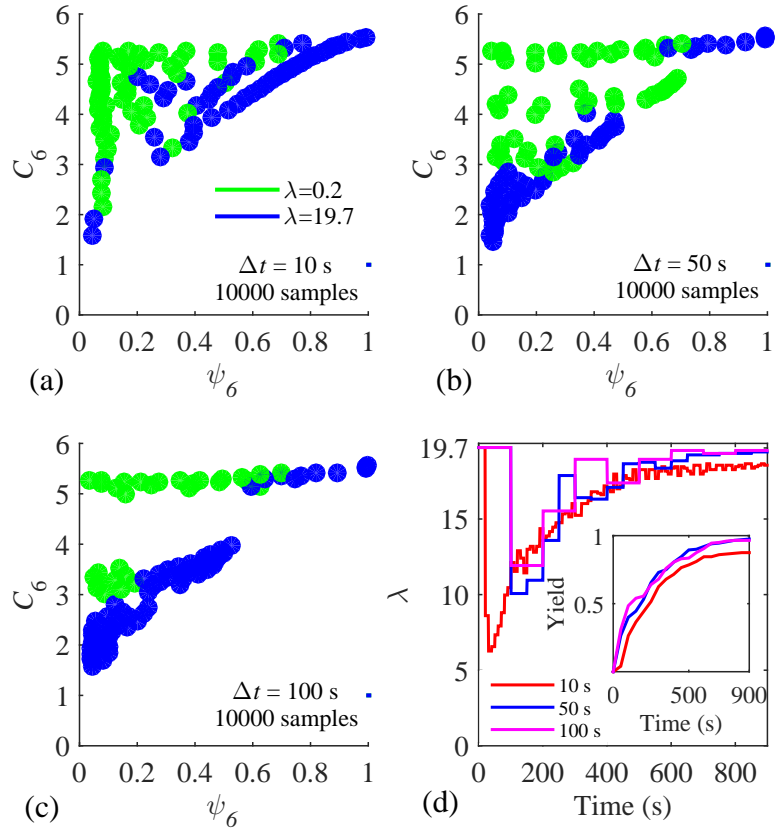


**Figure 23:** Control policies and controlled results with different transition times using 10000 samples. Control policy with (a)  $\Delta t = 10$  s; (b)  $\Delta t = 50$  s; (c)  $\Delta t = 100$  s. (d) Yield and averaged input trajectories of 200 BD realizations.

all the defined states are reachable. However, the number and the coverage of the samples affects the clustering results significantly. In this chapter, the effects of an evenly-spaced gridding and a k-means clustering approach are investigated.

## 6.3 Results

### 6.3.1 Effect of $\Delta t$

The goal of this first study is to understand the effects of different transition times with the same number of samples. Three transition times are considered:  $\Delta t = 10$  s, 50 s and 100 s. In principle, a Markov state model built with a shorter  $\Delta t$  value could

resolve more intermediate transition dynamics, compared to a model with a longer  $\Delta t$ . Ideally, the control policy generated with the shorter transition time would lead to the best performance, since more switches are possible. However, in practice the model with the shorter transition time is often less accurate, and if the model is inaccurate, the resulting control policy will also be suboptimal.

To build Markov state models for each of the three  $\Delta t$  values, 10000 samples (i.e. transition pairs) are used, taken from BD simulations generated under time-varying input trajectories. The MATLAB k-means clustering function is used to discretize the state space into 100 non-overlapping states.

As shown in Figure 23, all three control policies share the same pattern that  $\lambda = 0.2$  is used in the upper left defective region and  $\lambda = 19.7$  is used in the fluid and the highly crystalline states. As the transition time increases, more white space, corresponding to unsampled states, appears in the upper left region of the control policy. This is because the system travels a longer distance in the state space with a longer transition time, and therefore the intermediate dynamics are not captured.

The control performance of the three policies is then evaluated with 200 BD simulations and the results are summarized in Figure 23(d). All the simulations are initiated from the same initial fluid-like states with the same set of seeds in the random number generator, for each of the three policies.

The averaged input trajectories in Figure 23(d) indicate that all three policies implement the same trend; after an initial use of  $\lambda = 19.7$ ,  $\lambda = 0.2$  is used to relax the system for defect correction, and with increased crystallinity,  $\lambda = 19.7$  is used to maintain the structure. The yield trajectories indicate that policies with  $\Delta t = 100$  s and 50 s gave a similar performance with a final yield of 96.5% and 97.5% respectively. However, contrary to the expectation, the  $\Delta t = 10$  s policy gave the lowest yield of 87.5%, which is significantly different from that of the other two, according to a two-tailed t-test with a 95% confidence interval. This phenomenon indicates that, the

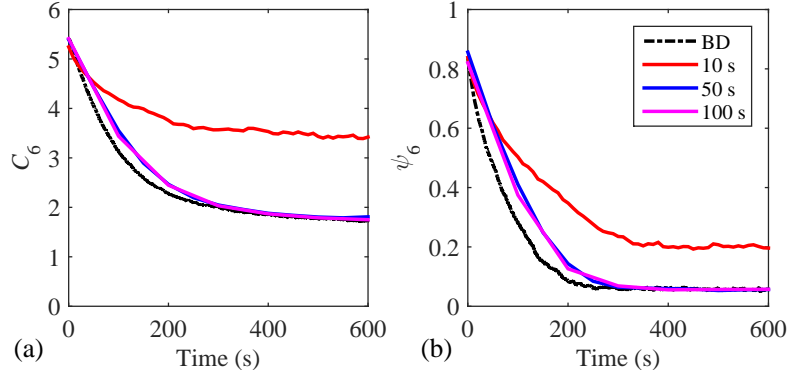


**Figure 24:** Averaged order parameter relaxation trajectories under  $\lambda = 0.2$ , starting from assembled states in BD simulation (black), Markov chain Monte Carlo simulation with model built with  $\Delta t = 10$  s (red),  $\Delta t = 50$  s (blue), and  $\Delta t = 100$  s (magenta).

**Table 5:** BD yield and assembly time of 200 realizations for policies with different  $\Delta t$  and different numbers of samples

Sample#	$\geq 50\%$ Time (s)		$\geq 80\%$ Time (s)		Yield (%)		
	$\Delta t$	50 s	100 s	50 s	100 s	50 s	100 s
100		450	300	N/A	600	72.5	89.0
500		300	300	N/A	650	78.0	90.0
1000		250	250	450	550	97.0	95.0
5000		200	150	400	450	97.5	98.5
10000		200	150	400	400	97.5	96.5

model built with  $\Delta t = 10$  s is less accurate than the other two.

A mean first passage analysis in Figure 24 confirms the above interpretation by showing that, the  $\Delta t = 10$  s Markov state model was not able to accurately quantify the relaxation from highly crystalline states, as compared to the other two models. The averaged  $C_6$  and  $\psi_6$  trajectories from the Markov chain Monte Carlo simulation with both the  $\Delta t = 50$  s and 100 s models are similar to that of the BD simulations, but the trajectories predicted with the  $\Delta t = 10$  s model differ significantly from the other three.

Further investigations into the  $\Delta t = 50$  s and 100 s models indicate that the accuracy of model built with a longer  $\Delta t$  value might be more robust to the number

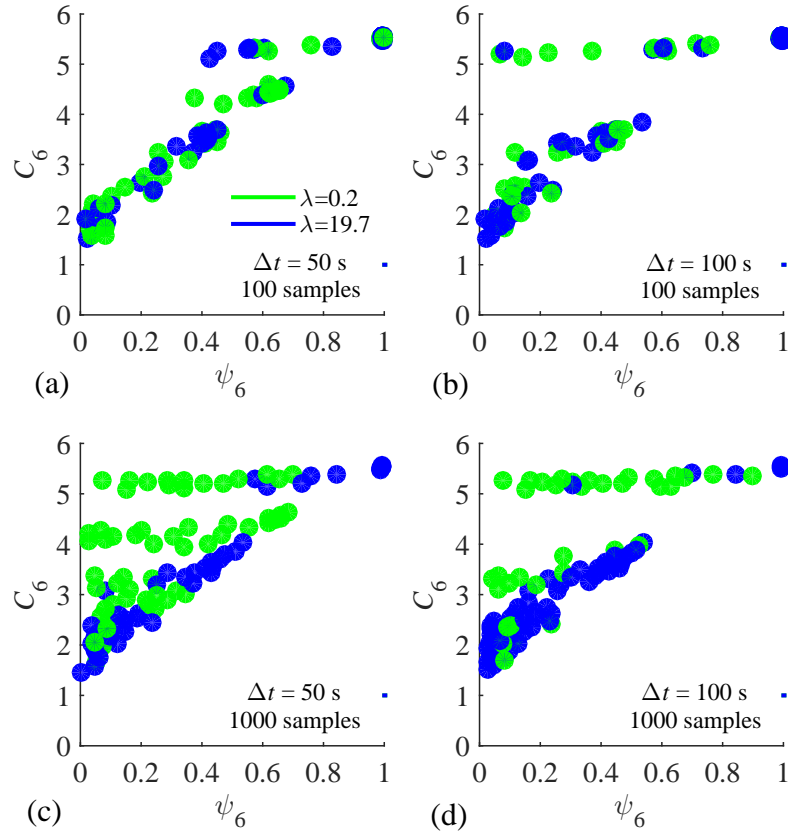


**Figure 25:** 100-state clustering-based control policies with different transition time and different number of samples. Policy for (a)  $\Delta t = 50$  s with 100 samples; (b)  $\Delta t = 100$  s with 100 samples; (c)  $\Delta t = 50$  s with 1000 samples; (d)  $\Delta t = 100$  s with 1000 samples.

of transition samples used, and a long  $\Delta t$  could potentially compensate for inadequacy in sampling.

According to Table 5, when sampling is not a limiting factor (more than 1000 samples), both  $\Delta t = 50$  s and  $\Delta t = 100$  s policies give similarly satisfying performance. Additional sampling does not show improvements in the yield, but a faster assembly to reach 50% and 80% yield is observed. When sampling is a limiting factor with 100 and 500 samples, additional samples dramatically improves the performance of the policy with 1000 and more samples for the  $\Delta t = 50$  s cases. However, less degradation was observed in the  $\Delta t = 100$  s models, as the number of samples was reduced.

Comparison of the control policies for the  $\Delta t = 50$  s and 100 s models, as shown in Figure 25, reveals that, additional sampling reduces the amount of noise in the control policy, which is resulted from under-sampling. The control policy is calculated based on the reward of using a particular action in each state. If a state is under-sampled, the reward of using either  $\lambda$  level in this state can be similar, and this is indicated as the noise in the control policy. If a state is only sampled under one input, this input is selected in the optimal control policy for that state, since the reward of using this input is higher than the other input (the state in the Markov state model for the other input is deemed as an absorbing state). Because of this, the use of  $\lambda = 0.2$  is also observed in the highly crystalline states in Figure 25(a) and (b), and this could result in destroying a perfect crystal at the end of the process. Indeed, if the yield is calculated based on the crystallinity at the end of the 900 s process, only 50% and 60% of the 200 BD simulations were able to produce a perfect crystal, with policies in Figure 25(a) and (b) respectively. However, the yield here is calculated based on the endpoint detection strategy. This further indicates that using feedback to terminate the process can improve the control performance by reducing the process time and avoiding destroying a perfect crystal.

Another observation in Figure 25 is that, when the transition time is shorter than the system characteristic time ( $\sim 100$  s) [104], the system does not move very far within the short transition time, as indicated by the white space in the upper left region of Figure 25(a). All the samples are collected from BD simulations that started from the lower left region in the state space. With a limited number of samples and a shorter than system characteristic transition time, the upper left defective states are not visited in Figure 25(a). Therefore, a transition time that is similar to the system characteristic time is suggested, and the following study focuses on  $\Delta t = 100$  s Markov state models.

### 6.3.2 Effect of Discretization

To understand the difference between the clustering and the gridding approaches, Markov state models with a transition time of 100 s are built with different numbers of samples. In the clustering approach, the state space is grouped into exactly 100 states; with the gridding approach, the system is discretized to give approximately 100 effective states. Note that an effective state is defined as a state that receives at least one sample under any input.

The clustering-based discretization is achieved by grouping states with similar order parameter values, via a k-means algorithm, and the resulting discrete states are all defined and reachable in the system. Therefore, the control policy from the clustering-based Markov state model assigns control action for every state in the system. When a new state is encountered, this state is assigned with the control action of its nearest cluster. Thus, all states have a control action defined in the control policy.

On the contrary, states discretized with gridding include reachable but not sampled states, as well as unfeasible states. If a reachable state is not sampled under either input, it is necessary to modify the control policy to define an action for these states. In this section, three modifications are considered: 1. applying  $\lambda = 0.2$  as the default action (i.e. GL); 2. applying  $\lambda = 19.7$  as the default action (i.e. GH); 3. using extrapolation and interpolation based on the neighboring states' actions to design the control action (i.e. GE).

Figure 26 shows the gridding-based control policies computed with the same Markov state model, built with the same 1000 samples used for the policy in Figure 25(d). While the control actions in the sampled states remain unchanged, actions for the unsampled states (e.g. region of  $C_6$  between 5 and 4) are subjected to the modification approaches. When the policy is modified with extrapolation and interpolation, the structure of the final control policy resembles that of the clustering-based

**Table 6:** BD yield and assembly time of 200 realizations for policies computed with gridding-based models using different policy modifications

Sample# discretization	$\geq 50\%$ Time (s)			$\geq 80\%$ Time (s)			Yield		
	GL	GH	GE	GL	GH	GE	GL	GH	GE
100	300	250	250	650	800	550	90.0%	82.0%	92.5%
500	250	150	250	550	600	550	95.0%	91.0%	95.0%
1000	150	150	150	450	450	450	94.5%	95.5%	96.5%
5000	150	150	150	450	450	450	97.0%	97.0%	97.0%
10000	150	150	150	450	450	450	97.5%	97.5%	97.5%

control policy in Figure 25(d), where the majority of the upper left region uses the low input level, and the rest is dominated by  $\lambda = 19.7$ .

Although the difference among the three gridding-based control policies is evident, the 200 controlled BD simulation realizations indicate no significant difference in terms of yield, as shown in Figure 26(d). According to the yield trajectories, all three gridding-based policies gave the similar yield. The clustering-based control policy gave a lower yield at the beginning, but reached the similar final yield at the end of the 900 s process. The histogram distribution in Figure 26(d) shows the time distribution of the yield.

A more detailed investigation with different numbers of samples confirms the similarity between the different discretization approaches. Results in Table 6 indicate that with additional sampling, both the yield and time required to reach a high yield can be improved. However, with the same number of samples, the four cases do not result in a statistically significant difference. One explanation for this phenomenon is that the majority of the important states are sampled, such that the actions used in the less important and unreachable states do not affect the performance of the control.

However, when the system is significantly under-sampled (using 100 samples), the yield of the gridding-based policy indicates a difference between the default use of  $\lambda = 19.7$  and the other modifications. One explanation is that the use of  $\lambda = 19.7$  results

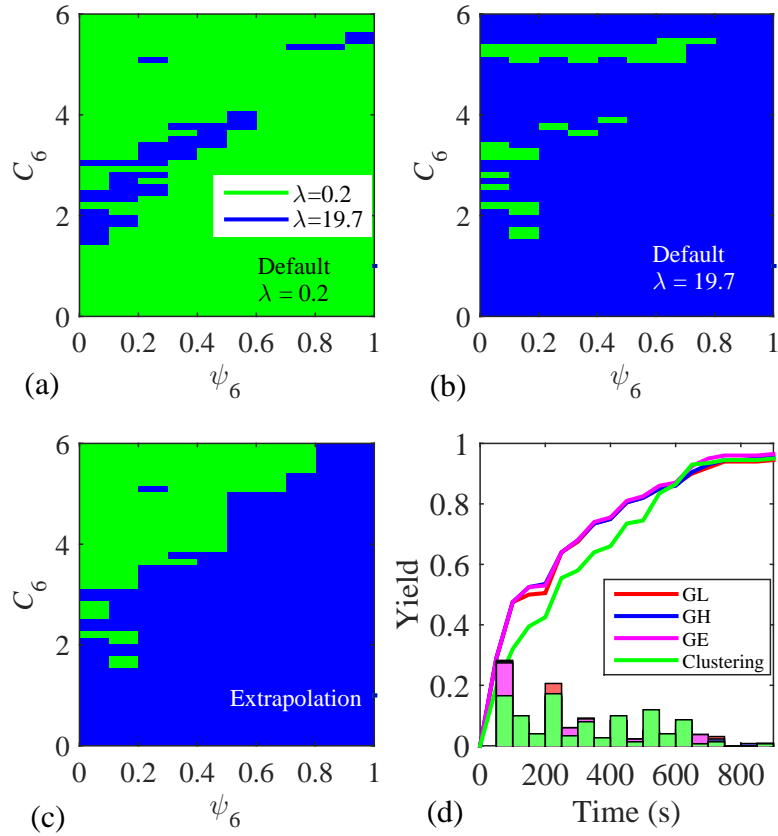


**Figure 26:** Control policies computed with gridding-based Markov state models, with policy modified to have: (a) default action as  $\lambda = 0.2$ , i.e. GL; (b) default action as  $\lambda = 19.7$ , i.e. GH; (c) modified with extrapolation and interpolation, i.e. GE. (d) Averaged yield of 200 controlled BD simulations, using control policies in Figure 4(d) and the three gridding-based policies.

in a lower chance of relaxation, due to the strong compressing force. As a results, when a defective but unsampled state is encountered, it has a lower chance of being eliminated. This further indicates the importance of using physical understanding in designing the default action.

### 6.3.3 Effect of Numbers of States

To understand the effects of different number of states, Markov state models with 100 s transition time and different number of states are studied. Since there is no

significant difference between the three policy modifications with more than 1000 samples, for simplicity, the gridding-based policies in this section are modified with a default input of  $\lambda = 19.7$ .

The state space is discretized into 10, 100, and 1000 clusters in the clustering-based policies, and is discretized to have about 10, 100, and 1000 effective states in the gridding-based policies. Markov state models are built with a set of 1000 and 10000 BD simulation samples respectively, to include the sampling effects as well. Therefore, a total of 12 Markov state models are constructed and compared.

The twelve optimal control policies, corresponding to the 12 Markov state models, are computed and evaluated with 200 realizations of 900 s BD simulations. The percentage yield of the controlled BD simulations are summarized in Table 7.

**Table 7:** BD yield of 200 realizations with policies adaptive to different numbers of states

# states discretization	1000 samples		10000 samples	
	Cluster	Gridding	Cluster	Gridding
10	97.0%	79.5%	93.5%	90.0%
100	95.0%	95.5%	96.5%	97.5%
1000	82.5%	81.5%	92.5%	86.5%

In general, policies with the clustering-based models are more robust to the number of states, compared to that of the gridding-based models, indicated by the variations among the yields.

One important observation is that, with 1000 states and 1000 samples, policies from the clustering and the gridding-based models gave a decent yield of 82.5% and 81.5% respectively. On average, only half (500) of the states are sampled under each  $\lambda$ , given that the total amount of the transition pairs is 1000. The high yield achieved here is again due to the use of the endpoint detection strategy, and the fact that random toggling lead to good assembly at some point during the process.

Surprisingly, with a coarse discretization of 10 states and 1000 samples, policies

from the clustering and the gridding-based models gave a yield of 97.0% and 79.5% respectively. This indicates that if the state space is discretized appropriately (clustering rather than gridding), the model errors introduced by a coarse discretization can be mitigated with adequate sampling (here, 50 samples per state on average).

Moreover, the results in Table 7 indicate that, in order to reach a yield of over 90%, i.e. a highly accurate model, at least an average of five samples per state are needed. Note that the averaged samples per state are calculated as the total number of samples divided by the number of states divided by the total number of  $\lambda$ 's (two).

### 6.3.4 Effect of Sample Sources

Results in the previous section indicate that a higher than 95% yield can be achieved with 1000 samples using the clustering approach with  $\Delta t = 100$  s. However, the characteristics of the samples also matter in the model accuracy. Therefore, in this section, we study the accuracy of the 100-state models built with 1000 samples from the following four sampling approaches: first, 500 samples from each of the constant input of  $\lambda = 19.7$  and  $\lambda = 0.2$ , i.e. Constant; second, 1000 samples from a toggling scheme which uniformly switches between the two input levels every 100 s, i.e. Toggling; third, 1000 samples from the controlled results using previously developed control policies, i.e. Optimal; fourth, 1000 samples generated with randomly switched input trajectories, i.e. Random. All the simulations for samples are initiated in the same fluid states.

Samples generated with the constant use of  $\lambda = 0.2$  are confined in the fluid states due to the small compressing force, while the majority of samples generated with  $\lambda = 19.7$  are from the assembled states, i.e. states with high  $C_6$  value, due to the strong compression. Therefore, two distinct sets of states are sampled under each  $\lambda$ . The unsampled fluid states in  $\lambda = 19.7$  and the unsampled high  $C_6$  states in  $\lambda = 0.2$  are deemed as absorbing states, where no transition to other states is observed

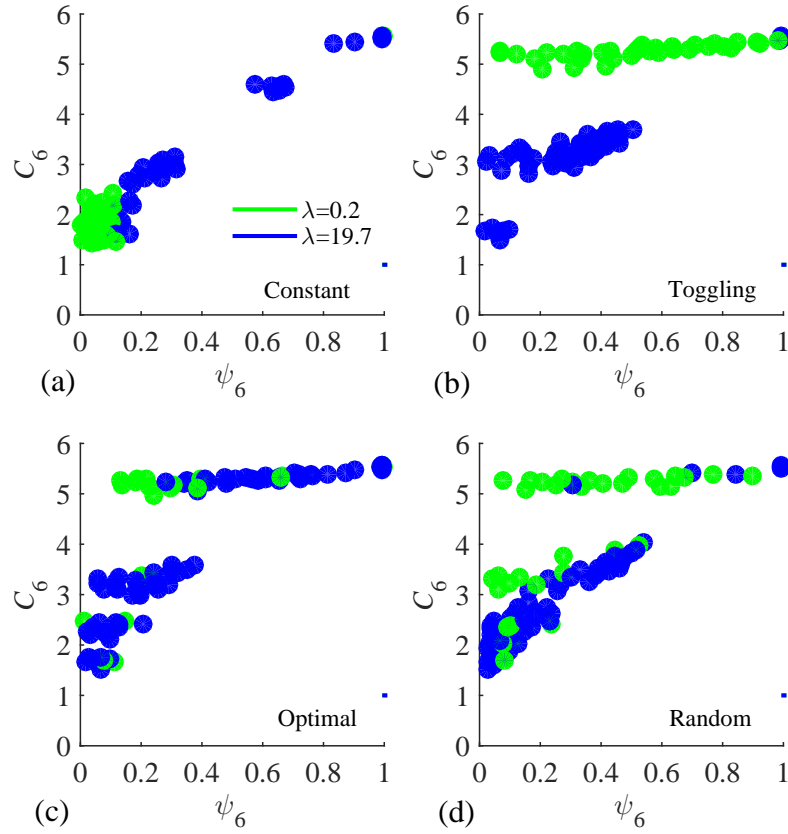


**Figure 27:** Control policies for 100-state models with 1000 samples from BD simulations under (a) constant input; (b) toggling input; (c) optimal control policy; (d) randomly switched input.

from these states, in their corresponding Markov state models. The existence of the absorbing states due to under-sampling results in the use of  $\lambda = 0.2$  in the fluid states and  $\lambda = 19.7$  in the compact states in the control policy, and this eventually leads to the lowest yield of 17.0%.

The toggling scheme starts the simulation with 100 s application of  $\lambda = 19.7$ , and switches with  $\lambda = 0.2$  every 100 s, with the last 100 s using  $\lambda = 19.7$ . This design enables sampling in the assembled states under  $\lambda = 0.2$  and sampling in the fluid and the final highly crystalline states under  $\lambda = 19.7$ . As a result, the policy uses  $\lambda = 0.2$  in the assembled states with  $\lambda = 19.7$  used in both the fluid-like and the

**Table 8:** BD yield and assembly time of 200 realizations for policies with samples generated under different input trajectories

	$\geq 50\%$ Time (s)	$\geq 80\%$ Time (s)	Yield
Constant	N/A	N/A	17.0%
Toggling	250	650	90.0%
Optimal	150	N/A	72.5%
Random	250	550	95.0%

highly crystalline state.

The control policy built with samples from the optimally controlled BD simulations in Figure 27(c) shows that, both  $\lambda = 19.7$  and  $\lambda = 0.2$  are used in the assembled as well as the fluid states. This is also observed in the policy with samples from BD simulations using randomly switched input trajectories, as shown in Figure 27(d), except that more states have used  $\lambda = 0.2$  in Figure 27(d). The use of both actions in both regions are usually desired, for reasons that some fluid states need a further relaxation to prevent a potential formation of defect; while some defective states can evolve into ordered states under  $\lambda = 19.7$ , without an immediate relaxation. However, the use of a specific  $\lambda$  in these states are particularly important; and this is why the difference in the two policies results in a different final yield of 72.5% for the policy in Figure 27(c), and 95.0% for the policy in Figure 27(d) respectively.

Another important observation in Table 8 is that, policy calculated with samples from optimal controlled simulations required the shortest amount of assembly time to reach a 50% yield, but ended up with a low yield of 72.5%. This is because the actions used on the samples are already optimized that, a further optimization leads to the fastest assembly. However, as the crystallinity increases in the controlled simulations, where the samples are collected,  $\lambda = 19.7$  is used for the remaining of the 900 s process. Therefore, the majority of samples from the later process are generated under a constant use of  $\lambda = 19.7$ . This further leads to states only being sampled under  $\lambda = 19.7$ , and they are deemed as absorbing states under  $\lambda = 0.2$ . As

a consequence, policy in Figure 27(c) shows a rapid assembly at the beginning but was not able to reach a similar final yield compared to that of the policy in Figure 27(d).

Results in Table 8 also indicate a similar performance between the policies built with samples from the toggling scheme and the randomly switched input trajectories, in terms of both assembly time and the final yield. The high yield with the policy using toggling samples confirms our previous understanding that, the defect correction mechanism is essentially relaxation and reassembly. However, samples generated with randomly switched input trajectories include richer dynamics than that of the toggling scheme, therefore the policy with randomly switched samples gave the best performance among all the cases.

#### **6.4 Discussion**

A globally accurate model is valuable, but for systems with a large amount of rarely visited, or dynamically unimportant states, it would make more sense to focus on the more relevant states. For these systems, sampling schemes that focus more on the states of interest could potentially accelerate the estimation process, as well as providing a useful model. One such approach is adaptive sampling [94], where initial sampling is generated using available states as starting points. Based on the weighting of the clustered states on the model uncertainty, a weighted sampling starting with the updated states are conducted for additional samples. This process is repeated until a satisfying model is achieved. The biased sampling algorithm could be particularly beneficial when conducting a global sampling is costly.

To design a control policy, it is important for each input to cover a common state space, in order to enable a reliable switch between different inputs. However this can be challenging, especially when system dynamics are dramatically different under different inputs. Instead of modifying the calculated policies, one can use estimation

techniques, such as interpolation or extrapolation, to estimate the transition probabilities in the unsampled states, before used in policy calculation. The underlying assumption is that, dynamics for the neighboring states do not differ significantly. With such a modified transition matrix, one can avoid defining a default action in the control policies for unsampled states with the gridding-based discretization.

Another observation from this study is that, to achieve the same amount of effective states, gridding defined a large total number of states. The total number of states are 20, 500, and 12000 for the 10-, 100-, and 1000-effective state models built with gridding in Section 6.3.3 respectively. These extra states make it more challenging to build an accurate model, considering the amount of additional sampling needed. It is also challenging to modify the control policy to deal with unsampled states. One alternative is to discretize the states unevenly to group together the infeasible and less important states. However, to find an appropriate uneven discretization can still be nontrivial. Clustering may be a better and simpler approach, compared to gridding.

## **6.5 Conclusion**

The results demonstrate the effect of state discretization, transition time  $\Delta t$ , sampling approach, and the number of samples on the accuracy of a Markov state model. Optimal control policies are computed with dynamic programming based on the reduced-order Markov state model. The model accuracy is evaluated based on the performance of the control policy in controlling a Brownian dynamics simulation for perfect crystals.

According to the results, in order to efficiently build an accurate Markov state model, the following settings are suggested: (1) a transition time that is similar to the system characteristic time, (2) a dynamic sampling approach, such as the time-varying input trajectory, (3) a clustering algorithm based on the metric distance for state space discretization, and (4) a discretization that ensures on average, at least

five samples per state, to balance the number of states and the number of samples.

The conclusion can also be made that, with the Markov state model based optimal control policy, rapid assembly of a highly crystalline two-dimensional colloidal crystal can be achieved. With the dynamic sampling approach and the clustering discretization, a 97% yield of the perfect crystal is achieved, even if the state space is coarsely discretized into 10 states. The study of this chapter can be extended to other systems that can be approximated with Markov state models.

## CHAPTER VII

### CONCLUSION AND OUTLOOK

#### *7.1 Conclusion*

This thesis illustrated the formulation and application of the optimization framework proposed in Figure 3, to compute an optimal control policy for a colloidal self-assembly process. A tunable AC electric field is used as a global actuator to control the particle movement. Order parameters, selected based on domain knowledge, are used to reduce the system dimension and quantify the ordering of the structure. Actuator-parameterized Markov state models with time-invariant transition matrices are built using samples from a Brownian dynamics simulation. Dynamic programming is used to solve for both the time-varying and time-independent optimal control policies. Feedback is enabled by conducting real-time microscopy to track individual particle locations for the order parameter calculations, and is integrated in the policy lookup table to update the control action for the next time step.

The control policy breaks meta-stable states and kinetic bottlenecks in the assembly process, by switching between different input  $\lambda$ 's. This out-of-equilibrium assembly strategy reduces the amount of time spent in the defective states, which would otherwise not be eliminated with a near-equilibrium approach in a similar amount of time. The near 100% yield of defect-free two-dimensional crystals in the experiment with the optimal control policy proves the feasibility of using the model-based feedback control to robustly control the stochastic colloidal self-assembly process.

The comparison between different control strategies in Chapter 5 indicates that, besides the optimal control policies, simple time-varying control, such as the “toggling” strategy, can also improve the yield compared to that of a time constant control

strategy. This phenomenon reveals that the defect-correction comes from suppressing the strong compression force for particle rearrangement. The performance of the time-based “toggling” approach depends on the selection of the switching frequency. A switching frequency that is too slow is essentially the same as restarting the assembly process, while switching too fast could not provide long enough time for particle rearrangement. Thus a tradeoff exists between the fast and slow switching frequency, and with a switching time near to the system characteristic time, a satisfying performance can be achieved.

The optimal open-loop control policy built on the Markov state model, presented in Chapter 5, features the switch between the high and the low  $\lambda$ 's, which is same as the toggling strategy. However, it uses more high input levels towards the end of process to reduce the chance of destroying assembled highly crystalline crystals, which could instead happen in the toggling strategy. As indicated in the single experimental results in Chapter 5, an assembled perfect structure might not form a highly crystalline state once destroyed. Therefore, the model-based optimal open-loop policy could potentially lead to a possible improvement compared to the toggling strategy.

Colloidal self-assembly processes are stochastic, the dynamics evolved from the same state is different every time the process is initialized. Open-loop control strategies update control actions only depend on time, regardless of the system state. Without feedback, open-loop control might result in undesired relaxation in a highly ordered state and undesired compression in a defective state. On the contrary, feedback control updates control actions based on the system state, thus overcoming the aforementioned issues to improve the robustness of the performance from system uncertainties. Moreover, a time-dependent optimal control policy updates control actions based on both time and system state, this could theoretically further improve the performance of the control by adding an extra degree of freedom.

Results in Chapter 6 reveal several important factors in building an accurate

low-dimensional Markov state model. First, dynamic input trajectories that switch between different input levels, can more efficiently generate samples to cover a richer dynamics, compared to a constant input trajectory; second, model built with a transition time similar to the system characteristic time is more robust to the number of samples, compared to that of a shorter transition time; third, discretizing the state space with a clustering algorithm, based on the metric distance, can avoid the policy modification in the gridding approach for unsampled states; fourth, a balance the number of states and the number of samples is important when sampling is limited. To ensure the model accuracy, an averaged of at least five samples per state are suggested.

In summary, this thesis has demonstrated the implementation of a Markov decision process based dynamic programming framework on a colloidal self-assembly process for rapid production of perfect crystals. Several open-loop and closed-loop control policies are investigated to illustrate the mechanism of defect correction. The analysis of Markov state model accuracy is also presented. The framework in this study is built on first-principle concepts that can be generalized to any molecular, nano-, or micro-scale assembly process where, there is a global actuator to control the dynamics and a modeling of the relation between the actuator and the system dynamics. The capability of system state measurement as feedback is desirable but not required, since a quality optimal open-loop control policy can also be calculated with the proposed framework.

## **7.2 Outlook**

The proposed framework in this thesis provides a viable approach to rapidly eliminate defects, which is one of the biggest challenges in colloidal self-assembly. It opens up new opportunities in a wide range of domains, and the application of the framework has already been demonstrated in other systems such as the crystallization of

$\text{Na}_3\text{SO}_4\text{NO}_3\cdot\text{H}_2\text{O}$  in a batch system [42, 43]. However, there are still open issues need to be further explored.

### 7.2.1 Control Input Selection

The use of dynamic programming is subjected to “curse of dimensionality”. To deal with this, discrete input levels are used in the framework. The selection of the discrete input levels is important and nontrivial to the performance of the control.

Starting with a pool of candidate input levels identified with heuristic experience, the four input levels in this study are selected via trial-and-error, based on their free energy landscape analysis. The free energy landscape reveals the equilibrium property of the system in the order parameter space, and indicates the equilibrium configuration of the system at that particular input level. The high input level is used to ensure the reachability of the perfect structure, and the low input level is used for a rapid relaxation to eliminate defects. Intermediate levels are included to partially relax the assembly while maintaining the ordered structure. The thermodynamic properties under the intermediate input levels should be significantly different from each other to avoid redundancy. Theoretically, more input levels should lead to better control policies, given the increased freedom with additional actions. The two upper limit input levels can be defined as the two physical limits of a global actuator. However, the selection of the number and the magnitude of the intermediate levels is more challenging.

Besides the above free energy landscape analysis based approach, the discrete input levels can also be defined with information from optimized input trajectories with a continuous input domain, from a simpler yet similar system. One example is the model predictive controlled results illustrated in Appendix A of this thesis. The optimized input trajectories can indicate the most often used input levels in the control. Starting with these input levels, one can more efficiently define the discrete

set of the input levels. However, this approach might require additional efforts in constructing models and solving for the optimal control input.

### 7.2.2 System State Measurement and Representation

*In situ* measurement of system states is required in a feedback control, and rather than it is also required in understanding and verifying a model. However, self-assembly systems at nano- and micro-scales are always subjected to the capability of state measurement and representation, due to the lack of sensing and the high system dimension. This is especially challenging in a large system for three-dimensional structure production.

By virtue of the particle size, optical video microscopy is used in our system to monitor individual particle location. When a larger quantity of smaller sized particles are used for three-dimensional crystals, the capability of measuring the system state and the imaging processing time are all critical in practical applications. For these systems, other *in situ* measurement techniques should be explored. For example, scanning electron microscope (SEM) for two-dimensional optically invisible structures and transmission electron microscope (TEM) for three-dimensional structures. Recent developments in liquid-cell electron microscopy has enabled the imaging process of in-solution structures, and overcomes the difficulties encountered in liquid measurements using TEM [87]. A recent application of liquid-cell microscopy in monitoring the one-dimensional solution-phase CdSe/Cds self-assembly dynamics demonstrates the potential of using this technique for in-solution measurements with nano-meter resolution [100]. To broaden the proposed framework in this thesis, the system measurement techniques should be further explored.

Another aspect for future work is the exploration of the order parameters. Representing a high-dimensional system in a lower and physically meaningful space can significantly help explain the dynamics and design the controller. The two order

parameters used in this thesis capture the formation of grain boundaries, however, previous findings indicate that they can not always distinguish a state with a single point vacancy. The two order parameters are calculated as averages over all the particles, instead, the distribution of individual particle order parameters can be used. Besides, other dimensionality reduction approaches including spatial statistics [56], dynamic PCA [63], and diffusion mapping [116], should also be further explored for a more efficient identification of physically meaningful order parameters.

### 7.2.3 Combination with Other Systems

The self-assembly process considered in this study is composed of spherical particles in a radially inhomogeneous electric field. Variations of the system settings including particle shape and electric field geometry can lead to a broader application. For example, changes on the particle shape can introduce different geometric structures in the assembly; the location and the number of the electrodes can change the geometry of the electric field for a more complex control.

A combination with other manufacturing methods should also be explored. For example, the capability of manipulating individual particles via acoustic tweezers [108, 126] enables the possibility of correcting defects locally. The combination of a global driving force via an electric or magnetic field for a holistic control and a local defect correction mechanism, like the acoustic tweezers, could potentially provide more effective control over the system. Such a combination can also be extended to template-guided assembly in an external field mediated system as in Ref. [66]. In these systems, the global driving force might instead be the templates which define the bigger structure of the crystal, while the electric field, or other externally applied fields function as correction forces for better crystallinity.

Furthermore, coupling coated particles, like Janus particle and DNA coated particles, with externally applied fields could also provide a promising route for rapid

assembly of highly ordered structures. The assembly dynamics in these systems are controlled by both the inter-particle reactions determined by the particle surface properties, and the particle-field interactions manipulated by the external force field. As in Ref. [71], the assembly is a combined result of both the particle surface property and the global driving force (temperature). Assembly of coated particles is usually enabled when particles come in contact with each other, and the highly crystalline state is usually achieved at equilibrium state. If combined with externally applied fields to provide a global driving force to rapidly drive the particles in contact with each other, the assembly process could potentially be accelerated.

#### **7.2.4 Optimal Policy Design**

Dynamic programming avoids the demanding online computation by employing an offline calculation scheme. However, when the number of state and inputs increase, even computed offline, the computational demand can be unmanageable. One alternative to dynamic programming is the approximate dynamic programming, which instead of an optimal policy, solves the optimization with approximated value functions to conduct the Bellman optimality iteration [79]. Approximate dynamic programming has been mainly studied in artificial intelligence and communications, however, it remains largely unexplored in the application of colloidal self-assembly control.

Another direction to explore could be the combination of model predictive control and the dynamic programming to take care of both computational issue and the system stochasticity, as in Ref. [83].

The performance of any model-based control depends on the quality of the model. When it is challenging to obtain an accurate model, model-free techniques such as reinforcement learning can be used instead. Reinforcement learning is similar to the idea of dynamic programming that it evaluates and stores the reward or cost associated with different actions for each state, and selects the best combination of

actions according to a predefined criterion/objective function. This algorithm requires the system to visit each state many enough times to perform a statistically evaluation of each control action before converging to a final optimal policy. However, visiting each state for many enough times is usually costly and even inaccessible for a practical application. One way to mitigate this challenge is to start with a heuristic policy or an optimal policy from a similar system.

### 7.2.5 Extension to Continuous Systems

This thesis has focused on optimal control in a batch system. However, before colloidal self-assembly can be used for mass production, an understanding of the dynamics and control in a continuous system is required.

One possible construction of a continuous system can be the roll-to-roll production used in printing, similar to a plug flow reactor shown in Figure 28. The dispersed particles are continuously added and the assembled structure is continuously removed at a velocity of  $V$  with a unit of “length/time”. This system will enable both an open-loop and a closed-loop control, with either online and off-line calculation. For the open-loop control, the control policy is designed ahead without the instant system state as feedback, only the state at the outlet will be considered in the objective function. While in the closed-loop control design, the system state is measured at point  $a$  which is  $\Delta L$  away from point  $b$ , and the updated control action based on feedback is applied at point  $b$ . The distance  $\Delta L$  is defined as  $V \times \Delta t$ , where  $\Delta t$  is the time needed to obtain the system state information and the control policy.

However, the design of the assembly driving force, the simulation of the system dynamics, the measurement of the system state, and the maintenance of the assembled structure might all differ from that of a batch system, and can be more challenging. Other challenges also need to be addressed for experimental manufacturing. First, the possible block in the channel caused by the crystal growth makes it nontrivial

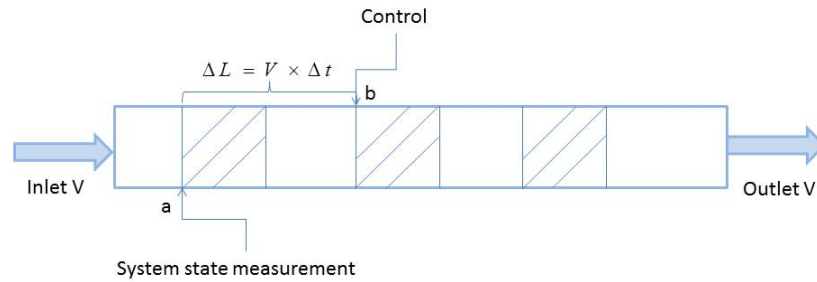


**Figure 28:** Continuous flow system for colloidal self-assembly in the format of a plug flow reactor.  $V$  is the velocity with unit *length/time* and  $\Delta t$  is the time needed for state measurement and control action calculation.

to make a device for such a continuous system. To address this issue, potential approaches include the design of reactor structures, the choice of materials, and the design of the flow patterns. Second, to experimentally implement the control policy, the computational time to develop the control policy and to obtain a feedback is confined in a practical time interval. Third, the possible noise in the measurement and the delay of the actuator will also add to the complexity of experimentally controlling a continuous process.

Controlling self-assembly of nano- and micro-scale colloidal particles is a promising yet challenging route of manufacturing new materials with novel properties. The use of colloidal self-assembly for a continuous mass production of three-dimensional structures with low defect density, still remains largely unexplored, and requires further studies.

## APPENDIX A

### COLLOIDAL SELF-ASSEMBLY WITH MODEL PREDICTIVE CONTROL

Besides the proposed framework, I also investigated the application of model predictive control on the colloidal self-assembly system [105]. In this chapter, a Model Predictive Control (MPC) method is proposed to facilitate self-assembly of a quadrupole colloidal system for defect-free two-dimensional crystals. A Langevin equation model is developed to model the thermodynamics of the colloidal system and provides predictions for optimization. A finite prediction horizon is used to optimize the input trajectory over different control horizons. The stochastic optimization problem is solved using simulated annealing, and simulation results of the optimized input trajectory demonstrate that the MPC algorithm proposed in this section is able to accelerate the process of crystallization of the quadrupole colloidal system.

#### *A.1 Introduction*

Based on the operating principles and other properties, predictive control technology can be divided into different categories, among which model predictive control has been widely studied and applied because of its particular merits over other predictive control technologies. There are three main advantages of MPC technology as summarized by Qin and Badgwell [80]: (1) the incorporation of an explicit model into the control calculation allows the controller to deal directly with all significant features of the process dynamics; (2) the consideration of process behavior over a future horizon makes it possible to account for disturbances, which ensures that the process moves more closely to the desired state; (3) the ease of adding various constraints on input,

state and output leads to tighter control at the optimal constrained steady-state for the process. This third feature distinguishes MPC from other control methodologies [80]. Decades of research has revealed the promising future of MPC in various industrial applications spanning from industrial plant design to chemical production. A summary of different applications can be found in Ref. [80].

Considering the success of MPC in industrial applications [1, 27, 72, 80], we implement MPC in our simulated quadrupole colloidal system, aiming to produce a defect-free two-dimensional hexagonal SiO<sub>2</sub> crystal. In this Appendix, we present the application of MPC to a colloidal assembly system with a nonlinear stochastic Langevin equation as our dynamic model. The purpose of this paper is to introduce a control method with real-time feedback to reliably manipulate the formation of colloidal crystals on a micro scale in a quadrupole system, by using an external electric force. The specific experimental system being modeled, the theory of our control strategy, and the analysis of the control results are described in detail in the following sections.

## ***A.2 Problem Statement***

In order to study the self-assembly mechanism of colloidal particles, we consider a colloidal system of SiO<sub>2</sub> particles developed by Michael A. Bevan's research group at Johns Hopkins University [54]. In this system, 174 identical SiO<sub>2</sub> particles with a nominal size of 1.5  $\mu\text{m}$  are suspended in deionized water in a container made of glass microscope cover slips (50 mm x 24 mm x 150  $\mu\text{m}$ ) [54]. Four separate, tunable 1 MHz AC electrode tips are attached to the edge of the container and are connected in series with a function generator to generate an electric field inside the container [54]. We simulated this system with a Brownian Dynamics (BD) simulation where the particle-particle, and particle-field interaction forces are considered [53]. Previous results have demonstrated that the particle movements can be manipulated by applying

different magnitudes of voltages to the system [54]. Based on this observation, we want to design an optimal input trajectory of the voltage to efficiently manipulate the assembly of the SiO<sub>2</sub> particles into defect-free two-dimensional hexagonal crystals, optimizing speed and accuracy. Unlike most of the previous research, in our case, the current crystal information is considered as feedback and is utilized to further optimize the control policy for subsequent moves.

### ***A.3 Theory and Method***

#### **A.3.1 Dynamic Model–Langevin Equation**

Developed in 1908 by French physicist Paul Langevin (1872-1946), the Langevin equation is a stochastic equation that provides a simple but still accurate way to describe the Brownian motion of the characteristic parameter of a system [62]. The simplicity and accuracy of the Langevin equation in describing Brownian motion has earned tremendous attention in mathematics, physics, and engineering.

In our colloidal system, we used the Langevin equation as a model to simulate the colloidal assembly process to capture the dynamics of the order parameters identified for our particular system [54].

Developed from the Fokker-Plank equation [9], the Langevin equation for our system is given as the following:

$$\frac{dx}{dt} = D_1(x, u) + \sqrt{D_2(x, u)}w(t) \quad (44)$$

where  $x$  is the state of the system, and in our colloidal system  $x = C_6 \in (0, 6)$  is the order parameter defined as the average number of hexagonally close packed particles around each particle [54].  $u$  is the input control parameter,  $D_1(x, u)$  is the drift function,  $D_2(x, u)$  is the diffusion landscape, and  $w \sim N(0, 1)$  is an independent identically distributed Gaussian white noise term with zero mean and unit variance.

The Free Energy Landscapes (FELs), which describes the change of free energy as a function of system configuration under a fixed thermodynamic condition, is chosen

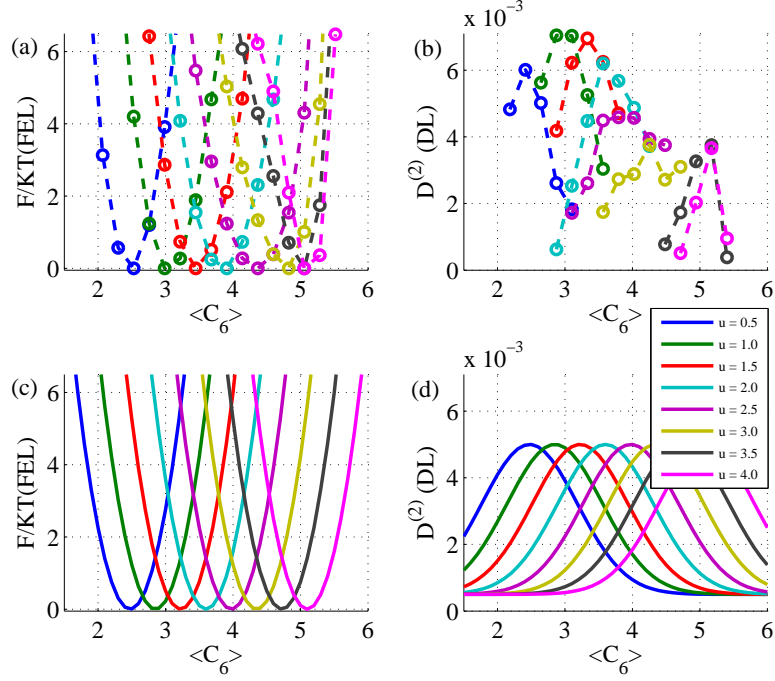


**Figure 29:** (a) FELs calculated via BI method based on BD simulation, (b) DLs calculated via BI method based on BD simulation, (c) FELs from simplified analytical model, (d) DLs from simplified analytical model.

here as a modeling method to capture the state of our colloidal assembly system. The justification of the use of FEL in our Langevin model lies in the fact that the system is time-invariant [96, 97].

The corresponding discrete-time Langevin equation with a sampling interval of  $\Delta t$  is given as:

$$x_{k+1} = x_k + \Delta t D_1(x_k, u_k) + \sqrt{2D_2(x_k, u_k)\Delta t} w(t) \quad (45)$$

where the subscript  $k$  is a discrete time index. FELs can be expressed in analytic form according to [61, 117],

$$F(x, u) = KT \int \frac{\frac{dD_2(x, u)}{dx} - D_1(x, u)}{D_2(x, u)} dx \quad (46)$$

where  $K = 1.38066 \times 10^{-23} J/K$  is the Boltzmann constant, and  $T = 293K$  is the temperature given in Kelvin.

In previous work, the effective actuator, and the effective configuration state which can be experimentally measured, have been identified to be field voltage  $V_{pp}$  and  $C_6$ , respectively [53, 54]. Thus the BD simulation has been implemented under different values of  $u$ , which has a one-to-one relationship with the field voltage  $V_{pp}$  [53] (note  $u$  here corresponds to  $\lambda$  in [53]). Under each value of  $u$ , 300000 time steps were simulated, with the time step being 1 ms. The  $C_6$  value has been calculated and recorded at each time step. The set of all possible  $u$  values is chosen to be  $u \in [0.5, 4.0]$  where a step size of 0.5 for  $u$  is used empirically so that the trajectories of  $C_6$  under different voltage levels are distinguishable yet not too different so that useful information is obtained. The Bayesian inference (BI) method [10, 49, 98] is then applied to the recorded  $C_6$  trajectories, resulting in diffusion landscapes (DLs) and FELs as shown in Figure 29.

Inspired by the numerical DLs and FELs from BD simulation, we developed the simplified analytic expression of FELs and DLs:

$$F(x_k, u_k) = 10KT (x_k - 2.1 - 0.75u_k)^2 \quad (47)$$

$$D_2(x_k, u_k) = 4.5 \times 10^{-3} e^{-(x_k - 2.1 - 0.75u_k)^2} + 0.5 \times 10^{-3} \quad (48)$$

where the state  $x$  denotes  $C_6$  and  $u$  is the controller/actuator, such that the resulting DLs and FELs curves, shown in Figure 29 (c) and (d), are similar to the numerical simulations from BD. We call the system characterized by FELs and DLs in Eqn. 47 and Eqn. 48 the simplified colloidal assembly system.

According to the development of FELs in both Figure 29 (a) and (c), and referring to the calculation of transition probability between two states along the energy curve as in Ref. [3], it can be seen that given any constant control value, the probability for either system to transit from any value of  $x$  to another is positive. Thus, given long enough time, it is possible for either system to visit the whole state space from any initial state, i.e. the system is ergodic. Moreover, both sets of FELs show that

a higher  $u$  corresponds to a higher  $x$  at the energy minimum. As was discovered in previous work, for the quadrupole system, a higher  $x$  ( $C_6$ ) corresponds to higher crystallization [53]. Thus the highest possible  $x$  is desirable.

Next we adopt the Langevin model, Eqn. 45, to represent the dynamics of the order parameter  $x$  of this simplified system. Combining Eqn. 45 and Eqn. 46 gives the modified Langevin model as:

$$x_{k+1} = x_k + \left( \frac{D_2(x_k, u_k)}{dx} - \frac{dF(x_k, u_k)}{dx} \frac{D_2(x_k, u_k)}{KT} \right) \Delta t + \sqrt{2D_2(x_k, u_k)\Delta t} w_k \quad (49)$$

### A.3.2 Objective Function–Cost Function

Model predictive control falls into the category of optimal control, where the control action is obtained by online computation. The basic concept of MPC is to use a dynamic model to forecast system behavior over a prediction horizon, and optimize the forecast to produce the best control move over the control horizon [81]. In MPC, an optimized input trajectory is designed at each control interval based on the current system state and the prediction from the model, subject to the constraints of the system. However, only the first control input is applied to the system at the next time step. This strategy ensures that the latest update of the actual measured output is considered in the optimization and accounts for the disturbance introduced by any uncertainties in the system [80, 81].

A function  $J$  is defined according to the objective of the optimization. Therefore it is called the objective function (sometimes named as the cost function if it is to be minimized) [81].

For our discrete-time simulation system, we define the cost function as:

$$J(x, u) = \sum_{k=1}^N J_k(x(k), u(k)) \quad (50)$$

where,  $J(x, u)$  denotes the cost function to be minimized and is a function of both the state of the system and the manipulated parameter.  $J_k(x(k), u(k))$  is defined as

the cost at each time point  $k$  as following:

$$J_k(x(k), u(k)) = (x(k) - x_{target})^2 \quad (51)$$

where  $x = C_6 \in (0, 6)$  is the order parameter defined as the average number of hexagonally close packed particles around each particle [54].  $x_{target} = C_{6target} = 6$  indicates a perfect hexagonal crystal in a two-dimensional case, and this is the desired state of our system. The optimal control is defined in a way such that  $J(x, u)$  is minimized subject to the physical constraints of both  $x$  and  $u$ :

$$\min_u J(x, u) \quad (52)$$

In our study,  $N$  is chosen as an integer to denote a finite control horizon.

### A.3.3 Optimization–MATLAB Optimizer

In order to solve the optimization, different MATLAB optimization solvers were investigated using MATLAB R2011a. However, considering the stochastic property of this system, only non-gradient based methods were considered, including direct search (*patternsearch*), simplex search methods (*fminsearchbnd*), and simulated annealing. Results from all these optimization solvers were analyzed according to their stability, convergence and ease of use. We chose simulated annealing for two reasons: (1) it is reliable when dealing with our nonlinear, stochastic Langevin model; (2) it provides more convenience to modify the internal arguments of the solver compare to the other investigated solvers.

## A.4 *Result and Discussion*

The MPC controller is implemented in the Langevin equation to perform an online optimization, using the simulation from our Langevin equation model.

To demonstrate the effects of the external electric force on our colloidal system, 100-realization-averaged  $C_6$  trajectories from a system under different voltage magnitudes without feedback control are recorded and compared. In this test, the input

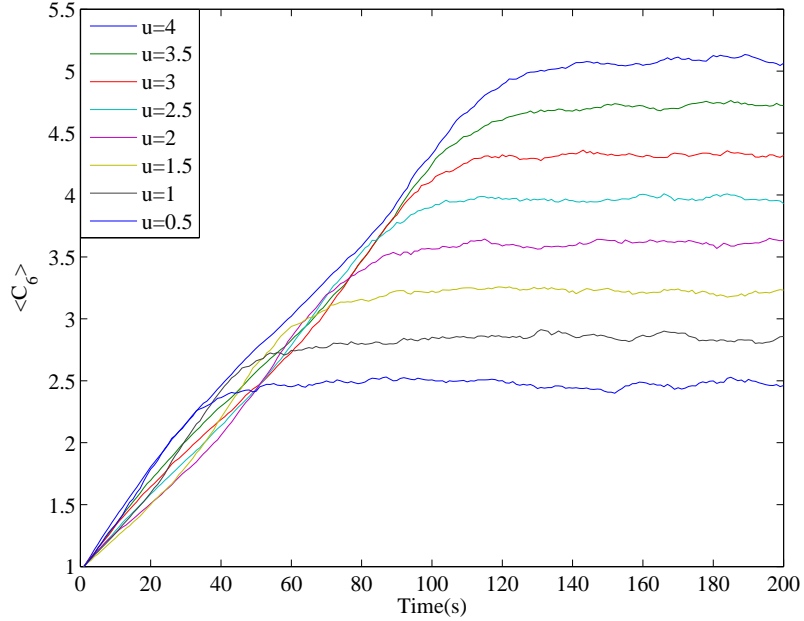


**Figure 30:** Averaged  $C_6$  trajectories over 100 realizations for different constant input  $u$  from system without a feedback control policy.

parameter  $u$ , which is the parameter corresponding to the actual experimental voltage, is set as a constant value throughout a 200-second simulation process. The input is discretized into 8 evenly spaced intervals between 0 and 4 with an increment of 0.5. The  $C_6$  trajectories of all these 8 input values are compared. The results are shown in Figure 30.

From Figure 30, we observe that as the input  $u$  increases, the steady state of  $C_6$  goes higher and higher which matches our theoretic expectation from Figure 28 that, with a stronger applied electric force, the particles are pushed closer to each other and thus achieve a higher  $C_6$  value eventually. However, for intermediate values of  $u$ , the slope in  $C_6$  decreases, which means an intermediate input leads to slower crystallization in our colloidal system. Also, in Figure 30, we can conclude that the  $C_6$  trajectories never reach the state of  $C_6 = 6$ , which is defined as the ideal hexagonal crystal in our colloidal system. This phenomenon is due to the edge effects of the system since particles at the edge of the system will never have six neighbors.

Comparison of the average cost from both the controlled and uncontrolled system reveals that the MPC optimization policy is able to accelerate the self-assembly process and maintain the system at the desired state.

In these tests, we chose a prediction horizon ( $N_p$ ) equal to the length of the control horizon ( $N_c$ ). Different  $N_c$  values were tested aiming to identify a suitable control horizon according to their effectiveness. For each  $N_c$ , the horizon is divided into evenly spaced control intervals. The corresponding number of intervals is denoted as  $s$ . The length of each control interval is denoted as  $h$  with a unit of second, which is also the time between each input adjustment. The relationship between  $N_c$ ,  $s$  and  $h$  is given as:

$$N_c = s \times h \quad (53)$$

According to this scheme, different combinations of  $s$  and  $h$  for different control horizons were tested. The tested number of control intervals,  $s$ , includes 2, 3, 5, 7, 8, 10, 12 with the lengths of control interval,  $h$ , of 1, 2, 4, 5, 10, 20 and 40 for each  $s$ . Again, the optimization is based on the expectation value,  $C_6$ , over 20 independent realizations.  $C_6$  trajectories from each of these  $s$  values that give the lowest average cost are denoted as the best  $C_6$  trajectories and are compared with the uncontrolled  $C_6$  trajectory, with input  $u$  set to be four constantly throughout the whole process. The result is shown in Figure 31.

In Figure 31,  $s2 - h4$  indicates the combination of  $s = 2$  and  $h = 4$ . This comparison reveals an obvious advantage of the controlled  $C_6$  trajectory over the uncontrolled trajectory in the sense that the  $C_6$  in the controlled system reaches its highest value about 40% faster than the uncontrolled system. The state of  $C_6$  is also well maintained after it reaches its steady state. These observations indicate that the controller is able to accelerate the formation of a highly ordered crystal faster than the uncontrolled system and maintain the formation of the crystal. In addition, from Figure 31, the difference between each best  $C_6$  trajectory from the controlled system

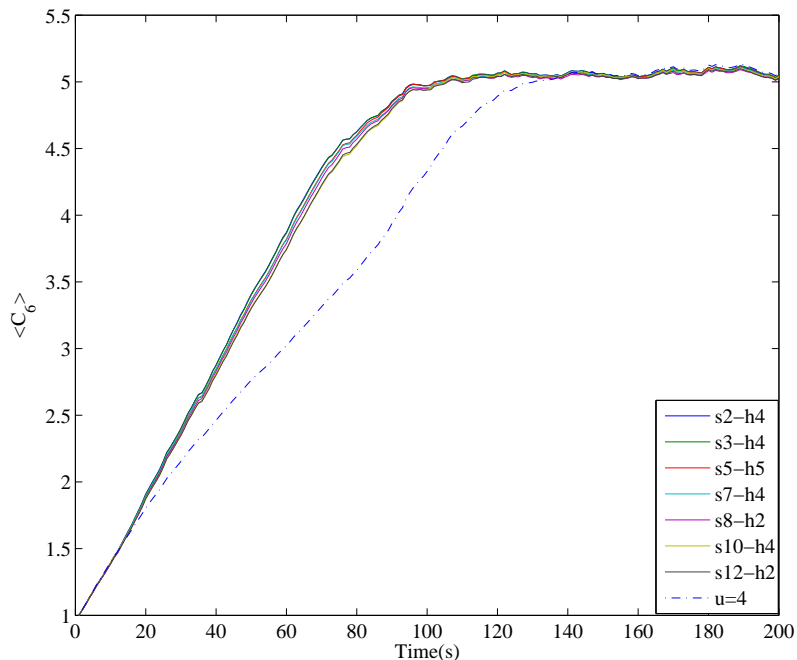


**Figure 31:** Comparison of best controlled  $C_6$  trajectories for each number of control interval  $s$  versus uncontrolled  $C_6$  trajectory with input  $u = 4$ .

is not noticeable, which suggests that the choice of optimal  $s - h$  combination should depend on the computational time it takes to finish the optimization, considering the similarity in their performance.

For a clearer evaluation of the performance of each  $s - h$  combination, a 100-realization-averaged cost for each of these combinations is calculated and the results are shown in Figure 32.

According to Figure 32, we can conclude in general that within each  $s$ , as the control interval length  $h$  gets larger, the 100-realization-averaged cost gets higher and higher, which means the control policy gets worse. This phenomenon matches the theoretical expectation that the less frequently the control policy updates with the latest feedback, the less accurate the control output is. However, for very small  $h$ , the cost increases, suggesting that the control horizon is too short.

Between each step, as  $s$  increases, the average cost increases for a same control

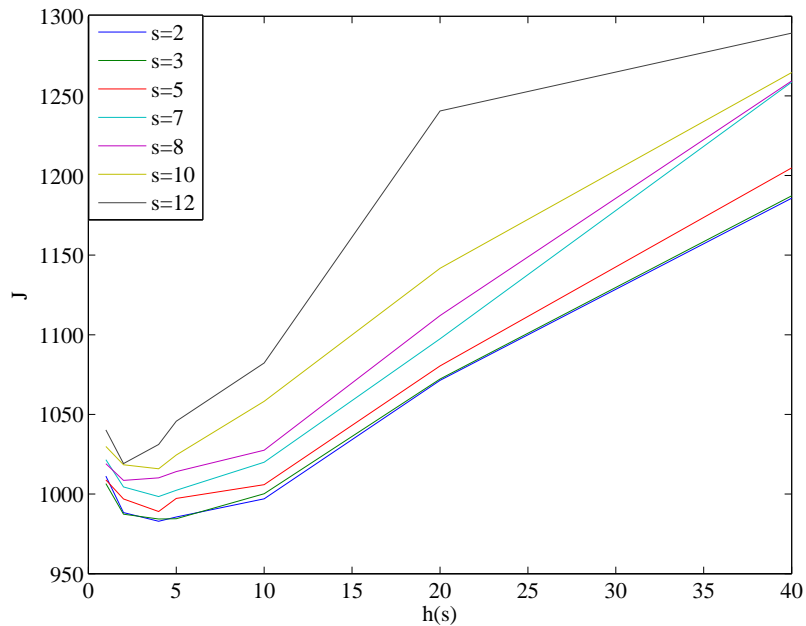


**Figure 32:** Average cost  $J(x, u)$  over 100 realizations for different combination of  $s - h$ .

interval  $h$ . This observation is probably due to the fact that the *simulatedannealing* MATLAB solver does not converge well for large values of  $s$  in our nonlinear, stochastic Langevin model. However, as can be seen in Figure 31, all values of  $s$  give similar performance, relative to the uncontrolled case.

Further, the analysis of several typical optimized control policies demonstrates that the use of a low input value  $u$  at the beginning and a high value of  $u$  towards the end of the simulation process gives a more efficient assembly process. Figure 33 illustrates the average input  $u$  trajectories over 100 realizations for several combinations  $s3 - h4$ ,  $s5 - h5$ , and  $s8 - h2$ .

According to Figure 33, these three typical input trajectories indicate a similar trend: at the beginning of the process, the controller applies a high input  $u$  value, but a sudden drop in the input is observed immediately afterward. This strategy makes sense if we look at the uncontrolled input trajectories shown in Figure 30, which indicates that a very low or very high input value  $u$  would lead to a faster increase

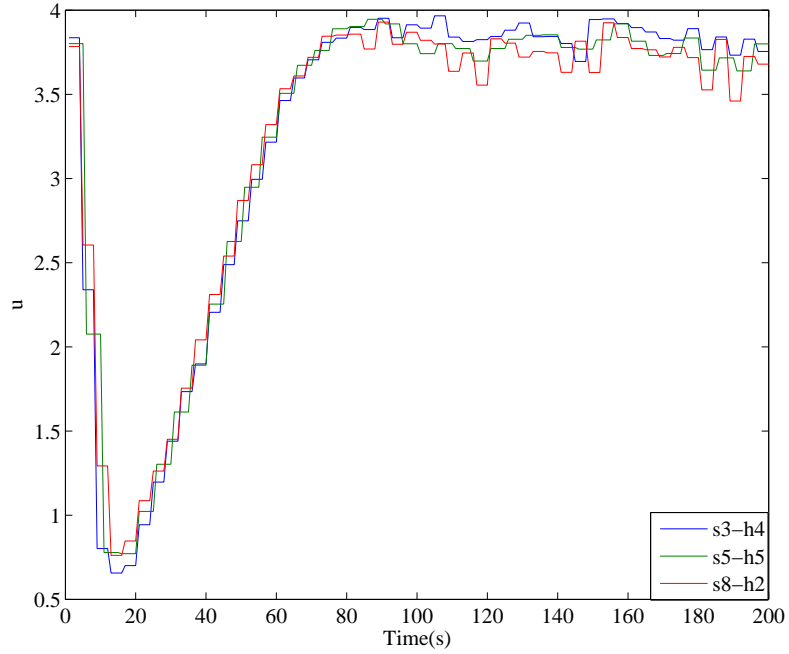


**Figure 33:** Controlled input  $u$  trajectories for combinations of  $s3-h4$ ,  $s5-h5$ ,  $s8-h2$  over 100 realizations.

in the  $C_6$  value, therefore accelerating the crystallization process. After the sudden drop, the control policy applies higher input values and eventually utilizes high values of the input throughout the remaining process. This utilization of high input values is also consistent with the observation in Figure 30 that a higher input value would result in a higher  $C_6$  value in the end.

Besides the effectiveness of the control policy, a low time cost required to perform the optimization is desired for practical application. In order to investigate the change in time needed for different  $s-h$  combinations, we recorded the computational time for 10 realizations, using  $s$  values of 2, 3 and 5 with the same  $h$  as mentioned before. The reason for investigating the time cost for a smaller number of realizations is because all the 100-realization simulations are carried out on a cluster where the time recorded to finish each job is dependent on the CPU used in the cluster, a confounding factor that prevents direct comparisons between jobs. The results are shown in Figure

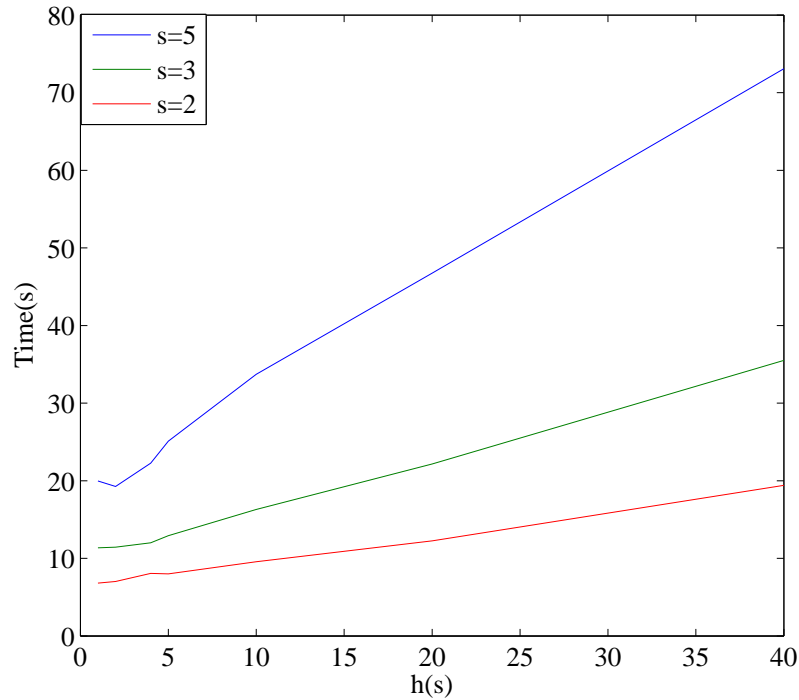


**Figure 34:** Computational time for controlled system with control steps of  $s = 2$ ,  $s = 3$ ,  $s = 5$  and 10 realizations.

34 for these 10-realization studies using a 3.40 GHz Intel(R) Xeon(R) CPU with 16.0 GB memory.

Figure 34 shows the average time needed for a single optimization for each  $s - h$  combination. According to Figure 34, a clear trend can be identified: as the step  $s$  increases, the time needed to finish each optimization increases. The same trend is also observed that when keeping each step  $s$  constant, the time increases as  $h$  increases. The above observation makes sense because an increase in either  $s$  or  $h$  would result in a heavier computation load by increasing the control horizon, therefore elongating the computational time. These observations, together with Figure 31, would aid in the choice of optimization policy for practical uses, considering both the optimality and the computational time. Overall, these results show that only a short control horizon is needed, and this also minimizes computation.

Despite the fact that our control policy is able to give a better result over the

uncontrolled system for our colloidal self-assembly system in respect of the speed of assembly, the computation time needed to finish a single optimization is longer than the updating time  $h$  for all these above tested steps at the moment. In order to make our control policy practical, reduction of the optimization time is required. Further work on identifying a more effective optimization algorithm is the subject of ongoing work.

### ***A.5 Conclusion***

According to the results, the MPC control policy is capable of accelerating the crystallization process while maintaining the desired state. From all the comparisons between the controlled and uncontrolled  $C_6$  trajectories, conclusion can be made that the controlled system gives better outputs than the uncontrolled system. In addition, the time needed to perform an optimization process increases as the control step and control interval increase. Considering the computational time consumption of the controlled system, future work is needed to shorten the optimization time for practical applications.

## REFERENCES

- [1] ADLEMAN, L., CHENG, Q., GOEL, A., HUANG, M., KE, D., ESPANES, P., and ROTHEMUND, P., “Combinatorial optimization problems in self-assembly,” *In Proc. ACM Symposium on Theory of Computing*, 2002.
- [2] ADRIANI, P. M. and GAST, A. P., “A microscopic model of electrorheology,” *Phys. Fluids*, vol. 31, pp. 2757–2768, 1988.
- [3] AKINORI, B. and KOMATSUZAK, T., “Construction of effective free energy landscape from single-molecule time series,” *PNAS*, vol. 104, pp. 19297–19302, 2007.
- [4] ALSAYED, A. M., ISLAM, M. F., ZHANG, J., COLLINGS, P. J., and YODH, A. G., “Premelting at defects within bulk colloidal crystals,” *Science*, vol. 309, pp. 1207–1210, 2005.
- [5] ANDERSON, V. J. and LEKKERKERKER, H. N. W., “Insights into phase transition kinetics from colloid science,” *Nature*, vol. 416, pp. 811–815, 2002.
- [6] ANEKAL, S. and BEVAN, M. A., “Self diffusion in sub-monolayer colloidal fluids near a wall,” *J. Chem. Phys.*, vol. 125, p. 034906, 2006.
- [7] ARIGA, K., HILL, J. P., LEE, M. V., VINU, A., CHARVET, R., and ACHARYA, S., “Challenges and breakthroughs in recent research on self-assembly,” *Sci. Technol. Adv. Mater.*, vol. 9, p. 014109, 2008.
- [8] ARPIN, K. A., AGUSTIN, M., JOHNSON, H. T., BACA, A. J., ROGERS, J. A., LEWIS, J. A., and BRAUN, P. V., “Multidimensional architectures for functional optical devices,” *Adv. Mater.*, vol. 22, pp. 1084–1101, 2010.
- [9] BELTRAN-VILLEGAS, D. J., SEHGAL, R. M., MAEOUDAS, D., FORD, D. M., and BEVAN, M. A., “Fokker-Planck analysis of separation dependent potentials and diffusion coefficients in simulated microscopy experiments,” *Chem. Phys.*, vol. 132, p. 044707, 2010.
- [10] BELTRAN-VILLEGAS, D. J., SEHGAL, R. M., MAROUDAS, D., FORD, D. M., and BEVAN, M. A., “A smoluchowski model of crystallization dynamics of small colloidal clusters,” *J. of Chme. Phys.*, vol. 135, p. 154506, 2011.
- [11] BEMPORAD, A. and MORARI, M., *Robust model predictive control: A survey*. Lecture Notes in Control and Information Sciences, Springer London, 1999.
- [12] BERTSEKAS, D. P., *Dynamic programming and optimal control*. Nashua: Athena Scientific, 2012.

- [13] BEVAN, M. A., FORD, D. M., GROVER, M. A., SHAPIRO, B., MAROUDAS, D., YANG, Y., THYAGARAJAN, R., TANG, X., and SEHGAL, R. M., “Controlling assembly of colloidal particles into structured objects: Basic strategy and a case study,” *J. of Process Control*, vol. 27, pp. 64–75, 2015.
- [14] BHATT, K. H. and VELEV, O. D., “Control and modeling of the dielectrophoretic assembly of on-chip nanoparticle wires,” *Langmuir*, vol. 20, pp. 467–476, 2004.
- [15] BISWAS, A., BAYER, I. S., BIRIS, A. S., WANG, T., DERVISHI, E., and FAUPEL, F., “Advances in top-down and bottom-up surface nanofabrication: Techniques, applications & future prospects,” *Adv. in Colloid and Interface Science*, vol. 170, pp. 2–27, 2012.
- [16] BJÖRNBERG, J. and DIEHL, M., “Approximate robust dynamic programming and robustly stable mpc,” *Automatica*, vol. 42, pp. 777–782, 2006.
- [17] BOCICOR, M.-L., CZIBULA, G., and CZIBULA, I.-G., “A reinforcement learning approach for solving the fragment assembly problem,” pp. 191–198, 2011.
- [18] BOWMAN, G. R., BEAUCHAMP, K. A., BOXER, G., and PANDE, V. S., “Progress and challenges in the automated construction of markov state models for full protein systems,” *J. Chem. Phys.*, vol. 131, p. 124101, 2009.
- [19] BOWMAN, G. R., PANDE, V. S., and FRANK, N., eds., *An introduction to Markov state models and their application to long timescale molecular simulation*. New York: Springer, 1 ed., 2014.
- [20] BRIGGS, A. and SCULPHER, M., “An introduction to markov modelling for economic evaluation,” *PharmacoEconomics*, vol. 13, pp. 397–409, 1998.
- [21] BRONGERSMA, M. L., CUI, Y., and FAN, S., “Light management for photovoltaics using high-index nanostructures,” *Nature Materials*, vol. 13, pp. 451–460, 2014.
- [22] CATCHPOLE, K. R. and POLMAN, A., “Plasmonic solar cells,” *Optics Express*, vol. 16, pp. 21793–21800, 2008.
- [23] CHADES, I., CHAPRON, G., CROS, M. J., GARCIA, F., and SABBADIN, R., “Mdptoolbox: a multi-platform toolbox to solve stochastic dynamic programming problems,” *Ecography*, vol. 37, pp. 916–920, 2014.
- [24] CHEN, J. C. and KIM, A. S., “Brownian dynamics, molecular dynamics, and monte carlo modeling of colloidal systems,” *Advan. in Colloid and Interface Science*, vol. 112, pp. 159–173, 2004.
- [25] CHEN, Q., BAE, S. C., and GRANICK, S., “Directed self-assembly of a colloidal kagome lattice,” *Nature Lett.*, vol. 469, pp. 381–384, 2011.

- [26] CHODERA, J. D., SINGHAL, N., PANDE, V. S., DILL, K. A., and SWOPE, W. C., “Automatic discovery of metastable states for the construction of markov models of macromolecular conformational dynamics,” *J. Chem. Phys.*, vol. 126, p. 155101, 2007.
- [27] CHRISTOFIDES, P. D., EL-FARRA, N., LI, M., and MHASKAR, P., “Model-based control of particulate processes,” *Chemical Engineering Science*, vol. 63, pp. 1156–1172, 2008.
- [28] COIFMAN, R. R., KEVREKIDIS, I. G., MAGGIONI, M., and NADLER, B., “Diffusion maps, reduction coordinates, and low dimensional representation of stochastic systems,” *Multiscale Model. Simul.*, vol. 7, pp. 842–864, 2008.
- [29] COIFMAN, R. R. and LAFON, S., “Diffusion maps,” *Applied and Computational Harmonic Analysis*, vol. 21, pp. 5–30, 2006.
- [30] COLVIN, V. L., “From opals to optics: colloidal photonic crystals,” *MRS Bulletin*, vol. 26, pp. 637–641, 2011.
- [31] CRUZ, C., CHINESTA, F., and RÉGNIER, G., “Review on the brownian dynamics simulation of bead-rod-spring models encountered in computational rheology,” *Arch. Comput. Methods Eng.*, vol. 19, pp. 227–259, 2012.
- [32] DINSMORE, Y. D., WEEKS, E. R., PRASAD, V., LEVITT, A. C., and WEITZ, D. A., “Three-dimensional confocal microscopy of colloids,” *Applied Optics*, vol. 40, pp. 4152–4159, 2001.
- [33] DUGUET, E., HUBERT, C., CHOMETTE, C., PERRO, A., and RAVAINÉ, S., “Patchy colloidal particles for programmed self-assembly,” *Comptes Rendus Chimie*, vol. 19, pp. 173–182, 2016.
- [34] EDWARDS, T. D., BELTRAN-VILLEGAS, D. J., and BEVAN, M. A., “Size dependent thermodynamics and kinetics in electric field mediated colloidal crystal assembly,” *Soft Matter*, vol. 9, pp. 9208–9218, 2013.
- [35] EDWARDS, T. D., YANG, Y., BELTRAN-VILLEGAS, D. J., and BEVAN, M. A., “Colloidal crystal grain boundary formation and motion,” *Scientific Reports*, vol. 4, p. 6132, 2014.
- [36] ENGHETA, N., “150 years of maxwell’s equations,” *Science*, vol. 349, pp. 136–137, 2015.
- [37] FODOR, I. K., “A survey of dimension reduction techniques,” 2002.
- [38] GARCÍA, P. D., SAPIENZA, R., BLANCO, A., and LÓPEZ, C., “Photonic glass: a novel random material for light,” *Adv. Mater.*, vol. 19, pp. 2597–2602, 2007.

- [39] GATES, B. D., XU, Q., STEWART, M., RYAN, D., WILLSON, C. G., and WHITESIDES, G. M., “New approaches to nanofabrication: molding, printing, and other techniques,” *Chem. Rev.*, vol. 105, pp. 1171–1196, 2005.
- [40] GOLDMAN, A. J., COX, R. G., and BRENNER, H., “Slow viscous motion of a sphere parallel to a plane wall – i. motion through a quiescent fluid,” *Chem. Eng. Sci.*, vol. 22, pp. 637–651, 1967.
- [41] GOYAL, A., HALL, C. K., and VELEV, O. D., “Self-assembly in binary mixtures of dipolar colloids: Molecular dynamics simulations,” *J. Chem. Phys.*, vol. 133, p. 064511, 2010.
- [42] GRIFFIN, D. J., GROVER, M. A., KAWAJIRI, Y., and ROUSSEAU, R. W., “Data-driven modeling and dynamic programming applied to batch cooling crystallization,” *Ind. Eng. Chem. Res.*, vol. 55, pp. 1361–1372, 2016.
- [43] GRIFFIN, D. J., TANG, X., and GROVER, M. A., “Externally-directing self-assembly with dynamic programming,” *American Control Conference*, pp. 3086–3091, 2016.
- [44] GRZELCZAK, M., VERMANT, J., FURST, E. M., and LIZ-MARZÁN, L. M., “Directed self-assembly of nanoparticles,” *ACS Nano*, vol. 4, pp. 3591–3605, 2010.
- [45] GRZYBOWSKI, B. A., WILMER, C. E., KIM, J., BROWNE, K. P., and BISHOP, K. J. M., “Self-assembly: from crystals to cells,” *Soft Matter*, vol. 5, pp. 1110–1128, 2009.
- [46] GULDEN, J., YEFANOV, O. M., MANCUSO, A. P., ABRAMOVA, V. V., HILHORST, J., BYELOV, D., SNIGIREVA, I., SNIGIREV, A., PETUKHOV, A. V., and VARTANYANTS, I. A., “Coherent x-ray imaging of defects in colloidal crystals,” *Phys. Rev. B*, vol. 81, p. 224105, 2010.
- [47] HONG, L., CACCIUTO, A., LUIJTEN, E., and GRANICK, S., “Clusters of amphiphilic colloidal spheres,” *Langmuir*, vol. 24, pp. 621–625, 2008.
- [48] HUANG, X., YAO, Y., BOWMAN, G. R., SUN, J., GUIBAS, L. J., CARLSON, G., and PANDE, V., “Constructing multi-resolution markov state models (msms) to elucidate rna hairpin folding mechanisms,” *Pac. Symp. Biocomput.*, vol. 134, pp. 228–239, 2010.
- [49] HUMMER, G., “Position-dependent diffusion coefficients and free energies from bayesian analysis of equilibrium and replica molecular dynamics simulations,” *New Journal of Physics*, vol. 7, 2005.
- [50] JAIN, A. K., MURTY, M. N., and FLYNN, P. J., “Data clustering: a review,” *ACM Computing Survey*, vol. 31, pp. 264–323, 1999.

- [51] JENSEN, K. E., PENNACHIO, D., RECHT, D., WEITZ, D. A., and SPAEPEN, F., “Rapid growth of large, defect-free colloidal crystals,” *Soft Matter*, vol. 9, pp. 320–328, 2013.
- [52] JIANG, M., ZHU, X., MOLARO, M. C., RASCHE, M. L., ZHANG, H., CHADWICK, K., RAIMONDO, D. M., KIM, K.-K. K., ZHOU, L., ZHU, Z., WONG, M. H., O’GRADY, D., HEBRAULT, D., TEDESCO, J., and BRAATZ, R. D., “Modification of crystal shape through deep temperature cycling,” *Ind. Eng. Chem. Res.*, vol. 53, pp. 5325–5336, 2014.
- [53] JUÁREZ, J. J. and BEVAN, M. A., “Interactions and microstructures in electric field mediated colloidal assembly,” *J Chem Phys*, vol. 131, p. 134704, 2009.
- [54] JUÁREZ, J. J. and BEVAN, M. A., “Feedback controlled colloidal self-assembly,” *Advanced Functional Materials*, vol. 22, pp. 3833–3839, 2012.
- [55] JUÁREZ, J. J., LIU, B. G., CUI, J.-Q., and BEVAN, M. A., “kt-scale colloidal interactions in high-frequency inhomogeneous ac electric fields. ii. concentrated ensembles,” *Langmuir*, vol. 27, pp. 9219–9226, 2011.
- [56] KALIDINDI, S. R., NIEZGODA, S. R., and SALEM, A. A., “Microstructure informatics using higher-order statistics and efficient data-mining protocols,” *JOM*, pp. 34–41, 2011.
- [57] KARG, M., KÖNIG, T. A. F., RETSCH, M., STELLING, C., REICHSTEIN, P. M., HONOLD, T., THELAKKAT, M., and FERY, A., “Colloidal self-assembly concepts for light management in photovoltaics,” *Materials Today*, vol. 18, pp. 185–205, 2015.
- [58] KELLER, B., DAURA, X., and VAN GUNSTEREN, W. F., “Comparing geometric and kinetic cluster algorithms for molecular simulation data,” *J. Chem. Phys.*, vol. 132, p. 074110, 2010.
- [59] KIM, S.-H., LEE, S. Y., YANG, S.-M., and YI, G.-R., “Self-assembled colloidal structures for photonics,” *NPG Asia Materials*, vol. 3, pp. 25–33, 2011.
- [60] KLOTSA, D. and JACK, R. L., “Controlling crystal self-assembly using a real-time feedback scheme,” *J Chem Phys*, vol. 138, p. 094502, 2013.
- [61] KOPELEVICH, D. I., PANAGIOTOPOULOS, A. Z., and KEVREKIDIS, I. G., “Coarse-grained kinetic computations for rare events: Application to micelle formation,” *J. of Chem.Phys.*, vol. 122, p. 044908, 2005.
- [62] LEMONS, D. S. and GYTHIEL, A., “Paul langevin’s 1908 paper “on the theory of brownian motion”,” *Amer. J. Phys.*, vol. 65, pp. 1079–1081, 1997.
- [63] LI, P., TREASURE, R. J., and KRUGER, U., *Dynamic Principal Component Analysis using subspace model identification*. Berlin: Springer Berlin Herdelberg, 2005.

- [64] LU, P. J. and WEITZ, D. A., “Colloidal particles: crystals, glasses, and gels,” *Annu. Rev. Condens. Matter. Phys.*, vol. 4, pp. 217–233, 2013.
- [65] MALMSTROM, R. D., LEE, C. T., WART, A. T. V., and AMARO, R. E., “Application of molecular-dynamics based markov state models to functional proteins,” *J. Chem. Theory Comput.*, vol. 10, pp. 2648–2657, 2014.
- [66] MAYER, M., TEBBE, M., KUTTNER, C., SCHNEPF, M. J., KÖNIG, T. A. F., and FERY, A., “Template-assisted colloidal self-assembly of macroscopic magnetic metasurfaces,” *Faraday Discussions*, 2016.
- [67] MENDES, M. J., MORAWIEC, S., SIMONE, F., PRIOLO, F., and CRUPI, I., “Colloidal plasmonic back reflectors for light trapping in solar cells,” *Nanoscale*, vol. 6, pp. 4796–4805, 2014.
- [68] MOHRAZ, A. and SOLOMON, M. J., “Direct visualization of colloidal rod assembly by confocal microscopy,” *Langmuir*, vol. 21, pp. 5298–5306, 2005.
- [69] NAGAMANASA, K. H., GOKHALE, S., GANAPATHY, R., and SOOD, A. K., “Confined glassy dynamics at grain boundaries in colloidal crystals,” *Proc. Natl. Acad. Sci. U. S. A.*, vol. 108, pp. 11323–11326, 2011.
- [70] NEDIALKOVA, L. V., AMAT, M. A., KEVREKIDIS, I. G., and HUMMER, G., “Diffusion maps, clustering and fuzzy markov modeling in peptide folding transitions,” *J. Chem. Phys.*, vol. 141, p. 114102, 2014.
- [71] NYKYPANCHUK, D., MAYE, M. M., VAN DER LELIE, D., and GANG, O., “Dna-guided crystallization of colloidal nanoparticles,” *Nature Lett.*, vol. 451, pp. 549–552, 2008.
- [72] OUELLETTE, J., “Seeing the future in photonic crystals,” *The Industrial Physicist*, pp. 14–17, 2002.
- [73] OZBAY, E., “The magical world of photonic metamaterials,” *Opt. Photonics News*, vol. 19, pp. 22–27, 2008.
- [74] PANDE, V. S., BEAUCHAMP, K., and BOWMAN, G. R., “Everything you wanted to know about markov state models but were afraid to ask,” *Methods*, vol. 52, pp. 99–105, 2010.
- [75] PAULSON, J. A., MESBAH, A., ZHU, X., MOLARO, M. C., and BRAATZ, R. D., “Control of self-assembly in micro- and nano-scale systems,” *Journal of Process Control*, vol. 27, pp. 38–49, 2015.
- [76] PERKETT, M. R. and HAGAN, M. F., “Using markov state models to study self-assembly,” *J. Chem. Phys.*, vol. 140, p. 214101, 2014.
- [77] POWELL, W. B., *Approximate dynamic programming solving the curses of dimensionality*. New Jersey: Wiley, 2011.

- [78] PRINZ, J.-H., WU, H., SARICH, M., KELLER, B., SENNE, M., HELD, M., CHODERA, J. D., SCHÜTTE, C., and NOÉ, F., “Markov models of molecular kinetics: Generation and validation,” *J. Chem. Phys.*, vol. 134, p. 174105, 2011.
- [79] PUTERMAN, M. L., *Markov decision processes: discrete stochastic dynamic programming*. New Jersey: Wiley-Interscience, 2005.
- [80] QIN, S. J. and BADGWELL, T. A., “A survey of industrial model predictive control technology,” *Control Engineering Practice*, vol. 11, pp. 733–764, 2003.
- [81] RAWLING, J. B. and MAYNE, D. Q. Madison: Nob Hill Publishing, 2009.
- [82] RISKEN, H. New York: Springer, 1996.
- [83] RIVOTTI, P. and PISTIKOPOULOS, E. N., “A dynamic programming based approach for explicit model predictive control of hybrid systems,” *Computer & Chemical Engineering*, vol. 72, pp. 126–144, 2015.
- [84] ROCCHI, L., CHIARI, L., and CAPPELLO, A., “Feature selection of stabilometric parameters based on principal component analysis,” *Medical and Biological Engineering and Computing*, vol. 42, pp. 71–79, 2004.
- [85] ROGERS, W. B., SHIH, W. M., and MANOHARAN, V. N., “Using dna to program the self-assembly of colloidal nanoparticles and microparticles,” *Nature Reviews*, vol. 1, pp. 1–13, 2016.
- [86] ROHRDANZ, M. A., ZHENG, W., MAGGIONI, M., and CLEMENTI, C., “Determination of reaction coordinates via locally scaled diffusion map,” *J. Chem. Phys.*, vol. 134, p. 124116, 2011.
- [87] ROSS, F. M., “Opportunities and challenges in liquid cell electron microscopy,” *Science*, vol. 350, 2015.
- [88] RYCENGA, M., CAMARGO, P. H. C., and XIA, Y., “Template-assisted self-assembly: a versatile approach to complex micro- and nanostructures,” *Soft Matter*, vol. 5, pp. 1129–1130, 2009.
- [89] SANTISO, E. E. and TROUT, B. L., “A general set of order parameters for molecular crystals,” *J. Chem. Phys.*, vol. 134, p. 064109, 2011.
- [90] SCHALL, P., COHEN, I., WEITZ, D. A., and SPAEPEN, F., “Visualization of dislocation dynamics in colloidal crystals,” *Science*, vol. 305, pp. 1944–1948, 2004.
- [91] SCHÜTTE, C., NOÉ, F., LU, J., SARICH, M., and VANDEN-EIJNDEN, E., “Markov state models based on milestoning,” *J. Chem. Phys.*, vol. 134, p. 204105, 2011.

- [92] SHERMAN, Z. M. and SWAN, J. W., “Dynamic, directed self-assembly of nanoparticles via toggled interactions,” *ACS Nano*, vol. 10, no. 5, pp. 5260–5271, 2016.
- [93] SHUKLA, D., HERNÁNDEZ, C. X., WEBER, J. K., and PANDE, V. S., “Markov state models provide insights into dynamic modulation of protein function,” *Acc. Chem. Res.*, vol. 48, pp. 414–422, 2015.
- [94] SINGHAL, N. and PANDE, V. S., “Error analysis and efficient sampling in markovian state models for molecular dynamics,” *J. Chem. Phys.*, vol. 123, p. 204909, 2005.
- [95] SKINEER, T. O. E., AARTS, D. G. A. L., and DULLENS, R. P. A., “Grain-boundary fluctuations in two-dimensional colloidal crystals,” *Phys. Rev. Lett.*, vol. 105, p. 168301, 2010.
- [96] SOLIS, E. O. P., BARTON, P. I., and STEPHANOPOULOS, G., “Controlled formation of nanostructures with desired geometries. 1. robust static structures,” *Industrial & Engineering Chemistry Research*, vol. 49, pp. 7728–745, 2010.
- [97] SOLIS, E. O. P., BARTON, P. I., and STEPHANOPOULOS, G., “Controlled formation of nanostructures with desired geometries. 2. robust static structures,” *Industrial & Engineering Chemistry Research*, vol. 49, pp. 7746–757, 2010.
- [98] SRIRAMAN, I. G. K. S. and HUMMER, G., “Coarse master equation from bayesian analysis of replica molecular dynamics,” *J. Chem. Phys.*, vol. 109, pp. 6479–6484, 2005.
- [99] STEBE, K. J., LEWANDOWSKI, E., and GHOSH, M., “Oriented assembly of metamaterials,” *Science*, vol. 325, p. 5937, 2009.
- [100] SUTTER, E., SUTTER, P., TKACHENKO, A. V., KRAHNE, R., DE GRAAF, J., ARCINIEGAS, M., and MANNA, L., “in situ microscopy of the self-assembly of branched nanocrystals in solution,” *Nature Comm.*, vol. 7, p. 11213, 2016.
- [101] SWAN, J. W., BAUER, J. L., LIU, Y., and FURST, E. M., “Directed colloidal self-assembly in toggled magnetic fields,” *Soft Matter*, vol. 10, pp. 1102–1109, 2014.
- [102] SWAN, J. W. and BRADY, J. F., “Simulation of hydrodynamically interacting particles near a no-slip boundary,” *Phys. Fluid*, vol. 19, p. 113306, 2007.
- [103] TAN, P., STEINBACH, M., and KUMAR, V. Boston: Addison-Wesley Longman, 2005.
- [104] TANG, X., RUPP, B., YANG, Y., EDWARD, T. D., GROVER, M. A., and BEVAN, M. A., “Optimal feedback controlled assembly of perfect crystals,” *ACS Nano*, vol. 10, pp. 6791–6798, 2016.

- [105] TANG, X., XUE, Y., and GROVER, M. A., “Colloidal self-assembly with model predictive control,” *Proc. of American Control Conf.*, 2012.
- [106] THEODORAKIS, P. E., FYTAS, N. G., KAHL, G., and DELLAGO, C., “Self-assembly of dna-functionalized colloids,” *Cond. Matter Phys.*, vol. 18, pp. 1–24, 2015.
- [107] TIERNO, P., “Magnetic assembly and annealing of colloidal lattices and superlattices,” *Langmuir*, vol. 30, pp. 7670–5, 2014.
- [108] TRAN, S. B. Q., MARMOTTANT, P., and THIBAUT, P., “Fast acoustic tweezers for the two-dimensional manipulation of individual particles in microfluidic channels,” *Appl. Phys. Lett.*, vol. 101, p. 114103, 2012.
- [109] VAN DER MAATEN, L. J. P., POSTMA, E. O., and VAN DEN HERIK, H. J., “Dimensionality reduction: a comparative review,” 2008.
- [110] VICTOR, B. L., LOUSA, D., ANTUNES, J. M., and SOARES, C. M., “Self-assembly molecular dynamics simulations shed light into the interaction of the influenza fusion peptide with a membrane bilayer,” *J. Chem. Inf. Model.*, vol. 55, pp. 795–805, 2015.
- [111] VUTUKURI, H. R., SMALLENBURG, F., BADAIRE, S., IMHOF, A., DIJKSTRA, M., and v. BLAADEREN, A., “An experimental and simulation study on the self-assembly of colloidal cubes in external electric fields,” *Soft Matter*, vol. 10, pp. 9110–9119, 2014.
- [112] WALIA, S., SHAH, C. M., GUTRUF, P., NILI, H., CHOWHURY, D. R., WITHAYACHUMNANKUL, W., BHASKARAN, M., and SRIRAM, S., “Flexible metasurfaces and metamaterials: A review of materials and fabrication processes at micro- and nano-scales,” *Appl. Phys. Rev.*, vol. 2, p. 011303, 2015.
- [113] WANG, Y., WANG, Y., ZHENG, X., DUCROT, E., YODH, J. S., WECK, M., and PINE, D. J., “Crystallization of dna-coated colloids,” *Nature Comm.*, vol. 6, p. 7253, 2015.
- [114] XIA, Y., YIN, Y., LU, Y., and MCLELLAN, J., “Template-assisted self-assembly of spherical colloids into complex and controllable structures,” *Adv. Func. Mater.*, vol. 13, pp. 907–918, 2003.
- [115] XUE, Y., BELTRAN-VILLEGAS, D. J., TANG, X., BEVAN, M. A., and GROVER, M. A., “Optimal design of a colloidal self-assembly process,” *IEEE Transactions on Control Systems Technology*, vol. 22, pp. 1956–1963, 2014.
- [116] XUE, Y., LUDOVICE, P. J., GROVER, M. A., NEDIAKOVA, L. V., DSILVA, C. J., and KEVREKIDIS, I. G., “State reduction in molecular simulations,” *Computers Chemical Engineering*, vol. 51, pp. 102–110, 2012.

- [117] YANG, S., ONUCHIC, J. N., and LEVINE, H., “Effective stochastic dynamics on a protein folding energy landscape,” *J. Chem. Phys.*, vol. 125, p. 054910, 2006.
- [118] YANG, Y., THYAGARAJAN, R., FORD, D. M., and BEVAN, M. A., “Dynamic colloidal assembly pathways via low dimensional models,” *J. of Chem.Phys.*, vol. 144, p. 204904, 2016.
- [119] YAO, F., COQUERY, J., and CAO, K.-A. L., “Independent principal component analysis for biologically meaningful dimension reduction of large biological data sets,” *BMC Bioinformatics*, vol. 13, p. 1, 2012.
- [120] YUSTE, S. B. and SANTOS, A., “A heuristic radial-distribution function for hard disks,” *J. Chem. Phys.*, vol. 99, pp. 2020–2023, 1993.
- [121] ZHANG, H., SROLOVITZ, D. J., DOUGLAS, J. F., and WARREN, J. A., “Characterization of atomic motion governing grain boundary migration,” *Phys. Rev. B: Condens. Matter Mater. Phys.*, vol. 74, p. 115404, 2006.
- [122] ZHANG, H., SROLOVITZ, D. J., DOUGLAS, J. F., and WARREN, J. A., “Grain boundaries exhibit the dynamics of glass-forming liquids,” *Proc. Natl. Acad. Sci. U. S. A.*, vol. 106, pp. 7735–7740, 2009.
- [123] ZHANG, J., LI, Y., ZHANG, X., and YANG, B., “Colloidal self-assembly meets nanofabrication: From two-dimensional colloidal crystals to nanostructure arrays,” *Adv. Mater.*, vol. 4, pp. 4249–4269, 2010.
- [124] ZHAO, Y., XIE, Z., GU, H., ZHU, C., and GU, Z., “Bio-inspired variable structural color materials,” *Chem. Soc. Rev.*, vol. 41, pp. 3297–3317, 2012.
- [125] ZHENG, H., CLARIDGE, S. A., MINOR, A. M., ALIVISATOS, A. P., and DAHMEN, U., “Nanocrystal diffusion in a liquid thin film observed by in situ transmission electron microscopy,” *Nano Lett.*, vol. 9, pp. 2460–2465, 2009.
- [126] ZHU, B., XU, J., LI, Y., WANG, T., XIONG, K., LEE, C., YANG, X., SHIIBA, M., TAKEUCHI, S., ZHOU, Q., and SHUNG, K. K., “Micro-particle manipulation by single beam acoustic tweezers based on hydrothermal pzt thick film,” *AIP Adv.*, vol. 6, p. 035102, 2016.

# Markov state model-based optimal control for colloidal self-assembly

Xun Tang

121 Pages

Directed by Professor Martha A. Grover

Colloidal self-assembly is widely studied as a promising route to manufacture highly ordered structures for applications as metamaterials. While near-equilibrium self-assembly could produce defect-free crystal, the time required is usually unmanageable in practical applications. On the contrary, rapid assembly via out-of-equilibrium approaches could reduce the amount of process time, but the assembled structure is usually terminated in defective states. Therefore, a gap exists between the speed and the quality of the structure in a colloidal self-assembly system. To overcome this challenge, this thesis proposes a model-based optimization framework for optimal feedback control over a colloidal self-assembly process for rapid assembly of defect-free two-dimensional crystals.

The proposed framework features: first, the use of an externally applied electric field as a global actuator to influence the particle movement; second, the use of two order parameters to represent the high dimensional system in a reduced dimension state space; third, the use of the Markov state model to capture the stochasticity in the system; fourth, the use of dynamic programming to design the optimal control policy; and fifth, the use of an optical microscope for *in situ* measurements as feedback.

The feasibility of the framework is first demonstrated with a static optimal control policy, and its performance is evaluated against fast quench and near-equilibrium approaches. The framework is then expanded to construct a time-dependent optimal control policy, and the performance is compared with widely used time-varying control strategies in both simulation and experiments. The refinement of the framework, more specifically, the construction of the Markov state model is also revisited for

better efficiency.

The major contributions of this thesis include: (1) it proposes a novel approach to rapidly control colloidal self-assembly processes for perfect crystal with optimal control theories; (2) it demonstrates for the first time in lab, the realization of optimal feedback control of a colloidal self-assembly process; (3) it reveals the benefits of feedback in a stochastic process control, not only to compensate for model inaccuracy, but also to shorten the process time; (4) it also investigates the Markov state model accuracy and provides a more efficient construction of accurate Markov state models.

The framework in this study is built on first-principle concepts, and it can be generalized to any molecular, nano-, or micro-scale assembly process where there exists a global actuator to affect the dynamics, a model to represent the relation between the actuator and the system, and a measurement of system state for feedback. Since micron-sized colloidal particles also serve as model systems to study the phase transition behavior and crystallization kinetics for atomic and molecular crystals, the framework can also be extended to these systems for optimal control.